A Sr-isotopic investigation of bifurcating chromitite layers of the UG1 at the Impala Platinum Mine, Rustenburg.

Tshepo Felix Nyakane

For submission in accordance with the requirements for the degree:

Master of Science

In

Geology

Faculty of Natural and Agricultural Sciences

University of the Free State

Bloemfontein

Supervisor: Mrs Justine Magson

Co-supervisor: Prof. Frederick Roelofse

UNIVERSITY OF THE FREE STATE
UNIVERSITEIT VAN DIE VRYSTAAT
YUNIVESITHI YA FREISTATA

UFS
NATURAL AND AGRICULTURAL SCIENCES

Declaration

I, Tshepo Felix Nyakane, declare that the Master's Degree research dissertation that I herewith submit for the Master's Degree qualification in Geology at the University of the Free State is my independent work, and that I have not previously submitted it for a qualification at another institution of higher education.

Tshepo Felix Nyakane

Signed

2023/07/25

Date

Acknowledgements

Firstly, I would like to express my gratitude towards my supervisor Mrs Justine Magson and co-supervisor Professor Frederick Roelofse of the Department of Geology at the University of the Free State for all their invaluable assistance and guidance during my research journey. This study would not have been possible if it were not for them.

I would also like to thank Dr Christian Reinke, of the Analytical Facility at the University of Johannesburg, for his assistance in performing analyses on my thin sections with the Cameca SX – 100 Microprobe. A special thanks to Henriette Ueckermann for her assistance with the use of the Nu Plasma II MC-ICPMS linked with a 193 nm ArF RESOlution SE excimer laser housed at the University of Johannesburg's Spectrum Analytical Facility and for going the extra mile to ensure that I had everything that I needed during my visit to the University of Johannesburg. Thanks to Diana Faseka for ensuring I was comfortable in my accommodation at the Geology guest rooms during my stay.

Great thanks to the kind members of the Department of Geology at the University of the Free State for their great advice and guidance. I would also like to acknowledge the support of Iphakade for providing financial assistance for my study, without which I would not have been able to complete this study.

I would like to express my utmost gratitude to my parents Pulane and Napo Nyakane, for their financial and emotional support throughout my academic journey and for always being there whenever I needed them.

Lastly, thanks to the man who inspired me to pursue this academic journey and why I kept going even when I felt like giving up, my late grandfather, Sello Ezekiel Masenkane.

Abstract

Chromitite bifurcations hosted within, but not limited to, the Upper Group 1 (UG1) chromitite layer in the Critical Zone of the Bushveld Complex are one of the most enigmatic geological features encountered. Several researchers have attempted to develop models explaining how these bifurcations could have been formed. Most of these studies were heavily based on field observation with little to no geochemical data to support their findings. In this study, samples of an exposure of chromitite bifurcations from the UG1 chromitite at Shaft No.11 of Impala Platinum Limited in the Western Limb of the Bushveld Complex were utilised to perform petrographic and geochemical work including Sr-isotopic determinations on plagioclase. The geochemical data collected, along with field observations, were used to develop a conceptual model explaining the development of the bifurcations.

Four sample cuts (D, C, B, and A) across the anorthositic footwall of the UG1 chromitite, each with a width of 10 cm and varying lengths were sampled from the study area using a diamond saw. The sample cuts represent vertical transects across a set of bifurcating chromitite layers, taken approximately 1 m apart, on the northern side of the approximately 40 m section. Thirty-four polished thin sections were made representing all the sample cuts. The polished thin sections were studied petrographically with an Olympus BX51 microscope. Electron microprobe analyses were carried out to obtain the compositions of chromite and plagioclase crystals from the samples, and Laser Ablation Multi-Collector Inductively Coupled Mass Spectrometry was used to obtain in-situ isotopic compositions of the plagioclase crystals.

Plagioclase in the anorthosite layers exhibits very little variation in An% with average values of 75.10 ± 3.27, 74.26 ± 1.93, 75.10 ± 3.27 and 73.85 ± 1.89 for sample cut D to A, respectively. Plagioclase in the chromitite layers reveals much more significant variation in An% with average values of 70.69 ± 14.15, 78.16 ± 15.26, 56.49 ± 33.13 and 55.50 ± 36.68 for sample cuts D to A, respectively. The in-situ plagioclase isotopic composition reveals that the initial $^{87}Sr/^{86}Sr$ ratios of plagioclase in anorthosite show very little variation both vertically and laterally through sample cuts A to D, with an average value of 0.7062 and individual layers that are generally within error compared to adjacent layers. Most chromitite layers also display $^{87}Sr/^{86}Sr$ ratios that are comparable to those observed in the anorthosite, although some of the

thicker layers returned values that are more radiogenic, e.g., the bottom thick layer in sample cut A, which returned values on the order of 0.709 – 0.710.

Taking into account the field relations along with the petrography and geochemistry of the study area, it is envisaged that the chromitite bifurcations in the study area were formed in the following stages:

(1) Development of an irregular floor through the thermo-chemical erosion of the underlying anorthosite footwall.
(2) The intrusion of chromite-rich slurry (mass balance requirement) as a basal flow resulted in thick chromitite layer deposition on an uneven surface.
(3) Development of cyclic anorthosite and chromitite forming bifurcations. Pressure fluctuations (magma influxes, roof rupturing events, shock waves) permitted rapid transitions between the system's chromitite and plagioclase stability fields. A large reservoir of melt likely buffered compositional and isotopic changes.
(4) The intrusion of a chromite-rich slurry led to renewed erosion and formation of the thick upper chromitite layer, with the thin chromitite layers now appearing as offshoots from the base of this layer.
(5) Downward intrusion of slurry into rheologically weak zones led to the development of additional bifurcations.

Contents

List of Figures

List of Tables

1. Introduction

The Bushveld Complex (BC) has been the focal point for many researchers, primarily because of its platinum group element (PGE) mineralisation and for many other enigmatic features observed within the complex over the past years. One of the most enigmatic features of the Bushveld Complex, and the focus of numerous investigations, is the chromitite bifurcations, the splitting and merging of chromitite layers observed in (but not limited to) the Upper Group 1 (UG1) chromitite layer (Nicholson, 2020; Nex, 2004). The focus of this study will be the UG1 chromitite layer at Shaft No.11 of Impala Platinum Limited in the Western Limb of the Bushveld Complex **(Figure 1)**, which exposes intricate chromitite bifurcations separated by anorthosite.

Although numerous studies have been made on the formation of chromitite bifurcations by Lee (1981), Cawthorn (2003, 2015), Nex (2004), Voordouw *et al.* (2009), Mukherjee *et al.* (2017), Pebane & Latypov (2017), Nicholson (2020), and Maghdour-Mashhour & Hayes (2021) there remains a lack of consensus on how these enigmatic structures came to be.

This study aims to contribute to our understanding of how chromitite bifurcations were formed. The objectives of this study were achieved through in-situ analysis of the Sr-isotopic compositions of in situ plagioclase in order to test for the involvement of isotopically distinct magmas in the genesis of bifurcating chromitites of the UG1 at Shaft No.11 of Impala Platinum Limited. The samples for the present investigation originate from the work of Nicholson (2020), who conducted a geochemical and petrological assessment of the bifurcated chromitites. The Sr-isotopic results were complemented by detailed petrographic studies on the chromitites and intervening anorthosites and the determination of mineral chemical variations across the interval in question.

1.1 Geology of the Bushveld Complex

The BC hosts the most extensive known layered intrusion on Earth and was emplaced into the rocks of the Transvaal Supergroup between 2058.9 and 2054.4 Ma (Zeh *et al.,* 2015). The complex contains more than 70% of known global PGEs (Chitiyo *et al.,* 2008; Li *et al.,* 2004) and consists of the mafic-ultramafic rocks of the Rustenburg Layered Suite (RLS) at the base,

and the sheeted granitic rocks of the Rashoop Granophyre Suite and the Lebowa Granite Suite above it **(Figure 1)** (. Nex, 2004; Voordouw *et al.*, 2009; Zeh *et al.*, 2015).

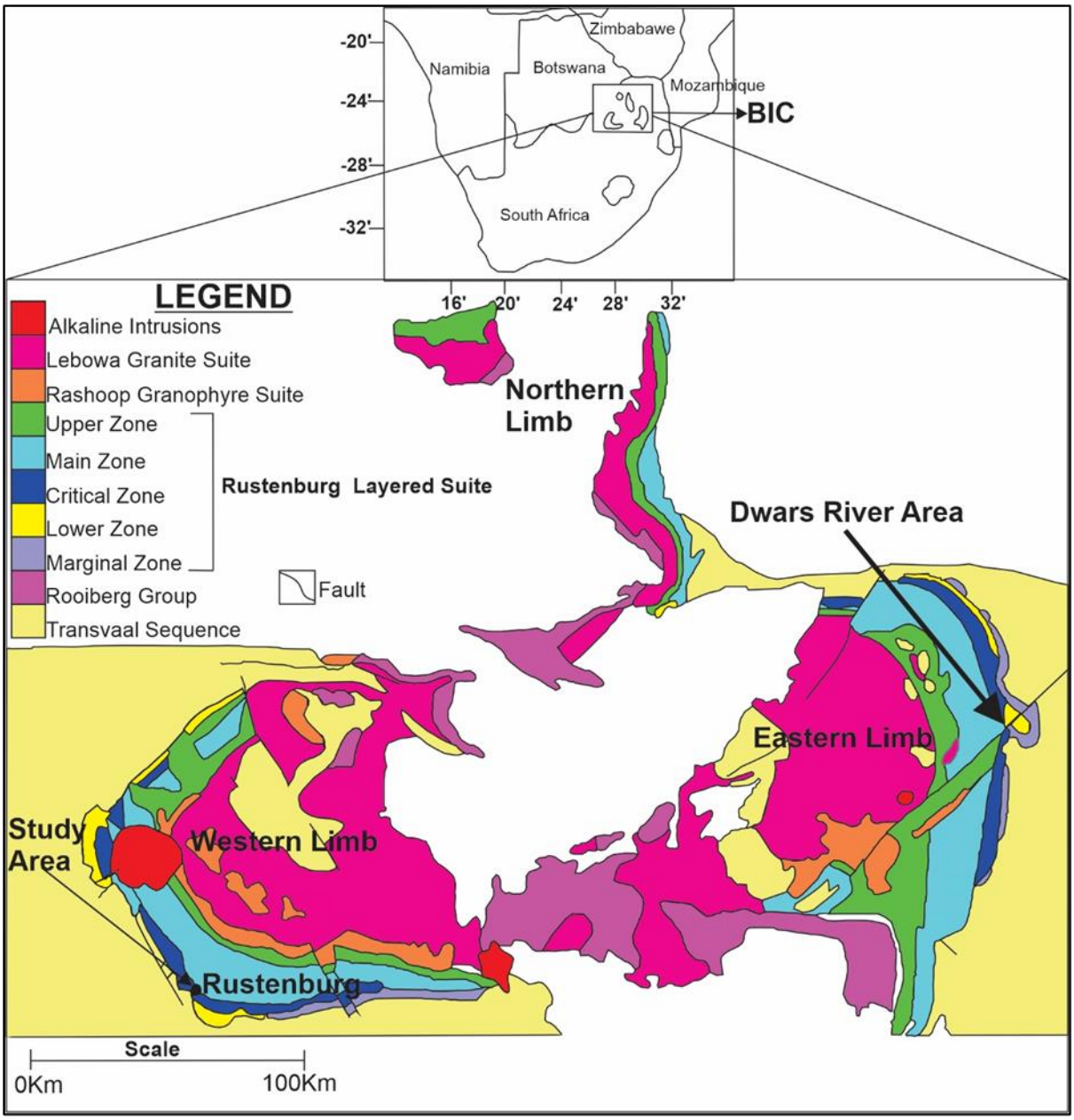

Figure 1: Geographical location of the Bushveld Complex and the location of the study area along with that of the Dwars River Locality (modified from Nicholson, 2020).

The RLS intruded the sedimentary rocks of the Transvaal Supergroup. The intrusion was likely preceded by the eruption of the Rooiberg Volcanic Sequence and succeeded by the emplacement of the Rashoop Granophyre Suite and the Lebowa Granite Suite (Eales & Cawthorn, 1996; Zeh *et al*., 2015). The RLS covers an area of approximately 65 000 km^2 and has a maximum thickness of approximately 7-9 km. It occurs horizontally within five limbs, *viz.* the Northern, Eastern, Western, Far Western, and South-eastern limbs. The South-eastern Limb does not outcrop as it is overlain by younger sediments, but its presence and approximate

extent are known from geophysical data and drill core material. The RLS has been further divided vertically into five zones extending laterally throughout the Bushveld Complex **(Figure 2)**, *viz.* the Marginal (MZ), Lower (LZ), Critical (CZ), Main (MZ), and Upper zones (UZ), based on the petrological, mineralogical, and geochemical variations occurring vertically within the suite (Eales & Cawthorn, 1996; Voordouw *et al*., 2009; Scoon *et al*., 2017; Yao *et al*., 2021).

The Marginal Zone, which occurs intermittently throughout the BC, constitutes the lowermost portion of the RLS and has a thickness of up to ~800 m and consists primarily of fine- to medium-grained norite, peridotite, and pyroxenite (Cawthorn & Walraven, 1998; Yao *et al*., 2021)

The Lower Zone has a thickness of approximately 900-1600 m and typically contains rocks such as dunite, harzburgite and pyroxenite. The distribution and thickness of this zone is typically controlled by the floor topography and structure, with the thickest section developed within the Olifants River Trough in the Eastern Limb, where the stratigraphy is made up of a basal feldspathic pyroxenite with minor harzburgite, overlain in turn by a lower pyroxenite, a harzburgite subzone, and an upper pyroxenite (Cameron, 1978; Kiefer & Viljoen, 2006)**.**

The Critical Zone is approximately 1300 – 1800 m thick and is subdivided into the Lower and Upper Critical Zone. The Lower Critical Zone (LCZ) has a thickness of 700 – 800 m and consists primarily of orthopyroxenite. The LCZ hosts an average of 9 substantial chromitite layers, the Lower Group (LG1-LG7) and the Middle Group (MG1-MG2) chromitite layers. The Upper Critical Zone (UCZ) typically has a thickness of 520-1000 m and is distinguished by the presence of cyclic units and copious cumulus plagioclase, the latter which appears between the MG2 and MG3 chromitite layers at the base of an anorthosite layer. The cyclic units consist of ultramafic rocks (chromitite, and/or harzburgite, and/or pyroxenite) overlain by increasingly feldspathic rocks, beginning with norite followed by anorthosite (Maier *et al*., 2013; Voordouw *et al*., 2009; Eales & Cawthorn, 1996). The UCZ contains approximately five significant chromitite layers, The Middle Group (MG3-MG4) and the Upper Group (UG1-UG3) chromitite layers, with the UG3 occurring only in the Eastern Limb of the Bushveld Complex (Eales & Cawthorn, 1996). The UCZ is also well-known for its Platinum Group Element (PGE) mineralisation which occurs mainly in the economically significant Merensky

Reef and UG2 chromitite, as well as in the sub-economic Pseudo Reef (harzburgite) and Bastard Reef (pyroxenite)**)** (Kiefer & Viljoen, 2006; Maier *et al*., 2013).

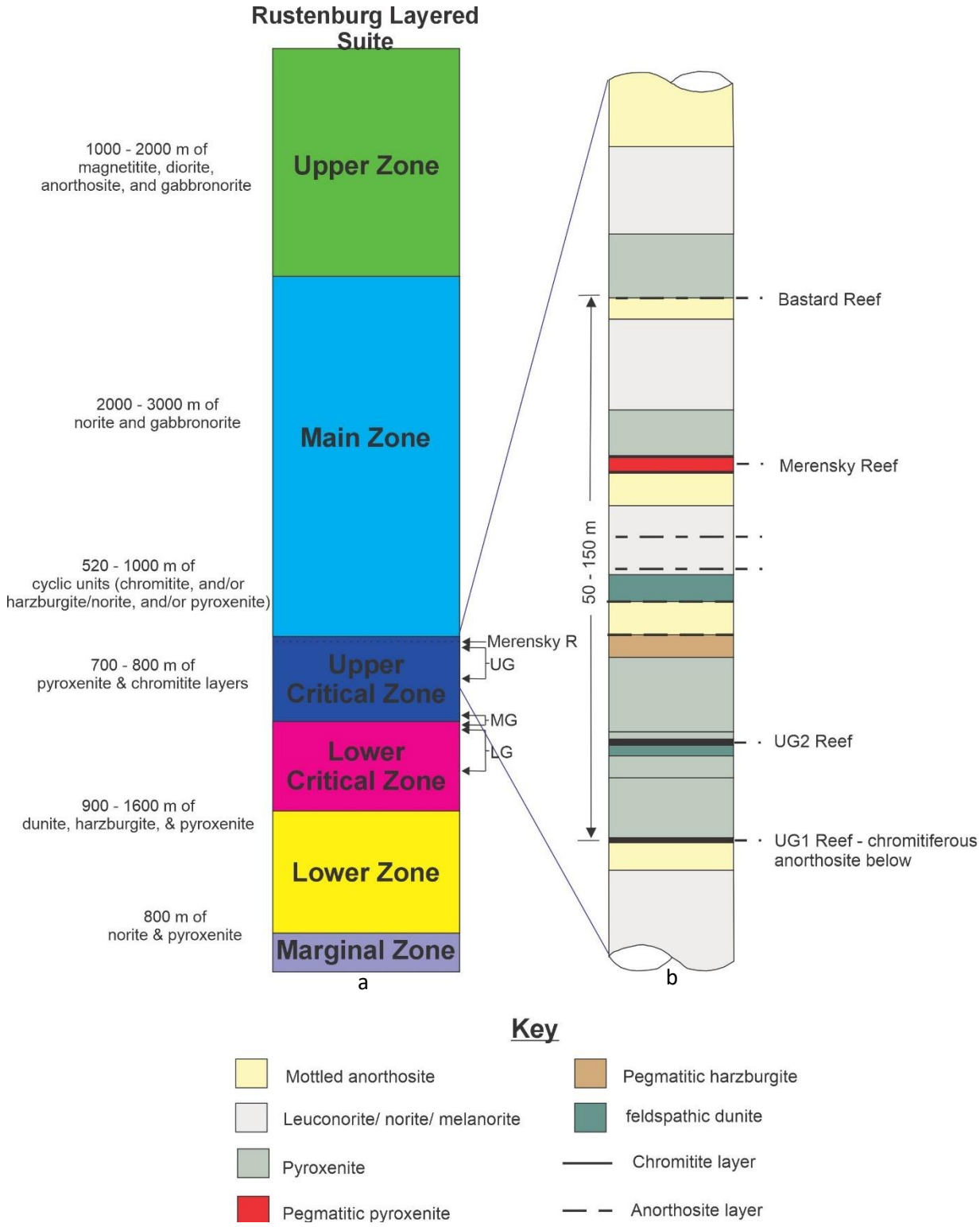

Figure 2: a) Generalized stratigraphy of the RLS with the different zones including the main thickness and the average depth of each division. b) Stratigraphy of the upper portion of the UCZ showing the position of the UG1 in relation to the UG2, Merensky, and Bastard Reefs in the Western Limb of the Bushveld Complex (right) (Nex, 2004; Smith *et al.,* 2004; Clarke *et al.,* 2009; Maier *et al.,* 2013).

The Main Zone is the thickest of all the zones, with a thickness of 2000 – 3000 m and occurs above the Bastard cyclic unit. It is composed mainly of massive norite and gabbronorite (Maier *et al*., 2013; Eales & Cawthorn, 1996). Layering within the Main Zone is not as well-developed as in the Critical Zone and it is also characterised by the absence of chromite and olivine. The Main Zone can be further divided into the Upper and Lower Main Zone (UMZ and LMZ), with the boundary defined by an ~3 m thick orthopyroxenite layer, the so-called Pyroxenite Marker, which records a significant reversal in initial Sr isotopic ratios (Molyneux, 1974; Mitchell, 1990; Nex *et al*., 1998; Yao *et al*., 2021; Magson *et al*., 2023).

The base of the 1000-2000 m thick Upper Zone of the RLS is marked by the appearance of cumulus magnetite. The zone hosts several magnetitite layers, up to 26 in the Western and Eastern limbs and 16 in the Northern Limb (Maier *et al*., 2013). The UZ has been divided into three subzones based on the cumulate mineral phases in this zone (Cawthorn & Walraven, 1998; Maier *et al*., 2013; Eales & Cawthorn, 1996). The first subzone, A, is characterised by the presence of cumulus plagioclase, low Ca-pyroxene, and magnetite. Subzone B is recognisable by the emergence of olivine as a cumulus phase, along with cumulus plagioclase, low Ca-pyroxene, and magnetite. Lastly, subzone C is characterised by the appearance of cumulus apatite along with various large country-rock xenoliths (Maier *et al*., 2013).

1.1.1 The Upper Group 1 chromitite layer (UG1)

The UG1 chromitite layer is the fourth significant chromitite layer above the base of the UCZ **(Figure 2)**. The UG1 typically comprises several chromitite layers interwoven with anorthosite, but it is also known to occur as a single layer in some areas. The chromite crystals encountered within the UG1 chromitite layer typically occur enclosed by oikocrystic plagioclase and orthopyroxene (Nex, 2004). The size of the chromite crystals varies depending on the abundance of interstitial silicates; crystals enclosed by silicates are often 0.1-0.2 mm in size. Chromitite crystals, where interstitial silicates are less, can be up to 2 mm in size (Nex, 2004).

The hanging wall to the UG1 chromitite layer consists of homogeneous pyroxenite with subsidiary interstitial feldspar. Towards the hanging wall's base, there are often euhedral clinopyroxene oikocrysts. Layered anorthosite and norite, with subsidiary pyroxenite and grading upward into a mottled anorthosite make up the immediate footwall of the UG1 chromitite layer. The mottled anorthosite hosts clinopyroxene oikocrysts, which commonly

contain cores of remnant cumulus orthopyroxene with a corona of oikocrystic clinopyroxene to form the mottled appearance (Nex, 2004).

The UG1 chromitite layer at the Dwars River Locality (DRL) on the Eastern Limb of the BC **(Figure 1)**, hosts one of the most striking exposures of bifurcating chromitite layers persisting for 10 s of meters along strike (Voordouw *et al.,* 2009; Pebane & Latypov, 2017). Unlike most underground exposures of the UG1 chromitite layer, at DRL it can be studied in 3-dimensions (Pebane & Latypov, 2017). For these reasons the DRL has received attention from numerous researchers (e.g. Cawthorn, 2003; Nex, 2004; Voordouw *et al.,* 2009; Cawthorn, 2015; Pebane & Latypov, 2017). Pebane & Latypov (2017) documented that the bifurcating chromitite layers at DRL are characterised by the splitting of one chromitite layer into two or more layers. These thinner layers typically converge after a few centimetres to meters along strike forming anorthosite lenses. The complexity of the bifurcations varies from those made of 2 – 3 chromitite layers to those made up of up to 10 layers of chromitite (Voordouw *et al.,* 2009). The chromitite layer from which these thinner layers emerge from or converge into has the same thickness to that of the combined thinner layers (Nex, 2004; Voordouw *et al.,* 2009; Pebane & Latypov, 2017).

1.2 Previous Studies

The origin of chromitite bifurcations has been studied by numerous researchers (Lee, 1981; Cawthorn, 2003; Nex, 2004; Voordouw *et al.,* 2009; Cawthorn, 2015; Mukherjee *et al.,* 2017; Pebane & Latypov, 2017; Nicholson, 2020; Maghdour-Mashhour & Hayes, 2021), and little consensus regarding their formation currently exists.

The first known study on chromitite bifurcations was published by Sampson (1932), who suggested that a residual melt, with a composition similar to that of chromite, intruded into weak points in the underlying anorthositic footwall (Pebane & Latypov, 2017). Lee (1981) argued a different mode of formation, suggesting that the density contrast between an overlying chromite-rich mush and underlying anorthosite was responsible for post-depositional deformation in the anorthosite **(Figure 3a-b)**. The chromite-rich mush is envisaged to have collapsed and to have filled pre-existing fractures in the anorthosite, which solidified laterally within those fractures resulting in the formation of chromitite bifurcations **(Figure 3c-d)** (Pebane & Latypov, 2017).

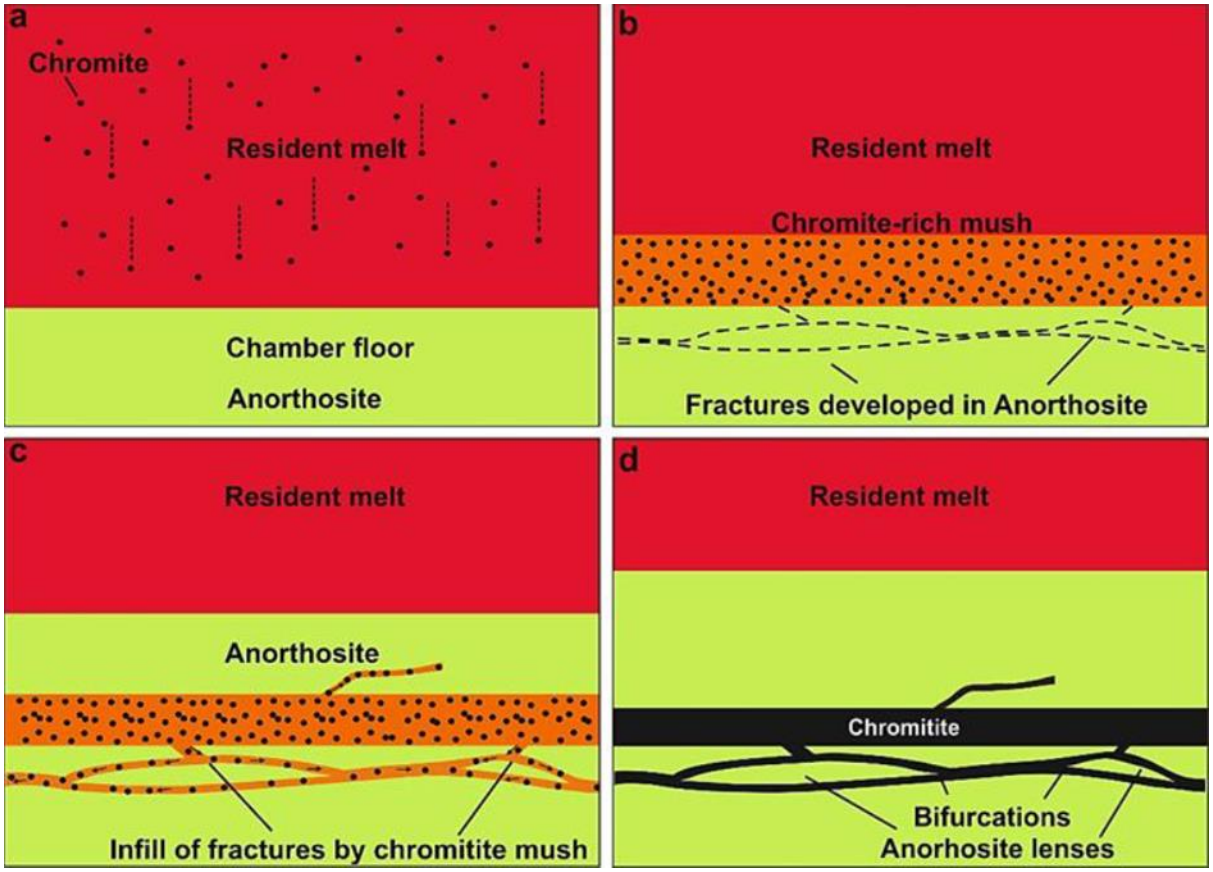

Figure 3: Intrusive model for the development of chromitite bifurcations developed by Lee (1981), as per Pebane & Latypov (2017). From Nicholson (2020).

Cawthorn (2003) subsequently argued that contrary to what Sampson (1932) and Lee (1981) suggested, chromitite bifurcations were formed in five stages: firstly, thin chromitite layers were formed above the anorthositic footwall **(Figure 4a-b)**. Secondly, an incomplete silicate layer formed over the chromitite layer due to in situ growth or descending convective cells, forming growth bulges and discontinuous silicate patches **(Figure 4c)**. Thirdly, the formation of another thin chromitite layer terminated the formation of these growth bulges and silicate patches, enclosing them as anorthosite lenses between two chromitite layers **(Figure 4d)**. In the fourth stage, more anorthosite patches/bulges are formed above the second chromitite layer. Lastly, the processes are repeated until a network of bifurcating chromitite layers has been formed (Cawthorn, 2003).

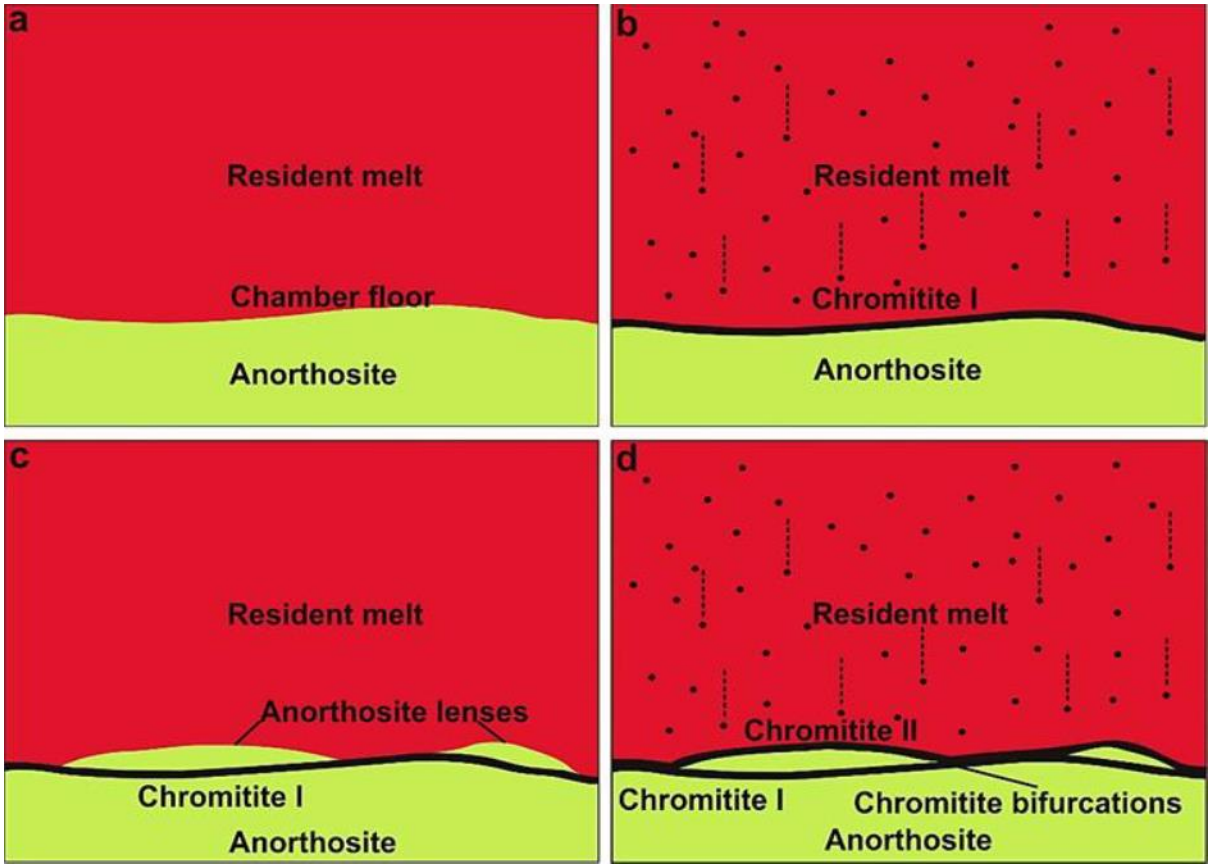

Figure 4: Depositional model for the development of chromitite bifurcations developed by Cawthorn (2003), as per Pebane & Latypov (2017). From Nicholson (2020).

Nex (2004) proposed that the origin of chromitite bifurcations could be explained by comparing their formation with that of sand volcanoes associated with seismic activity. This hypothesis suggests that lateral chromitite layers formed due to the influx of crustal-contaminated magma in the magma chamber. This influx was accompanied by substantial seismic activity, which led to the liquefaction of the underlying anorthosite, resulting in a plagioclase-rich mush **(Figure 5a-b)**. The mush extruded through the overlying chromitite layer to form anorthositic lenses, which were subsequently buried by further chromitite layers, resulting in chromitite bifurcations **(Figure 5c-d)**.

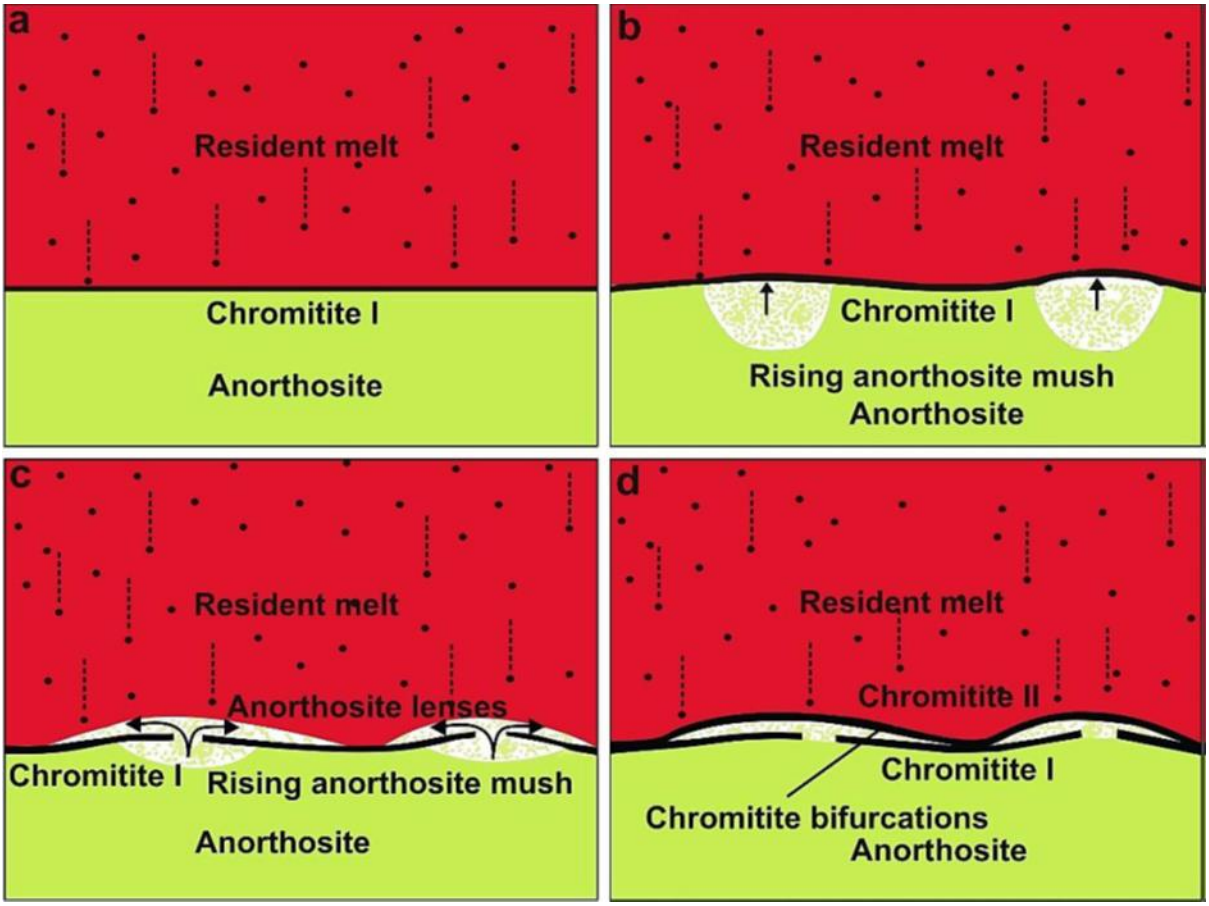

Figure 5: Depositional model for the development of chromitite bifurcations developed by Nex (2004), as per Pebane & Latypov (2017). From Nicholson (2020).

Voordouw *et al.*, (2009) suggested that chromitite bifurcations observed in the UG1 and UG2 were a result of chromite crystal slurries intruding into anorthosite. He proposed that the chromite-rich slurries accumulated in a structural trap. Afterwards, they were mobilised upwards through the Bushveld conduits and emplaced laterally along lithological contacts and structural weaknesses in the RLS **(Figure 6)**.

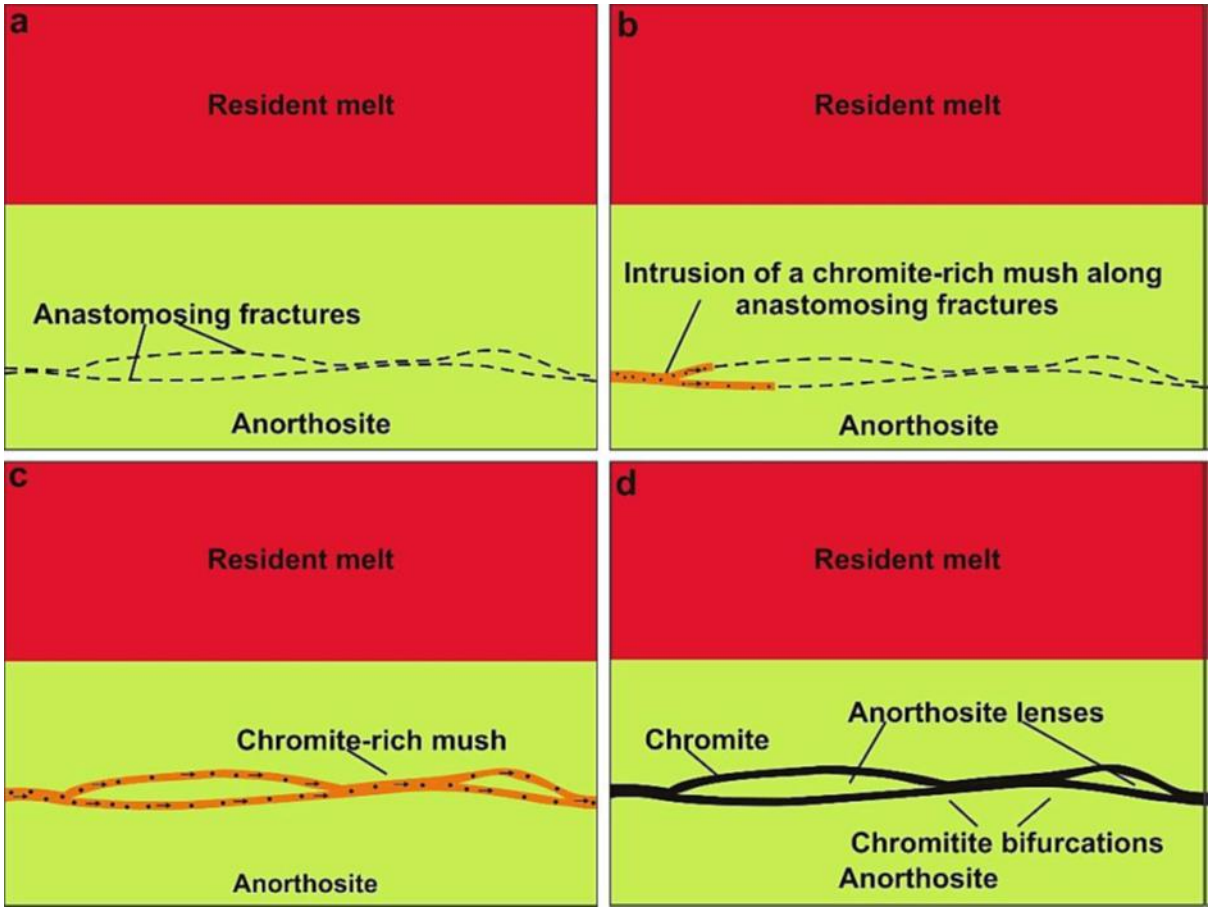

Figure 6: Intrusive model for the development of chromitite bifurcations developed by Voordouw *et al.* (2009), as per Pebane & Latypov (2017). From Nicholson (2020).

Cawthorn (2015) presented an alternative explanation for the genesis of chromitite bifurcations, proposing that seismic activity was responsible for the nucleation of chromite grains in the magma chamber. The accumulation of chromite on the chamber floor led to thin chromitite layers **(Figure 7a-b)**, and plagioclase grains accumulated above this due to inconsistent lateral flow rates in a plagioclase-laden suspension. A second thin chromitite layer was formed due to repeated seismic activity (second shock-induced chromite). This led to the formation of anorthosite lenses and chromitite bifurcations **(Figure 7c-d)**. Cawthorn (2015) surmised discontinuous anorthosite lenses were formed as a result of horizontally flowing plagioclase suspensions and the continuous chromitite layers accumulated due to seismic activity.

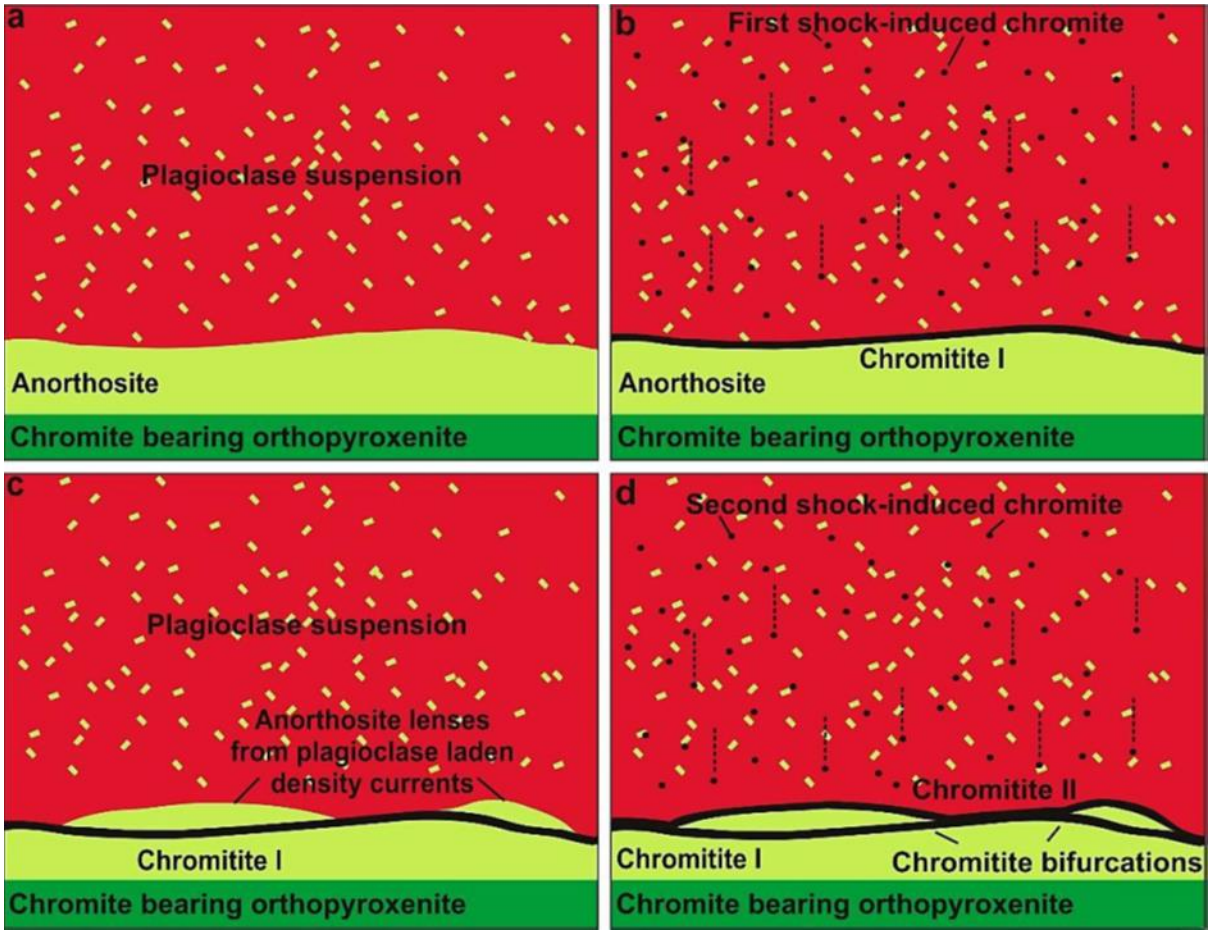

Figure 7: Depositional model for the development of chromitite bifurcations developed by Cawthorn (2015), as per Pebane & Latypov (2017). From Nicholson (2020)

The model formulated by Mukherjee *et al.,* (2017) is among the most recent models that attempt to explain the formation of chromitite bifurcations. However, the model was mainly intended to illustrate the formation of massive chromitite layers and not chromitite bifurcations. Mukherjee *et al.,* (2017) conducted detailed field and petrographic studies on a UG1 chromitite occurrence that extends into the anorthositic footwall from a chromitite pothole. The model argues that the magma chamber was filled with superheated melt, which was superheated by rapid adiabatic ascent. The subsequent cooling of the superheated melt resulted in chromite being saturated in the melt. It is speculated that the superheated melt might have caused thermo-chemical erosion of the floor cumulates resulting in the formation of potholes. Pebane & Latypov (2017) agree with this model because the chromitite layers intruded into the anorthositic footwall, which they claim supports field observations they made. The model suggests that the chromite-saturated melt percolated along weak points (pre-existing fractures) into the anorthosite layer **(Figure 8a-b)**. In situ chromite crystallisation then proceeded to take place in the eroded fractures from the continued flowing melt **(Figure 8c-d)** (Pebane & Latypov, 2017).

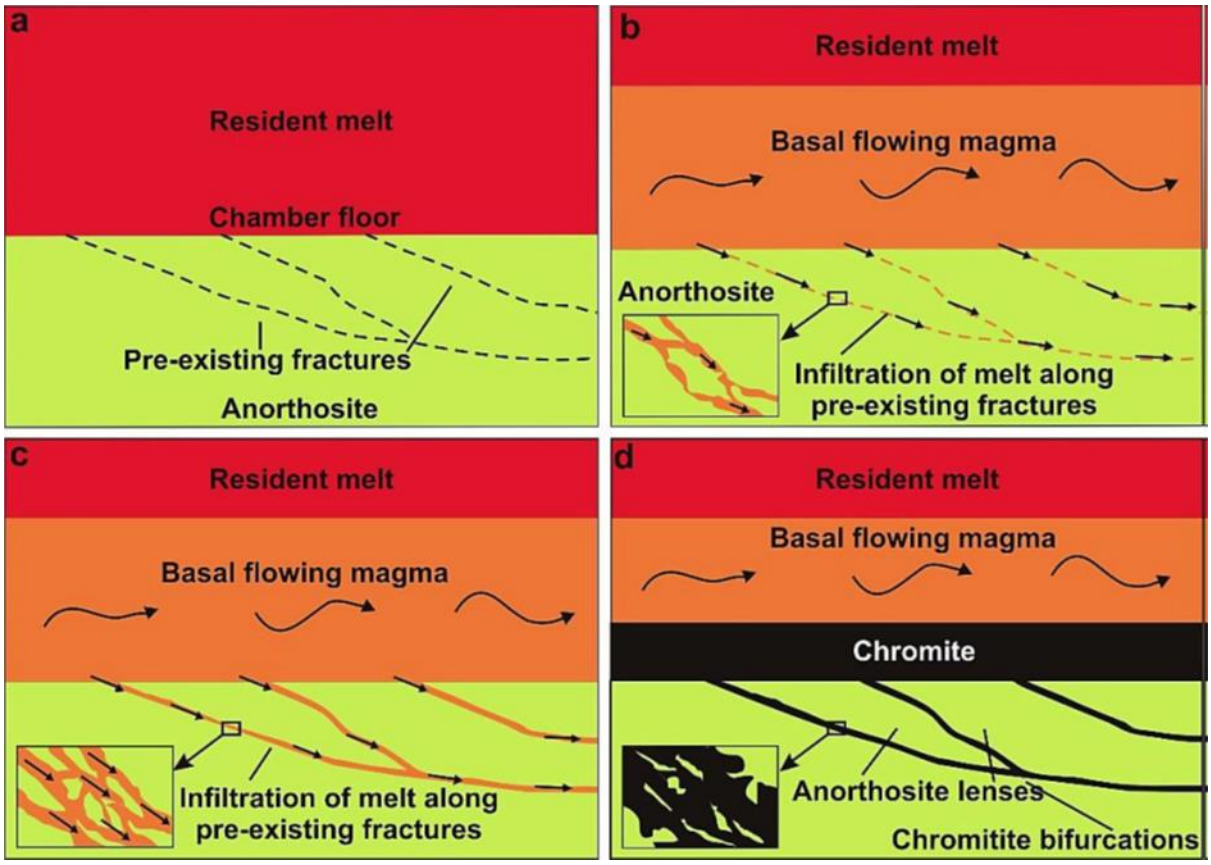

Figure 8: Intrusive model for the development of chromitite bifurcations developed by Mukherjee *et al.* (2017), as per Pebane & Latypov (2017). From Nicholson (2020).

The model of Pebane & Latypov (2017), claims that magmatic erosion played a significant role in forming chromitite bifurcations. This model suggests that a basal flow of dense superheated magma was emplaced in the magma chamber above anorthosite. The underlying anorthosite underwent thermo-chemical erosion due to the superheated magma. The magma then cooled to crystallise a chromitite layer above the irregular erosional surface until it was saturated in plagioclase **(Figure 9a)**. The magma then crystallised a continuous cumulate layer of plagioclase and chromite **(Figure 9b)**. A new superheated basal magma was subsequently emplaced, resulting in thermo-chemical erosion of the cumulates. The erosion was terminated at the underlying chromitite layer, and upon cooling, another chromitite layer was crystallised from the magma above the remaining anorthosite lenses and the underlying chromitite layer **(Figure 9c-d)**. This process resulted in the formation of chromitite bifurcations. It explains the formation of the anorthosite lenses, and the combined thickness of two bifurcating chromitite layers is equal to that of the chromitite layer into which they converge (Pebane & Latypov, 2017).

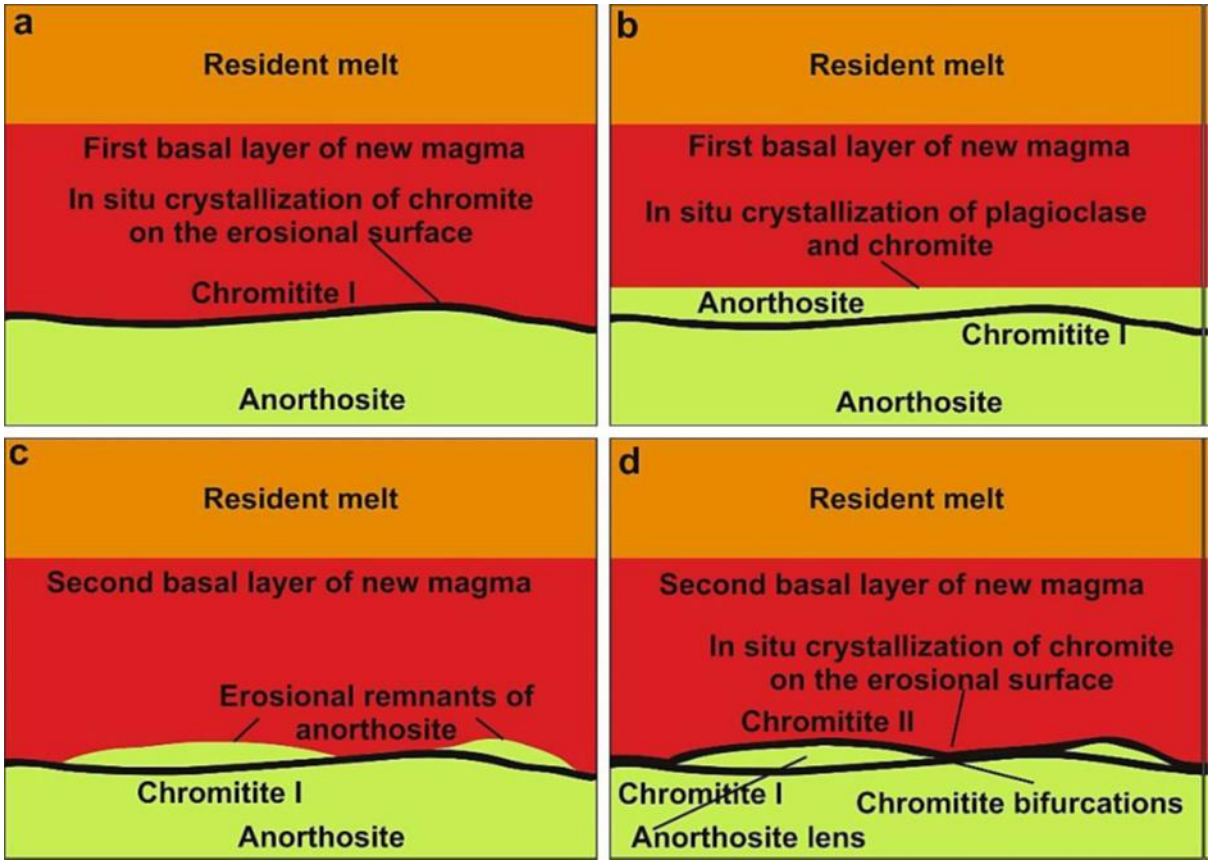

Figure 9: Erosional model for the development of chromitite bifurcations developed by Pebane & Latypov (2017). From Nicholson (2020).

Nicholson (2020) claimed that the models discussed above were typically, almost exclusively, based on field observations and did not rely sufficiently on petrological and geochemical investigations to explain the enigma which is chromitite bifurcations. Motivated by this fact, the study by Nicholson (2020) contains extensive field, petrological, and geochemical investigations to test the validity of the previously proposed models. Field investigations conducted provided evidence for thermo-chemical erosion in support of the erosional model. Petrographic investigations did not provide substantial information to support or refute the proposed models but revealed that fluids might have been present during crystallisation. However, the geochemical data collected did not favour any of the proposed models but indicated that several processes may have been involved in the formation of chromitite bifurcations. Nicholson (2020) concluded that more detailed geochemical investigations could provide more insight into the processes involved in the petrogenesis of chromitite bifurcations.

The most recent publication on the bifurcating nature of the UG1 chromitites was by Maghdour-Mashhour and Hayes (2021). They developed a model which proposes that the UG1 chromitite layers were formed when a fixed volume plagioclase slurry current, that was denser

than the resident magma in the developing chamber, was injected as a basal flow. The plagioclase laths that were entrained in this current settled at the base of the slurry, forming the anorthositic footwall. The remaining melt turbulently outran the deposited plagioclase slurry. As the current circulated, mixing of the resident magma and the frontal margins of the upper layer of the current occurred and generated a superheated chromium-saturated hybrid melt. The hybrid melt was injected back into the propagating current, resulting in the development of plume structures with rising buoyant plagioclase and descending packets of orthopyroxene crystals in the back of the current. The chromitite bifurcations observed in the UG1 occurred when the chromite precipitated from the cooling hybrid melt to form slurries that flowed and were caused to bifurcate by circulation of cells and granular vortices in the head of the current along with the developing plume structures at the back of the current.

2 Methodology

The samples used in this study were collected and prepared by Nicholson (2020). The samples were collected from an exposed anorthositic footwall of the UG1, Footwall 16 at Impala No. 11 Shaft near Rustenburg. The anorthositic footwall covers an area of approximately 195 m^2. This area was chosen because the anorthositic footwall displayed chromitite bifurcations that were different and much more complex than those at the Dwars River Locality (DRL) **(Figure 1)**. The anorthositic footwall also had reasonably thick chromitite bifurcations, which were critical for sampling.

The strategies behind the sample spacing and cut lengths were as follows:

(1) A single chromitite layer needed to be sampled separately from the two bifurcating chromitite layers. The sampling had to be done in this manner so that it would be possible to determine whether there are any differences in petrography, chemistry, and isotopic signatures between the two layers.

(2) The brittle nature of the footwall determined the cut lengths and how the samples would break if a cut were made at a particular area.

2.1 Sampling and sample preparation

Four sample cuts (D-A), each with a width of 10 cm and varying lengths, were sampled from the study area using a diamond saw **(Figures 10 and 11)**. Thirty-four polished thin sections **(Figure 12)** were prepared by Nicholson (2020), by attaching the samples to microscope glass slides with a 1:10 mixture of petropoxy 154 resin and 154 curing agents. Following lapping, the sections were polished using 3 µm diamond paste at approximately 300 rpm for about 5 minutes, and this was repeated using 1 µm diamond paste.

2.2 Petrography

Thirty-four thin sections were studied with the aid of an Olympus BX51 microscope, under both plane-polarised light (ppl) and cross-polarised light (xpl), to obtain petrographic data on the samples. The Altra 20 soft imaging system with Analysis Imager software, were utilised to obtain photomicrographs of the thin sections studied under the microscope.

Digitized Map of the Study Area

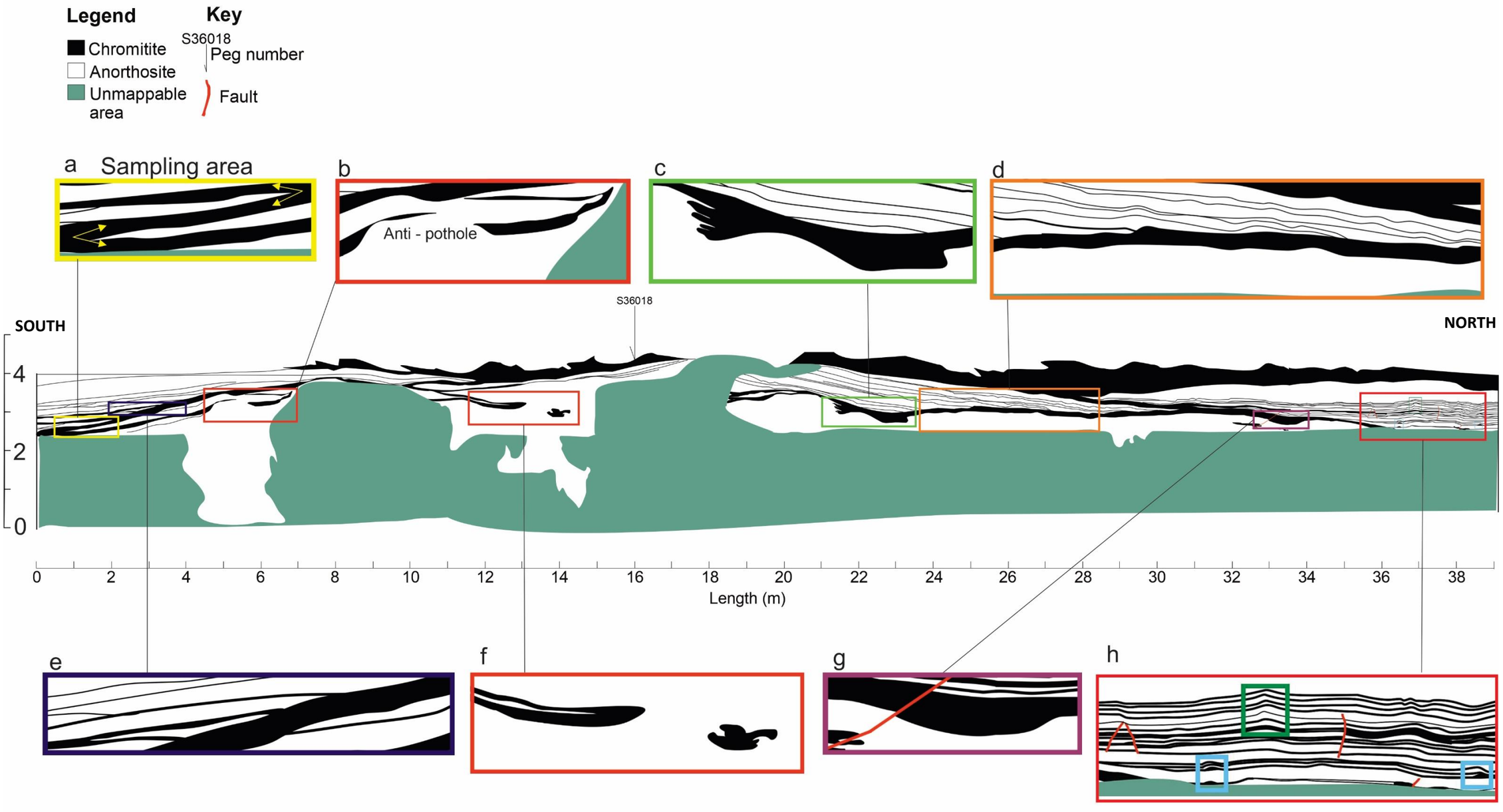

Figure 10: Digitised map of the study area. The black solid lines connect the areas of interest which have been enlarged for better visibility (from Nicholson, 2020).

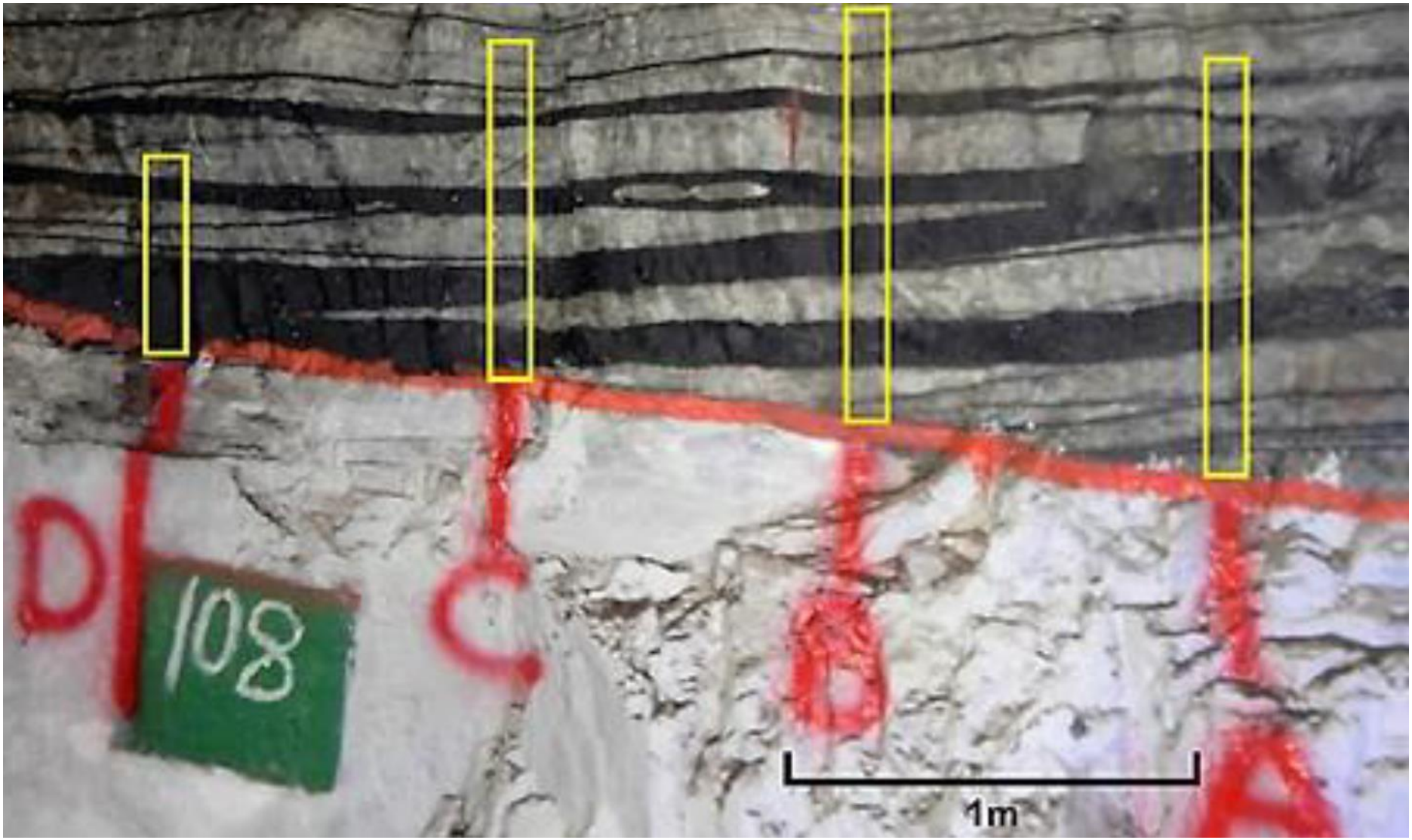

Figure 11: Image of Footwall 16 exposed at the Impala Platinum Limited No.11 Shaft, indicating the positions of sample cuts (from Nicholson, 2020).

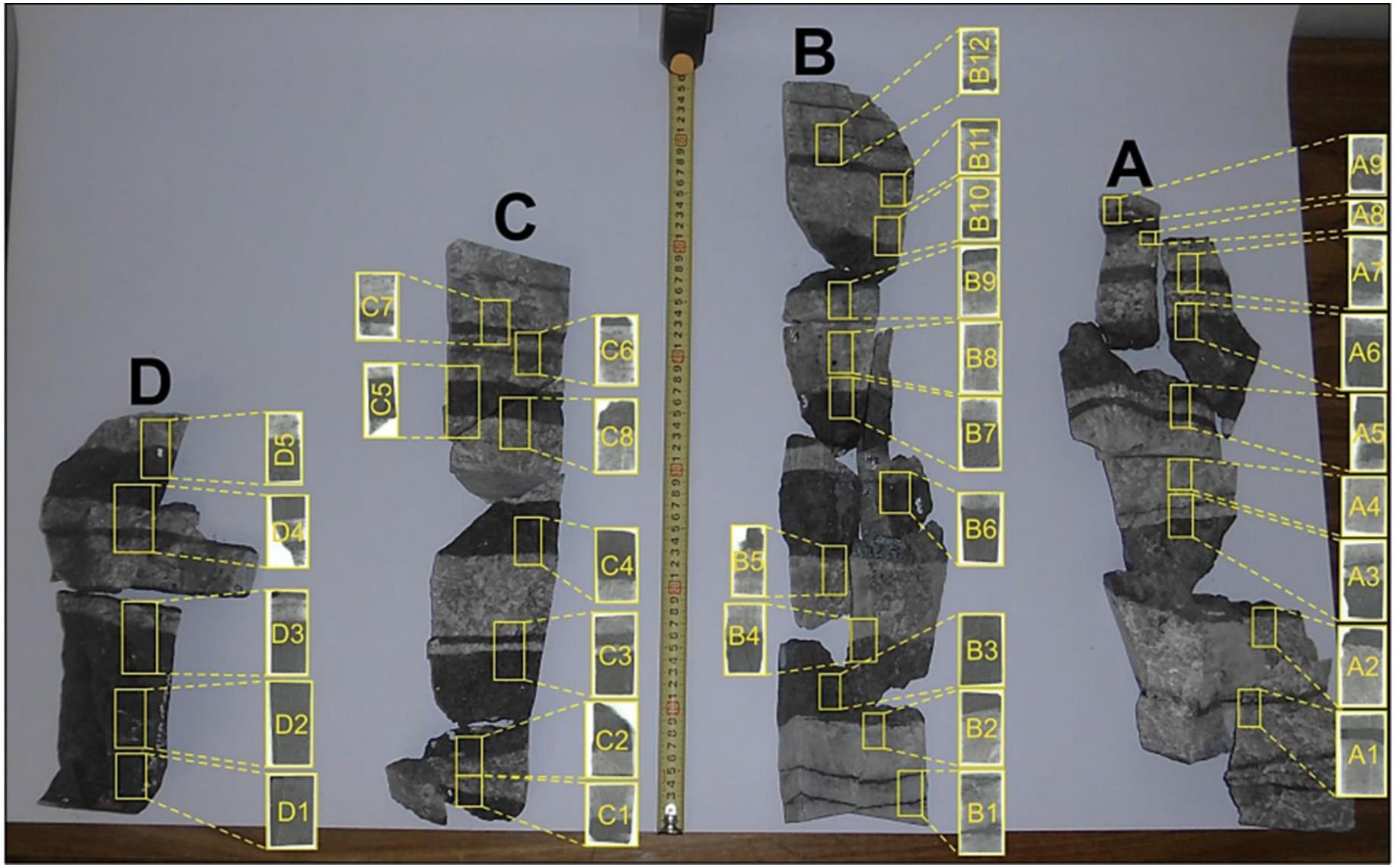

Figure 12: Sample cuts D-A, and the approximate location from which the 34 thin sections were made from each of the samples (from Nicholson, 2020).

2.3 Electron Microprobe Analysis

The CAMECA SX-100 Microprobe, equipped with four wavelength dispersive spectrometers (WDS) fitted with gas flow detectors, at the University of Johannesburg, was used to obtain the mineral chemistry of samples in the polished thin sections. The samples were analysed with the Electron Microprobe (EMPA) at 20 kV accelerating voltage and 20 and 40 nA electron beam current for the analysis of plagioclase and chromite, respectively. All the analysed elements **(Table 1)** were analysed on their Kα-lines.

Table 1: Elements analysed by EMPA in plagioclase and chromite crystals across the samples and the standards used for each element.

Plagioclase		**Chromite**	
Elements Analysed	**Standard***	**Elements Analysed**	**Standard***
Na	Jadeite	**Zn**	ZnS
Mg	Olivine	**Mg**	MgO
Al	Almandine	**Al**	Almandine
Si	Diopside	**Si**	Diopside
K	Orthoclase	**V**	V
Ca	Wollastonite	**Ca**	Wollastonite
Ti	TiO_2	**Ti**	TiO_2
Cr	Cr_2O_3	**Cr**	Cr_2O_3
Mn	Rhodonite	**Mn**	Rhodonite
Fe	Hematite	**Fe**	Hematite
Ni	NiO	**Ni**	NiO

*All the reference materials (standards) were natural substances apart from MgO, TiO_2, V, Cr_2O_3, NiO, and ZnS, which are synthetic.

To determine the plagioclase composition in the samples, three apparently cumulus (plagioclase in anorthosite layers) and intercumulus plagioclase (plagioclase in chromitite layers) crystals were each identified for analysis in all the thin sections. The plagioclase crystals chosen for EMPA were visually unaltered and individual crystals analysed were selected to ensure coverage of analyses across the thin sections **(Figures 13A and B)**. In some of the thin sections, where only one, either an anorthosite or chromitite layer and not both, was represented, three to four plagioclase crystals were chosen for analysis. Cross-polarised light (xpl) and backscattered electron (BSE) images were obtained for the analysed cumulus and intercumulus plagioclase crystals **(Figures 13C and D)**.

For chromite mineral chemistry, a single chromite crystal, per thin section, situated proximal to one of the cumulus plagioclase crystals were identified and analysed **(Figure 13C)**. One to three chromite crystals, within a chromitite bearing thin section, occurring proximal to the identified intercumulus plagioclase crystals were analysed **(Figure 13D)**. For each chromite

grain, only one spot was analysed. Backscattered electron images for all the analysed chromite grains were obtained.

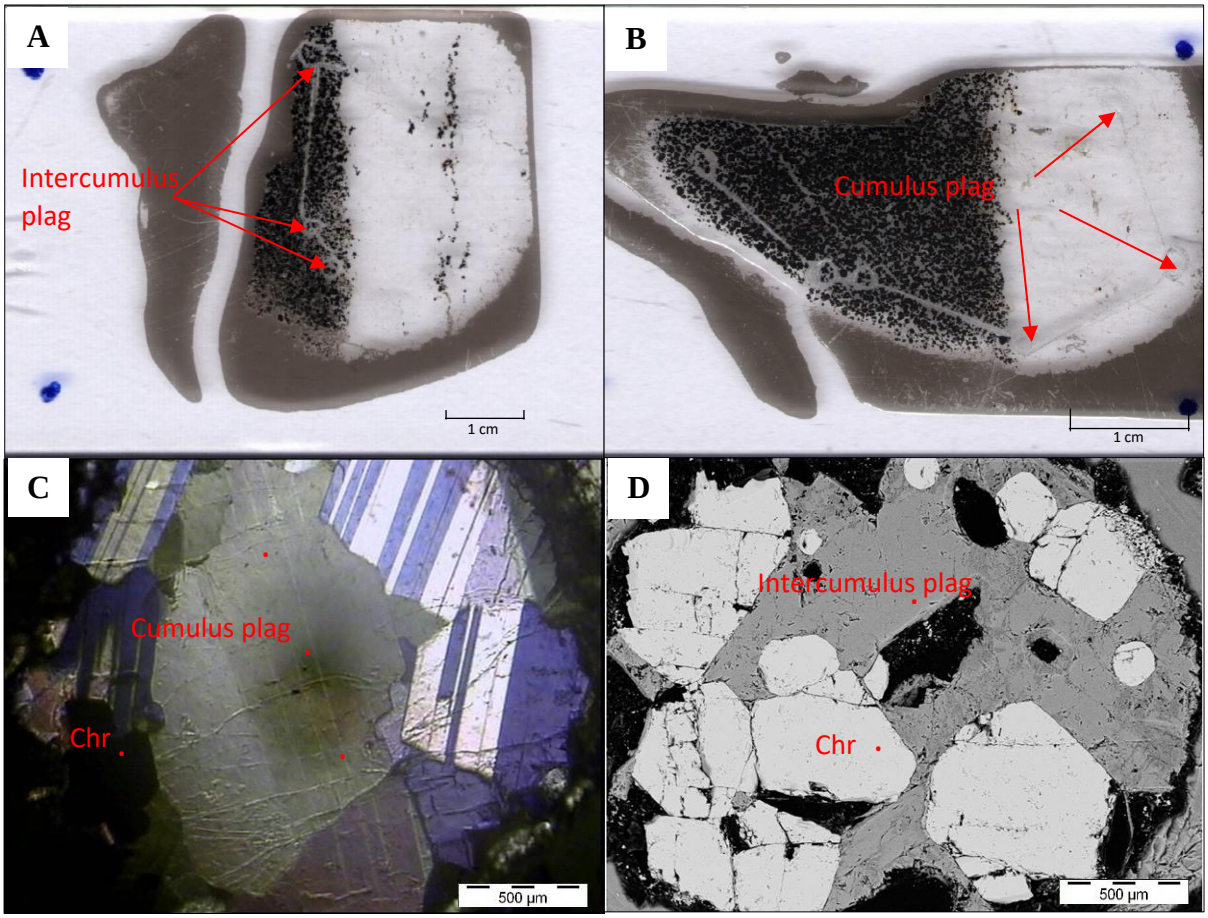

Figure 13: A-B) Flatbed scan images of thin sections with marks on the identified cumulus and intercumulus plagioclase crystals to be analysed. C) Xpl image of cumulus plagioclase crystal and chromite grain with red dots marking the spots that were analysed. D) BSE image of intercumulus plagioclase crystals and chromite grains with red dots indicating the spots that were analysed. plag = plagioclase, Chr = Chromite

3.1 Laser Ablation Multi – Collector Inductively Coupled Plasma Mass Spectrometry

In-situ Sr-isotopic analyses were carried out using the Nu Plasma II MC-ICPMS with 16 Faraday detectors and 5 ion counting detectors at the Spectrum Analytical Facility in the Geology Department at the University of Johannesburg. The instrument utilises a 193 nm ArF RESOlution SE excimer laser to ablate samples.

The analyses were executed by means of spot ablation on the 34 thin sections prepared by Nicholson (2020) on the same cumulus and intercumulus plagioclase crystals that EMPA was carried out on **(Figure 13A-B)**. An average of three spots were ablated on the cumulus plagioclase crystals, and one spot was ablated on the intercumulus plagioclase crystals. The plagioclase crystals were analysed for $^{87}Sr/^{86}Sr$ and $^{87}Rb/^{86}Sr$. Initial $^{87}Sr/^{86}Sr$ isotopic values

were calculated using an age of 2054.4 Ma (Zeh *et al*., 2015) with a decay constant of 1.39 x 10^{-11} y^{-1} (Nebel *et al.*, 2011). The standard errors for $^{87}Sr/^{86}Sr$ were propagated and multiplied by 2 to get the 2-standard error (2SE). The general conditions at which the instrument operated during the analyses are tabulated below **(Table 2)**.

Table 2: Conditions at which the Nu Plasma II MC-ICPMS operated during sample analysis

Plasma RF Power	1300 W
Coolant gas flow	13 L/min
Auxiliary gas flow	0.80 L/min
Nebuliser gas flow	0.9 L/min
Laser He carrier gas flow	0.31 L/min

The plagioclase crystals were ablated for 60 seconds with spot sizes ranging between 80 – 100 µm for cumulus plagioclase crystals and 60 – 100 µm for intercumulus plagioclase crystals. The spot sizes differed depending on the surface area available in each sample. The settings used to obtain the Sr-isotopic measurements are in the table below **(Table 3)**:

Table 3: Laser ablation settings utilised when obtaining Sr-isotopic measurements

Beam Energy	**Beam Attenuation**	**Repetition Rate**	**On-sample Fluence**	**Integration Time**
6 mJ	50 %	6 Hz	3.5 J/cm^2	0.2 sec

A blank signal was measured for 20 seconds on peak positions before ablation of the sample was initiated; the blank signal was subtracted from the ablation signal to get blank-corrected intensities.

The $^{86}Sr/^{88}Sr$ ratio of 0.1194 was used for mass bias correction, to calculate and correct Sr mass fractionation. ^{87}Rb was calculated from ^{85}Rb after the mass bias correction, and to obtain ^{87}Sr, the ^{87}Rb was subtracted from the total signal at mass 87. Reference glass BHVO2G (Elburg *et al.,* 2005) was regularly analysed to correct Rb mass fractionation through the regular adjustment of the Sr correction factor. BHVO2G ($^{87}Sr/^{86}Sr$ ~ 0.70347) and an in-house plagioclase glass standard ($^{87}Sr/^{86}Sr$ ~ 0.7072) were used as secondary standards to evaluate the accuracy of the measurements, by ablating them after every 10 – 15 measurements **(Appendix D: Table D-3 Figure D1 & 2)**. The standards were ablated using the same setting as the samples **(Table 2)**, except the spot size was fixed to 100 µm. The subtraction of ^{84}Kr and ^{86}Kr from ^{84}Sr and ^{86}Sr was used to correct for Kr interference during the blank correction.

3 Results

3.1 Field Observations

The study area displays a complex network of bifurcating chromitite layers with anorthosite in between **(Figure 10)**. At the base there is a thick uneven anorthosite layer that is capped with a relatively continuous chromitite layer, with both having varying thicknesses laterally. The basal chromitite layer also has a substantial thickness and is relatively discontinuous and appears to be penetrated locally by the underlying layer of anorthosite. A thick upper chromitite layer that is connected to the basal layer by what appears to be several offshoots is developed at the top of the studied exposure **(Figure 10)**. The area between these two thick chromitite layers does not only exhibit bifurcating chromitite layers, but it also has other interesting features such as, anorthosite inclusions within chromitite layers **(Figure 14)**, pothole-like chromitite structures **(Figure 15)**, along with faults and plastically deformed chromitite layers.

The anastomosing chromitite layers forming the bifurcations appear to merge with the chromitite layer at the top of the study area and the layer above the base anorthosite layer **(Figure 10d)**. There are several chromitite layers that are thicker than the bifurcating layers, which run diagonally and connect the uppermost and lowermost chromitite layers in the study area. The study area commonly exhibits chromitite layers proximal to each other, bifurcating in different directions **(Figure 10a)**. In areas where two chromitite layers bifurcate from a single chromitite layer, their combined thicknesses are equal to that of the single merged layer **(Figure 10a)**. In some instances, where the bifurcations are more complex and there are multiple bifurcating layers (which also merge with other bifurcating layers) merging into a single chromitite layer, the combined thickness of the individual layers do not correspond to that of the merged chromitite layer **(Figure 10e)**. There are also very thin chromitite layers between the two thick chromitite layers at the base and the top of the study area. On the northern side of the study area there are thin concordant chromitite layers that can be observed **(Figure 10h)**.

Circular and elongated anorthosite inclusions of varying sizes occur within some of the chromitite layers **(Figure 10 & 14)**. These inclusions locally disturb the chromitite layers by causing them to bulge and therefore increase the thickness of the layer where they occur **(Figure 14a & b)**. In other cases, the inclusions do not cause much disturbance in the host chromitite layer, and the thickness of the layer is virtually unaffected **(Figure 14c)**.

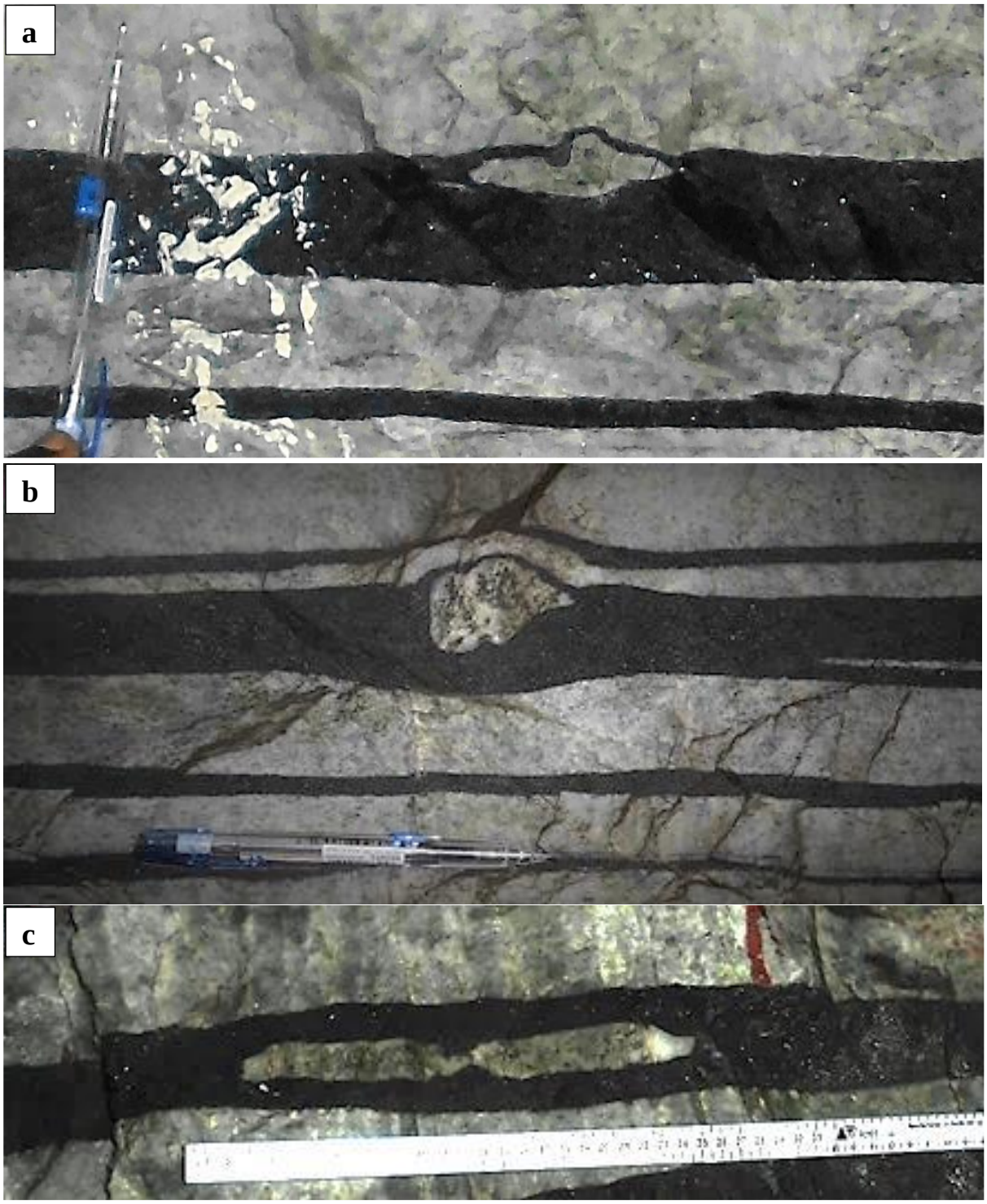

Figure 14: a) Elongated anorthosite inclusion disturbing the host chromitite layer. (b) Circular anorthosite inclusion causing disturbance to the host chromitite. (c) Elongated anorthosite inclusion in an undisturbed chromitite layer (from Nicholson, 2020).

There are certain parts in the study interval that have experienced brittle and ductile deformation. The evidence of brittle deformation can be observed in the presence of normal **(Figure 10g)** and reverse **(Figure 10h)** faults within the study area. Where there are faults, displaced chromitite layers are overlain by uninterrupted layers of chromitite. Ductile deformation is evident in plastically deformed and partly split chromitite layers **(Figure 10b & f)**.

There are two pothole-like structures within the study area, both of which are chromitite depressions; the first structure has a semi-rectangular form **(Figure 10c)**, while the second structure has a semi-circular form **(Figure 10g and Figure 15)**. What might be an anti-pothole can also be observed where an anorthosite mound stands above the normal level of a chromitite layer **(Figure 10b)**.

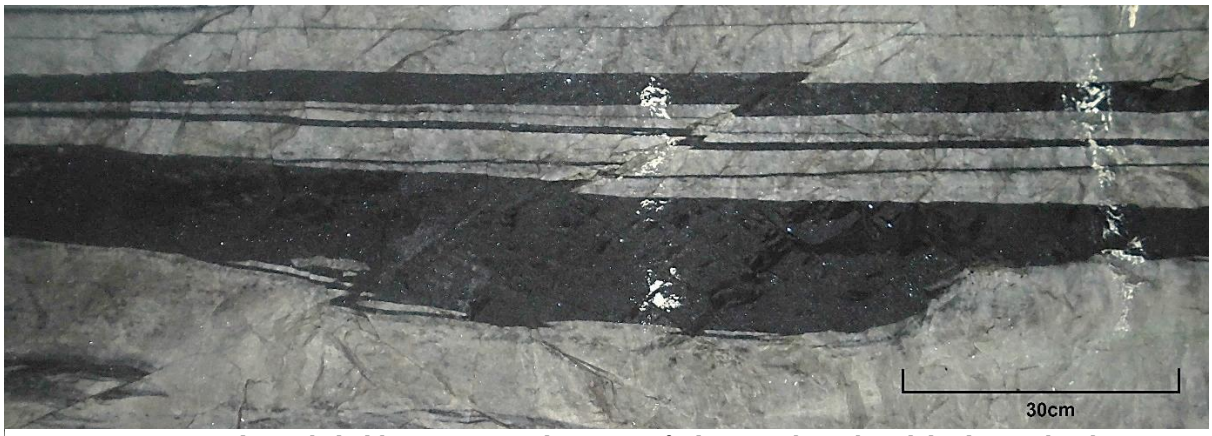

Figure 15: Semi-circular pothole-like structure and a reverse fault going through and displacing the chromitite – anorthosite layers (from Nicholson, 2020).

Some of the thin chromitite layers have been observed with upwards curving structures in the same lateral position in the study area, but at various stratigraphic heights **(Figure 10h; green box)**. In some instances, instead of curves, some of the chromitite layers form bulges among the layers forming curved structures **(Figure 10h; blue boxes)**.

3.2 Petrography

The results obtained from the petrographic analysis of the 34 thin sections are presented below for the whole group of thin sections and not as individual sections to prevent redundancy; Most of the thin sections are primarily similar, as they contain the same lithologies (anorthosite and chromitite). The caption below each of the figures contains the thin section number after the

description for all the thin sections presented below. The modal mineralogy for the individual thin sections is provided in Appendix A.

3.2.1 Anorthositic host rock

The anorthositic host rock in the study contains, on average, less than 80% plagioclase and should therefore be strictly termed leucogabbros, leuconorites or leucogabbronorites depending on the ratio of clino- to orthopyroxene. However, due to historical usage, in this study these rocks will still be referred to as anorthosites. Cumulus plagioclase (~ 78%) constitutes most of the anorthositic host rock throughout sample cuts A, B, C, and D.

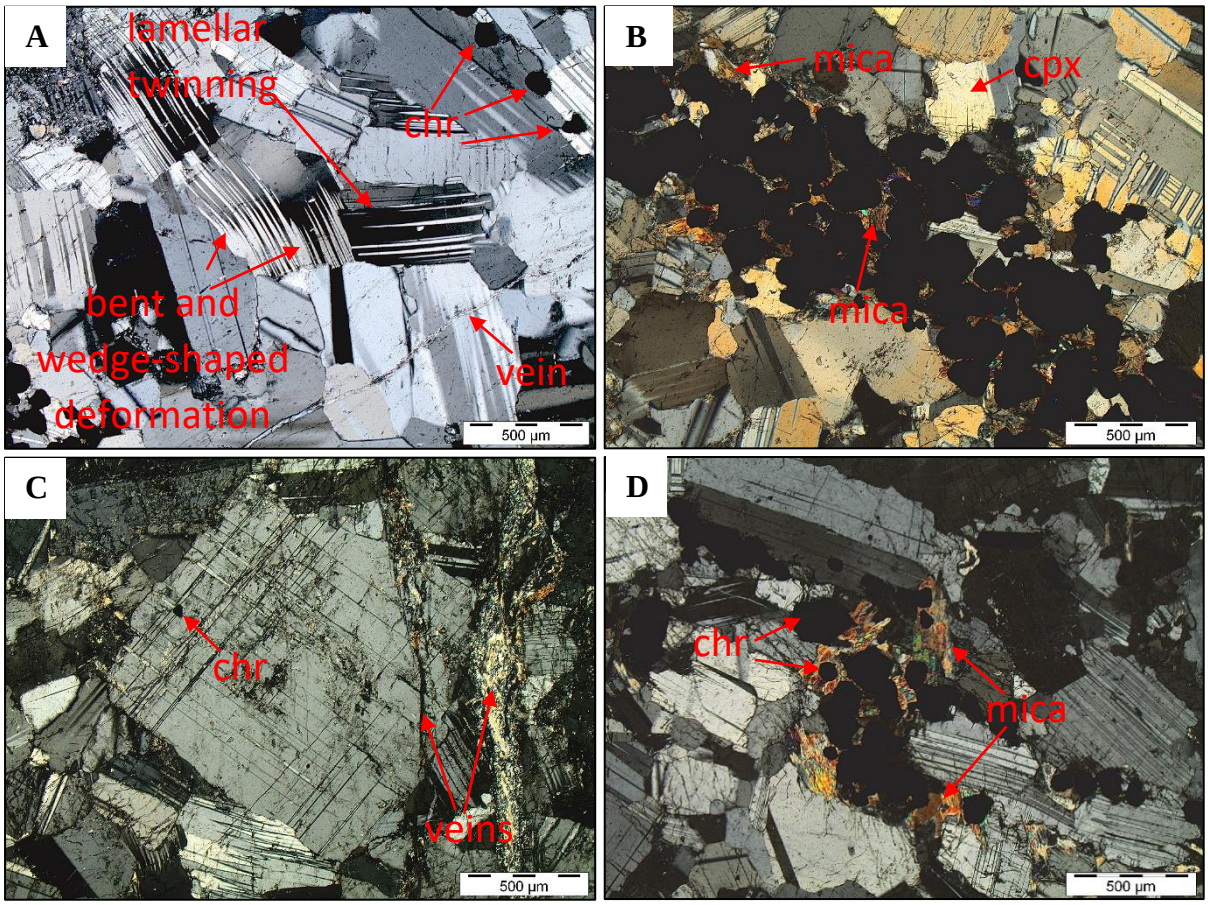

Figure 16: Photomicrographs of anorthosite taken under cross polarized light. A) Bent and wedge-shaped deformation twins in plagioclase with a vein cutting through plagioclase and chromite crystals within plagioclase and between plagioclase boundaries (B7). B) Thin chromitite layer cutting through an anorthosite layer and cpx crystal (B12). C) Vein cutting though an opx crystal with narrowly spaced exsolution lamellae of cpx (A3). D) Chromite crystals interspersed with mica (A8). Chr = chromite.

The anorthosite also contains clinopyroxene (~12%), mica (~4%), chromite (~4%), orthopyroxene (~2%) and some subsidiary quartz. The plagioclase crystals are predominantly subhedral to euhedral, with varying crystal sizes across all the samples. The plagioclase crystals exhibit mainly three variations of lamellar twinning *viz.* bent twins, wedge-shaped deformation twinning, and normal lamellar twinning **(Figure 16A)**. Some of the plagioclase crystals also exhibit undulatory extinction.

Clinopyroxene occurs primarily as anhedral crystals and as intergranular crystals between plagioclase crystals **(Figure 16B)**. Orthopyroxene is encountered across the study interval as subhedral to anhedral, medium-grained crystals. It occurs interstitial to plagioclase and often exhibits narrowly spaced exsolution lamellae of clinopyroxene **(Figure 16C)**. Mica minerals observed throughout the samples are phlogopite, which occurs interspersed throughout the anorthosite, showing reddish-brown pleochroism **(Figure 16B & D)**. Chromite crystals occur in a few different ways throughout the anorthositic samples, as dispersed mineral crystals at boundaries of plagioclase grains or enclosed within plagioclase and sometimes orthopyroxene crystals, clustered together, or as thin layers **(Figures 16A-D)**. The grouped chromite crystals and thin chromite layers are closely associated with clusters or large phlogopite crystals **(Figures 16B & D)**.

Features such as veins and fractures can be observed in some anorthositic samples. These veins and fractures are always filled with massive or polycrystalline epidote, and sometimes both. The veins appear to cut through both single and multiple plagioclase crystals. The veins have also been observed cutting through orthopyroxene **(Figures 16A & C)**.

3.2.2 Anorthosite-chromitite contacts

At the anorthosite-chromitite contacts, plagioclase often has a fractured appearance. The contacts between the anorthosite and chromitite layers are typically gradational as the cumulus plagioclase, and chromite crystals overlap at the contacts **(Figure 17A-D)**. The chromite varies in crystal size, with a higher concentration of smaller crystal sizes observed near the contact. The concentration of larger crystal sizes increases further from the contact towards the chromitite layer.

Locally, phlogopite that is encountered at the contact occurs as interstitial minerals between chromite crystals **(Figures 17A-B)**. Some of the cumulus plagioclase crystals occurring at the

contacts have been altered and fractured, especially those in proximity to the veins; the intercumulus plagioclase also exhibits alteration. At some of the contacts, veins can be observed. The veins either run parallel or perpendicular to the contact, some of them do not

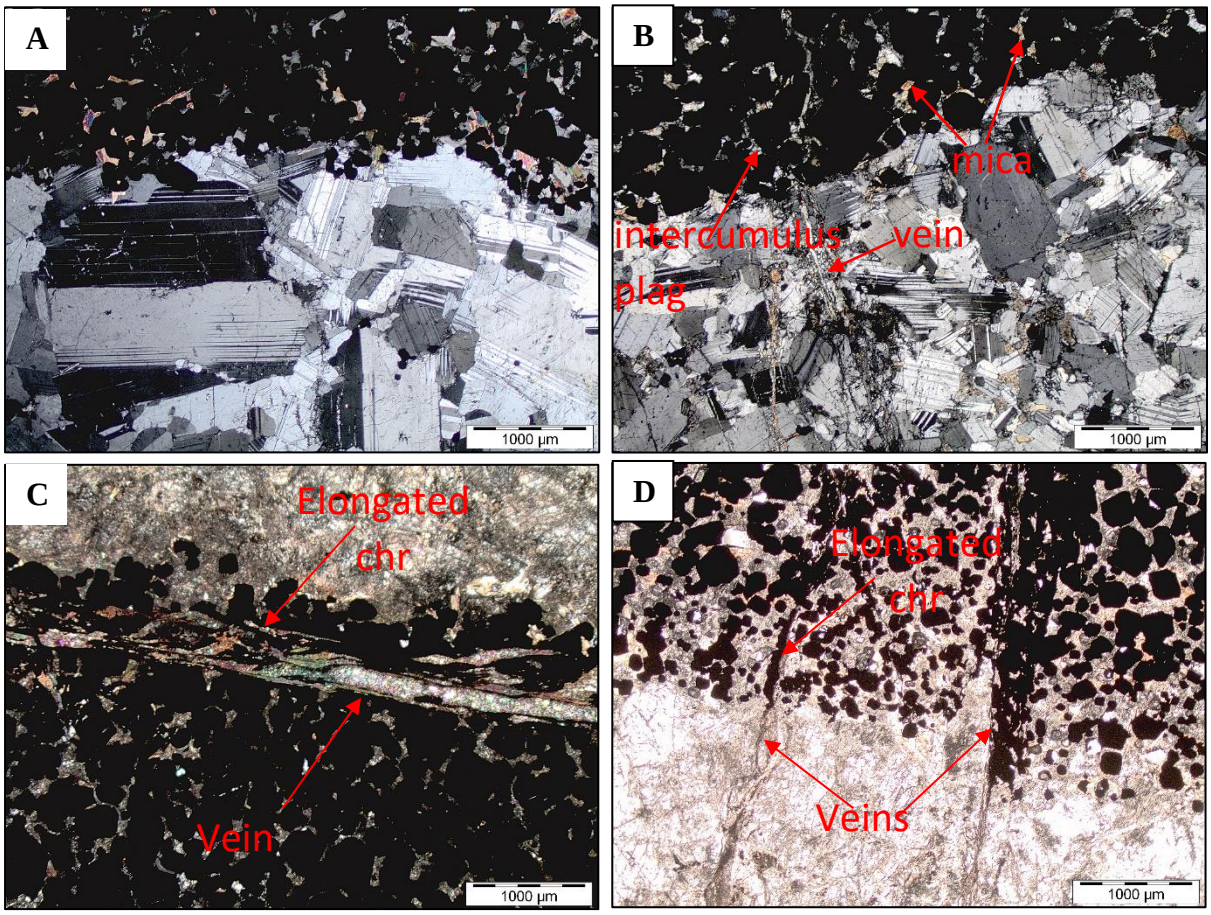

Figure 17: Photomicrographs of anorthosite-chromitite contacts A) Gradational contact; mica interstitial to the chromite crystals and intercumulus plagioclase crystals under cross polarized light (A1). B) Gradational contact with a vein cutting through multiple minerals and fractured minerals near the vein under cross polarized light (B6). C) Vein running parallel to the contact and elongated chromite crystals under cross polarized light (A2). D) Veins perpendicular to the contact and elongated chromite crystals under plane polarized light (B4). Chr = chromite

enter the chromitite layer and others terminate within the chromitite layer but close to the contact. The chromite crystals that are in close proximity to the veins have been elongated, while the plagioclase crystals have been severely altered and fractured compared to those further from the veins **(Figure 17C-D)**

3.3 Chromitite layers

Chromitite occurs as relatively thick massive layers and as smaller layers that occur within the anorthosite layers. The chromitite layers are predominantly composed of chromite (~60%), along with plagioclase (~25%), phlogopite (~10%), clinopyroxene (~3%), and orthopyroxene (~2%), which mainly occur interstitially to the chromite crystals. The chromite appears as

subhedral to euhedral cumulus crystals, varying in crystal size throughout the chromitite-bearing samples **(Figure 18A-D)**.

Fine crystalline plagioclase occurs throughout the chromitite layers between the chromite interstices **(Figure 18A & C)**. Phlogopite crystals occur sporadically throughout the chromitite host rock showing reddish-brown pleochroism **(Figure 18A-D)**. Pyroxenes also occur intermittently as fine-grained crystals within the fine mass of intercumulus plagioclase. Sometimes, veins can be observed intersecting perpendicularly with smaller chromitite layers,

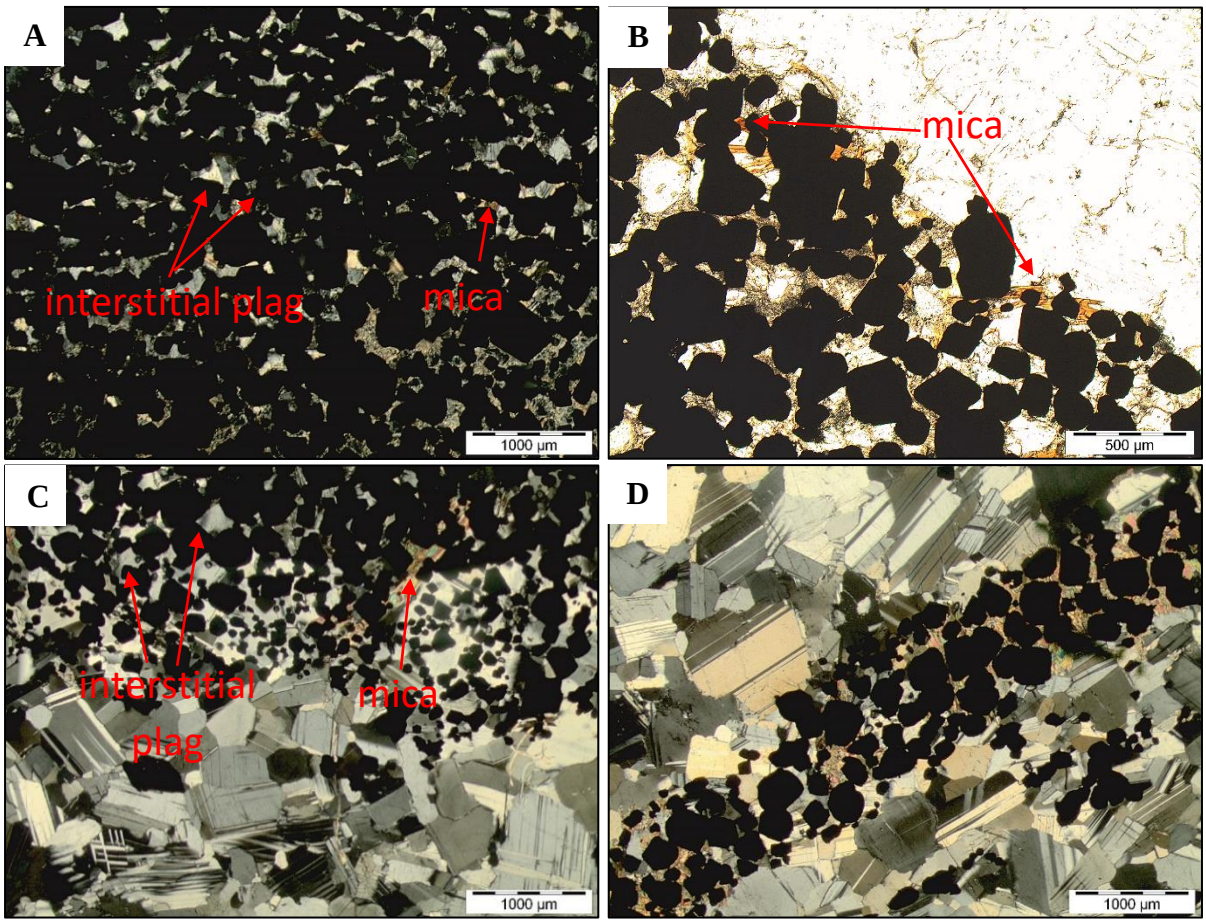

Figure 18: Photomicrographs of chromitite occurring in the different samples. A) Chromitite with interstitial plagioclase; and phlogopite occurring between chromite crystals under cross polarised light (C2). B) Phlogopite interspersed with chromite crystals in plane polarised light (B12). C) Chromite crystals at a gradational contact between a chromitite and an anorthosite layer, grading from smaller to larger crystals; and a large phlogopite crystal near the contact under cross polarized light (C3). D) Thin chromitite layer within anorthosite under cross polarized light (C6).

which occur within the anorthositic host rocks. These micro veins do not cut the chromitite layers completely but terminate near the contact **(Figures 17B & 18B).**

3.4 Mineral chemistry

3.4.1 Plagioclase

Plagioclase occurs in both the anorthositic host rocks and the chromitite layers; in the latter, it occurs as an intercumulus mineral and in the former as the primary mineral phase. For the analysis of plagioclase, the following elemental oxides were analysed: SiO_2, TiO_2, Al_2O_3, Cr_2O_3, $FeO_{(Total)}$, MnO, MgO, CaO, NiO, Na_2O, and K_2O. The results are graphically presented in the An-Ab-Or ternary diagram **(Figures 19 & 20)**, in depth profiles **(Figure 21-24)**, to show how the An% and major element oxides vary across the chromitite bifurcations and in binary variation diagrams to illustrate the variation in major element oxides with An% **(Figure 25)**. Plagioclase compositional data are presented in Appendix B, Tables B1 and B2. The anorthite content was calculated using: An% = 100 × molar Ca / (Ca + Na + K).

The analyses of cumulus plagioclase crystals revealed that the composition of An ranges between 64,21 – 83,92%, Ab between 15,75 – 34,45%, and Or between 0,12 – 1,70%. Most cumulus plagioclase crystals fall within the bytownite range, while a few are in the labradorite range **(Figure 19)**. The intercumulus plagioclase analysed yielded results with compositions of An between 2,26 – 98,58%, Ab between 1,41 – 97,69%, and Or between 0,01 – 0,53%. The majority of the intercumulus plagioclase is in the bytownite range. A substantial amount of the intercumulus plagioclase also occurs in the oligoclase range (sample cuts A and B), followed by lesser numbers in the labradorite range (sample cuts A, B, C, and D), and the least in the anorthite range (sample cuts A, B, and C) **(Figure 20)**. Table 4 below contains the averages and standard deviations for An% in the cumulus and intercumulus plagioclase for each sample cut.

Table 4: Average An% and ranges of cumulus and intercumulus plagioclase in sample cuts A-D. Uncertainty in average An% values expressed as 1 standard deviations.

Sample cuts	**A**		**B**		**C**		**D**	
Cumulus Plagioclase								
Average	73,85 ± 1,89		74,32±1,44		74,26±1,93		75,10 ± 3,27	
Range	64,21 – 78,98		71,84 – 81,85		69,26 – 80,68		69,80 – 83,92	
Intercumulus Plagioclase								
Average	5,40 ± 2,96	80,55 ± 7,13	79,16 ± 7,48	9,32 ± 4,28	–	80,64 ± 7,10	–	73,63 ± 3,09
Range	2,26 – 10,26	66,12 – 90,13	3,03 – 16,81	66,14 – 98,58	6,27	66,44 – 92,05	8,77	68,11 – 81,33

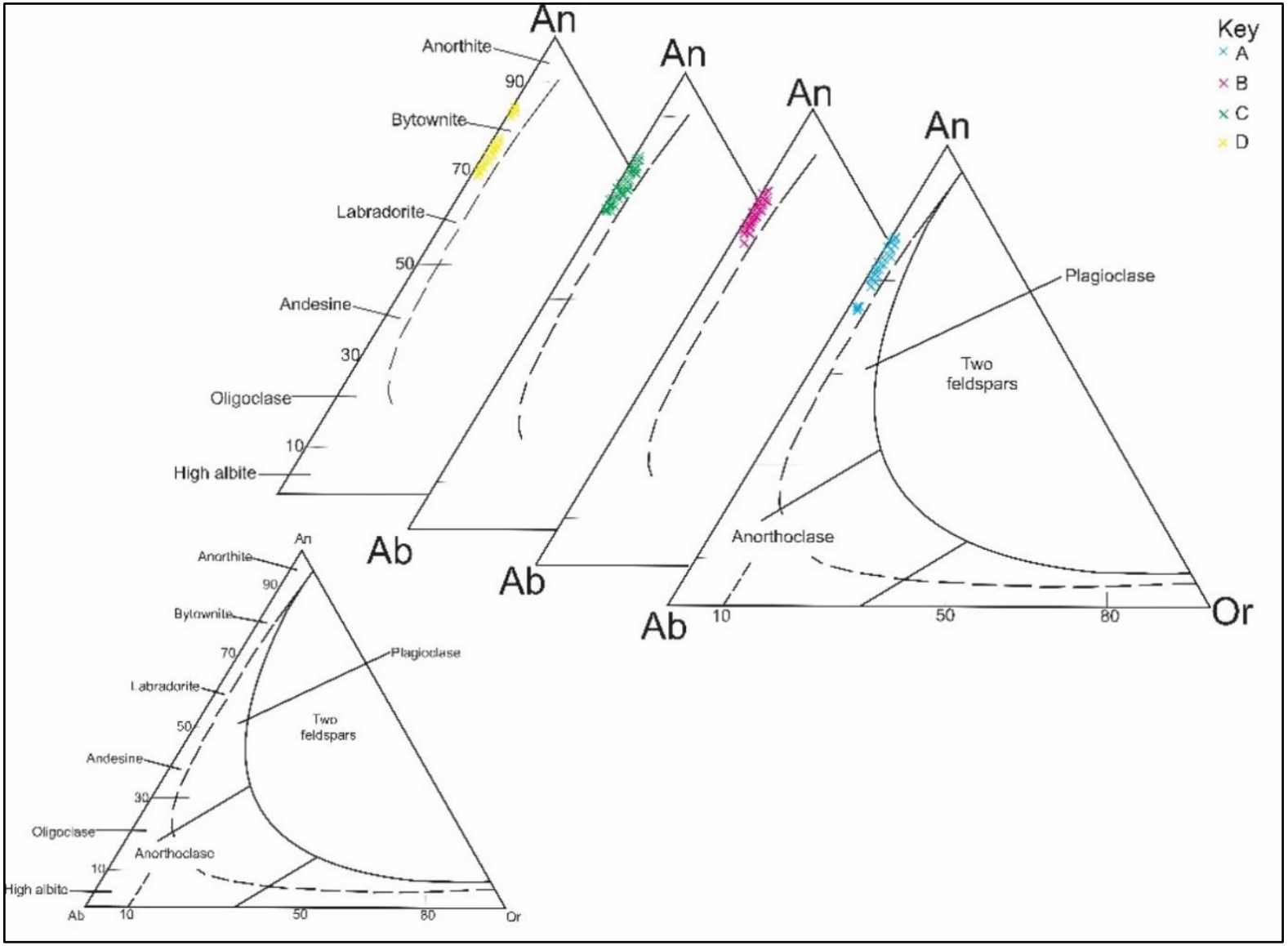

Figure 19: Ternary diagram showing cumulus plagioclase compositions for sample cuts D-A.

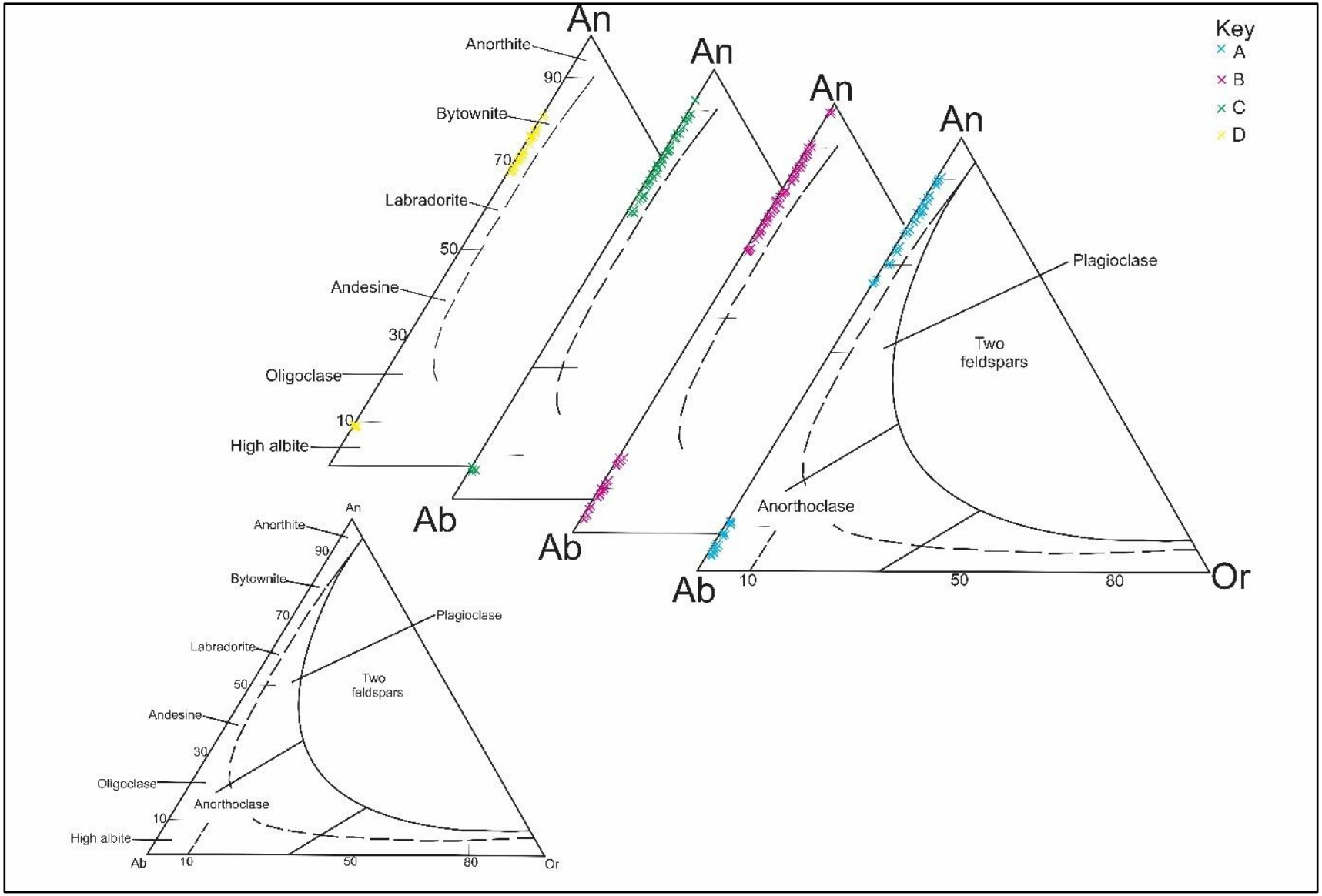

Figure 20: Ternary diagram showing intercumulus plagioclase compositions for sample cuts D-A.

The cumulus plagioclase crystals encountered in the samples have considerably higher K_2O contents than the intercumulus plagioclase crystals **(Table 5, Figures 21A and 25a)**. The $FeO_{(tot)}$ content for both cumulus and intercumulus plagioclase falls within similar ranges, with the cumulus plagioclase values becoming slightly elevated moving from sample cut D to A when compared to the intercumulus plagioclase **(Table 5, Figures 21B & 25b)**.

Table 5: Average major element compositions of cumulus and intercumulus plagioclase as determined by EMPA. Uncertainties expressed as 1 standard deviations.

Major element oxides	Cumulus plagioclase	Intercumulus plagioclase
TiO_2	0,02 ± 0,01	0,01 ± 0,01
Al_2O_3	31,45 ± 0,43	29,92 ± 4,87
Cr_2O_3	0,005 ± 0,01	0,11 ± 0,06
SiO_2	48,98 ± 0,59	51,71 ±7,73
$FeO_{(tot)}$	0,17 ± 0,03	0,14 ± 0,04
MnO	0,004 ± 0,01	0,004 ± 0,006
MgO	0,02 ± 0,01	0,02 ± 0,02
CaO	15,48 ± 0,42	13,37 ± 6,04
NiO	0,004 ± 0,01	0,01 ± 0,01
Na_2O	2,87 ± 0,23	4,20 ± 3,52
K_2O	0,15 ± 0,03	0,03 ± 0,02

The Al_2O_3 and CaO contents in the cumulus and intercumulus plagioclase crystals have a directly proportional relationship with the An% **(Figures 21C, 22A & 25c-d)**. The concentrations for Al_2O_3 and CaO in cumulus plagioclase lie roughly in the same range as in the intercumulus plagioclase. However, there are a few intercumulus plagioclase crystals that have lower An% in comparison to other plagioclase crystals and therefore, contain less CaO and Al_2O_3.

The Cr_2O_3 content varies significantly between the two plagioclase populations, with intercumulus plagioclase crystals exhibiting vastly higher concentrations than the cumulus plagioclase crystals **(Table 5, Figures 22B & 25e)**.

The SiO_2 and Na_2O in both cumulus and intercumulus plagioclase crystals exhibit an inversely proportional relationship with An% **(Table 5, Figures 22C, 23A & 25f-g)**. The SiO_2 concentrations for cumulus and intercumulus plagioclase fall roughly within a similar range, however, intercumulus plagioclase crystals with lower An% exhibit higher SiO_2 concentrations **(Figure 25f)**. The Na_2O concentrations follow the same trend as the SiO_2 **(Figure 25g)**.

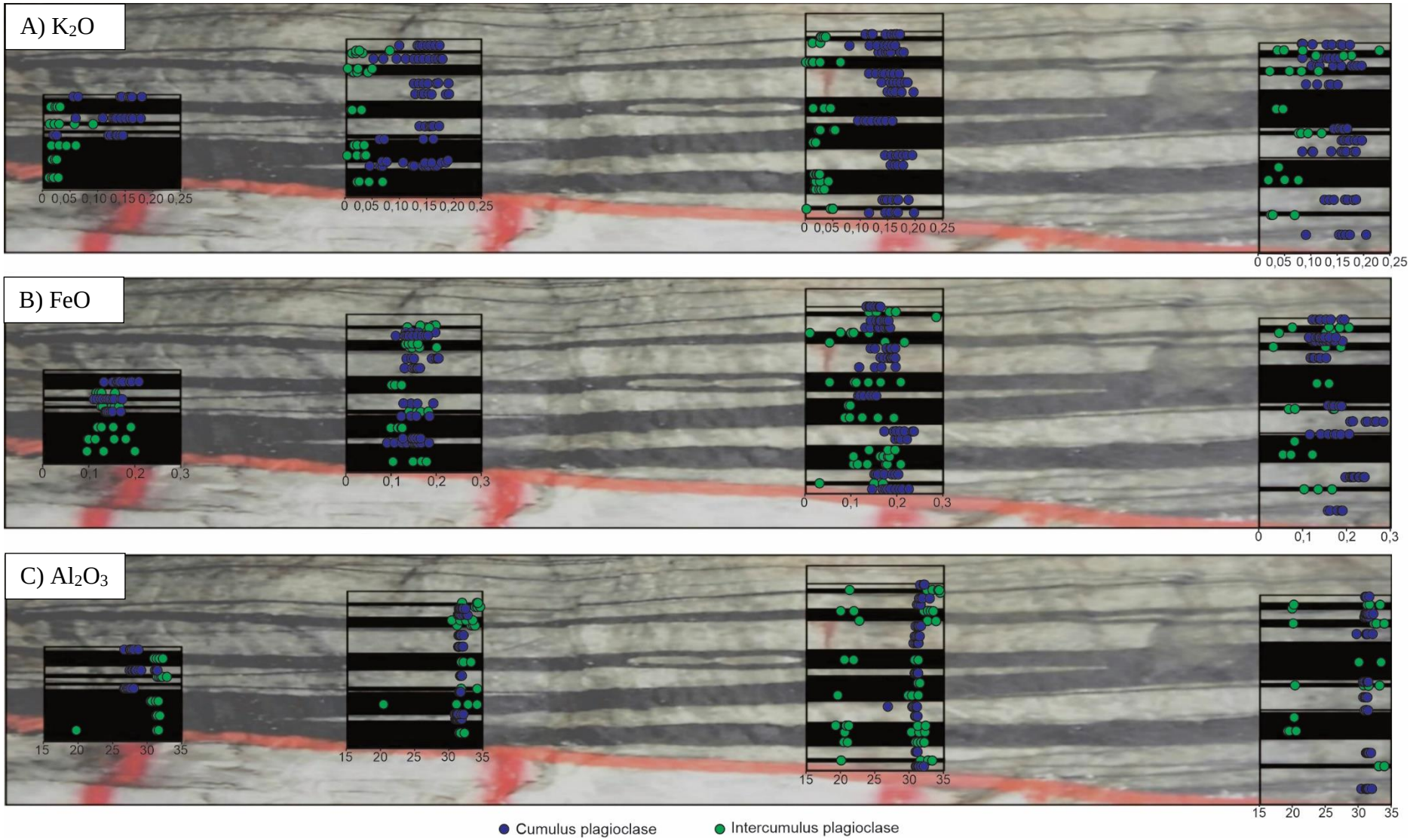

Figure 21: Plagioclase mineral chemistry depth diagrams displaying variations in the cumulus and intercumulus phases of major element oxides with depth for sample cuts D-A. A) K_2O (wt.%), B) FeO (wt.%), and C) Al_2O_3 (wt.%).

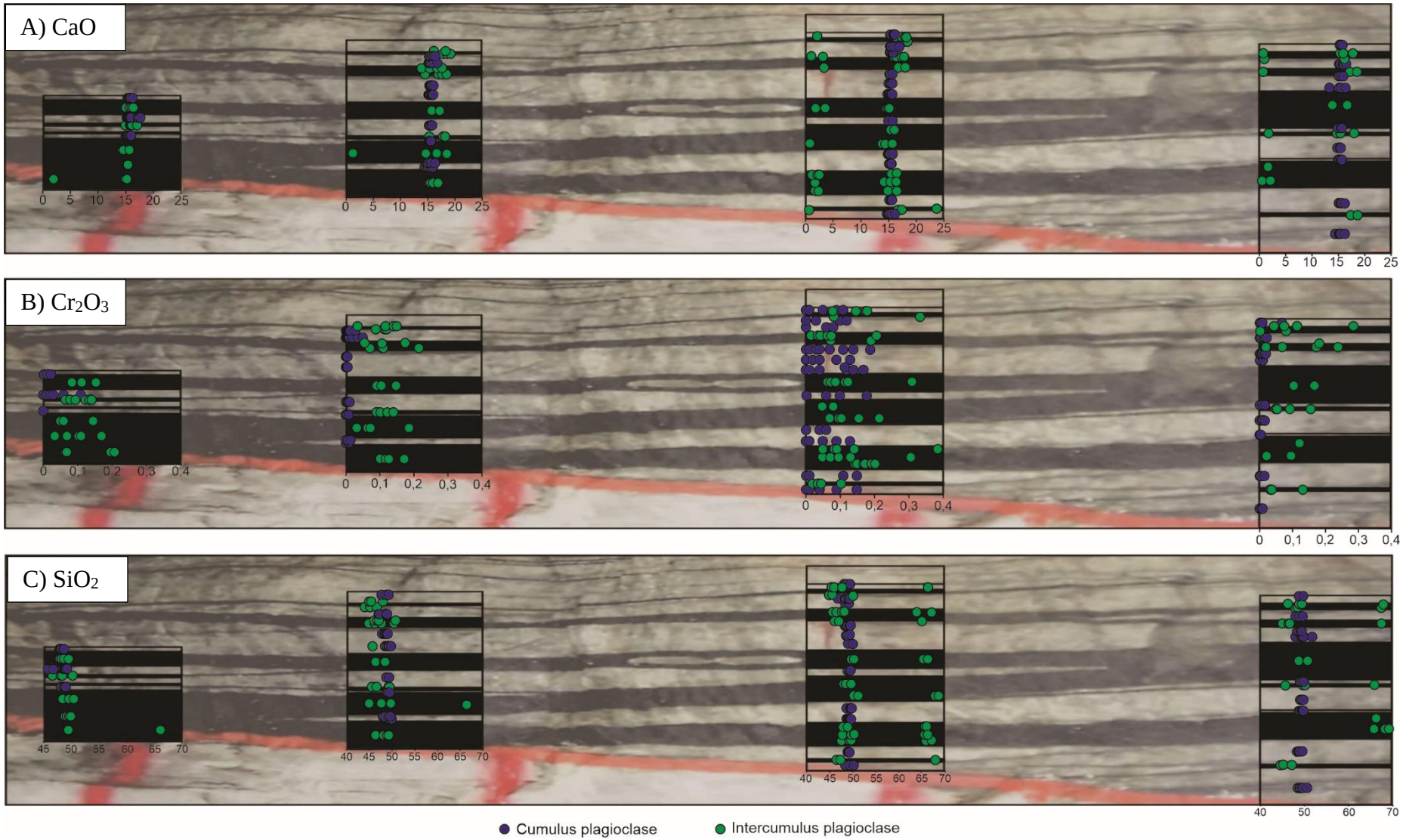

Figure 22: Plagioclase mineral chemistry depth diagrams displaying variations in the cumulus and intercumulus phases of major element oxides with depth for sample cuts D-A. A) CaO (wt.%), B) Cr_2O_3 (wt.%), and C) SiO_2 (wt.%).

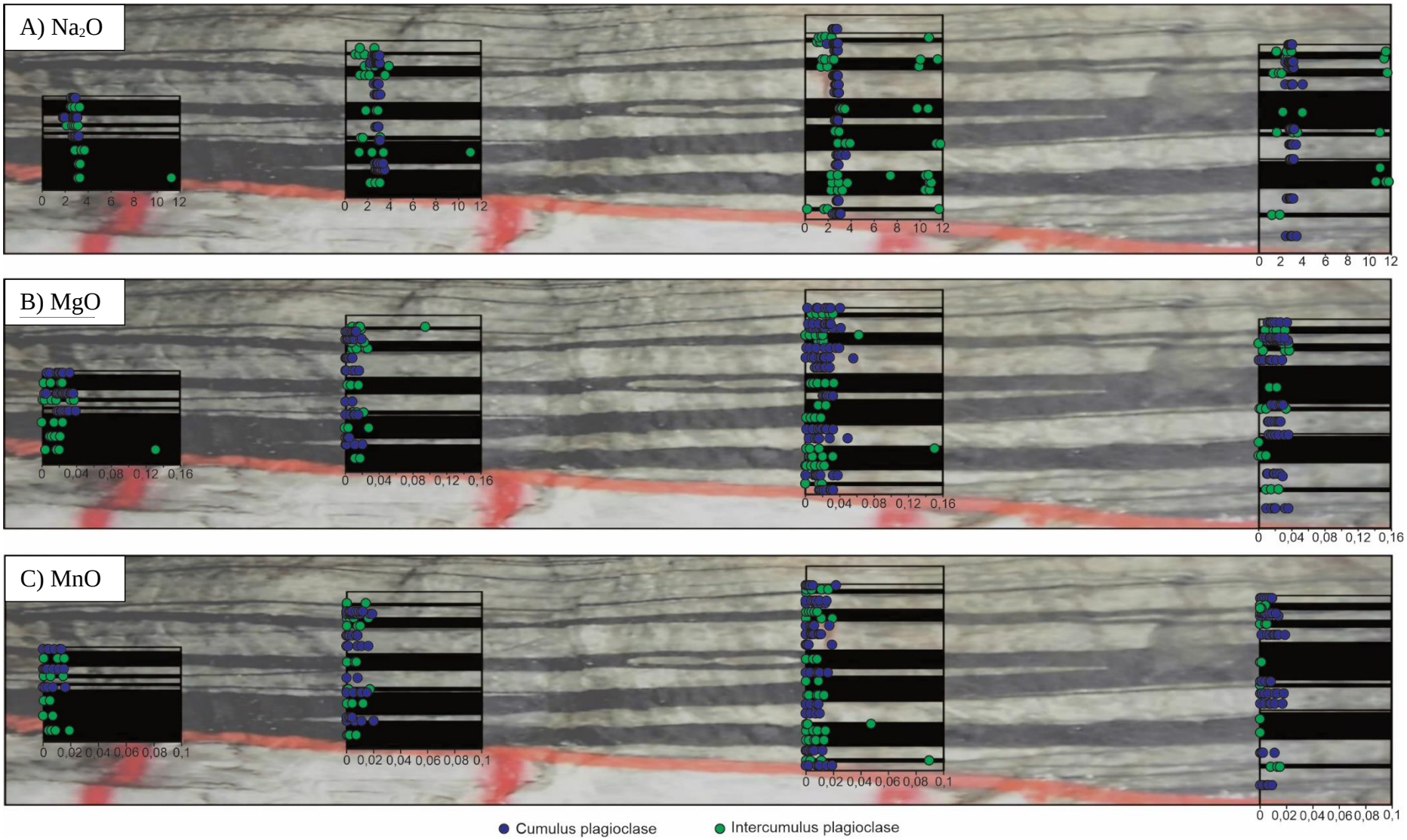

Figure 23: Plagioclase mineral chemistry depth diagrams displaying variations in the cumulus and intercumulus phases of major element oxides with depth for sample cuts D-A. A) Na_2O (wt.%), B) MgO (wt.%), and C) MnO (wt.%).

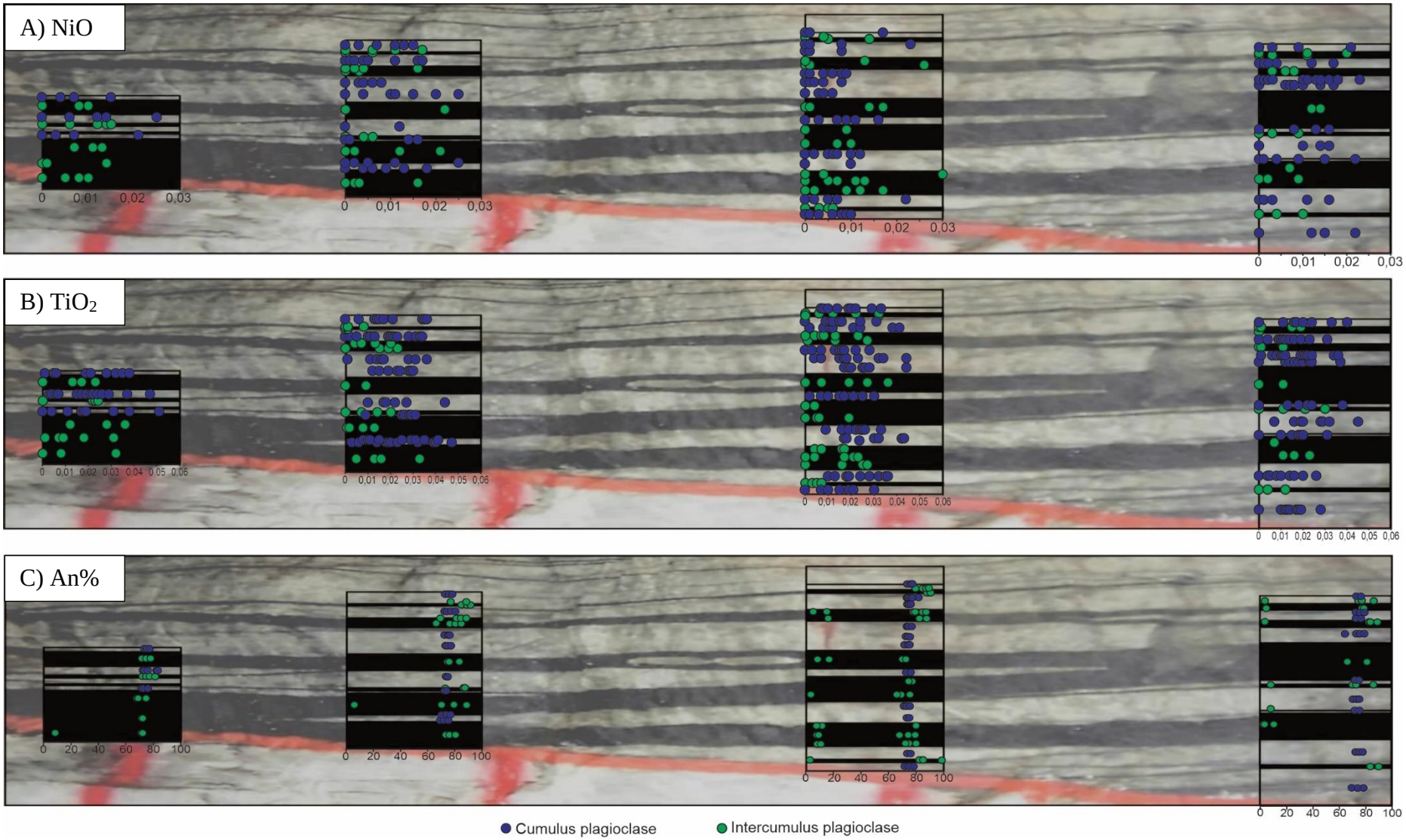

Figure 24: Plagioclase mineral chemistry depth diagrams displaying variations in the cumulus and intercumulus phases of major element oxides with depth for sample cuts D-A. A) NiO (wt.%), B) TiO_2 (wt.%), and C) An% .

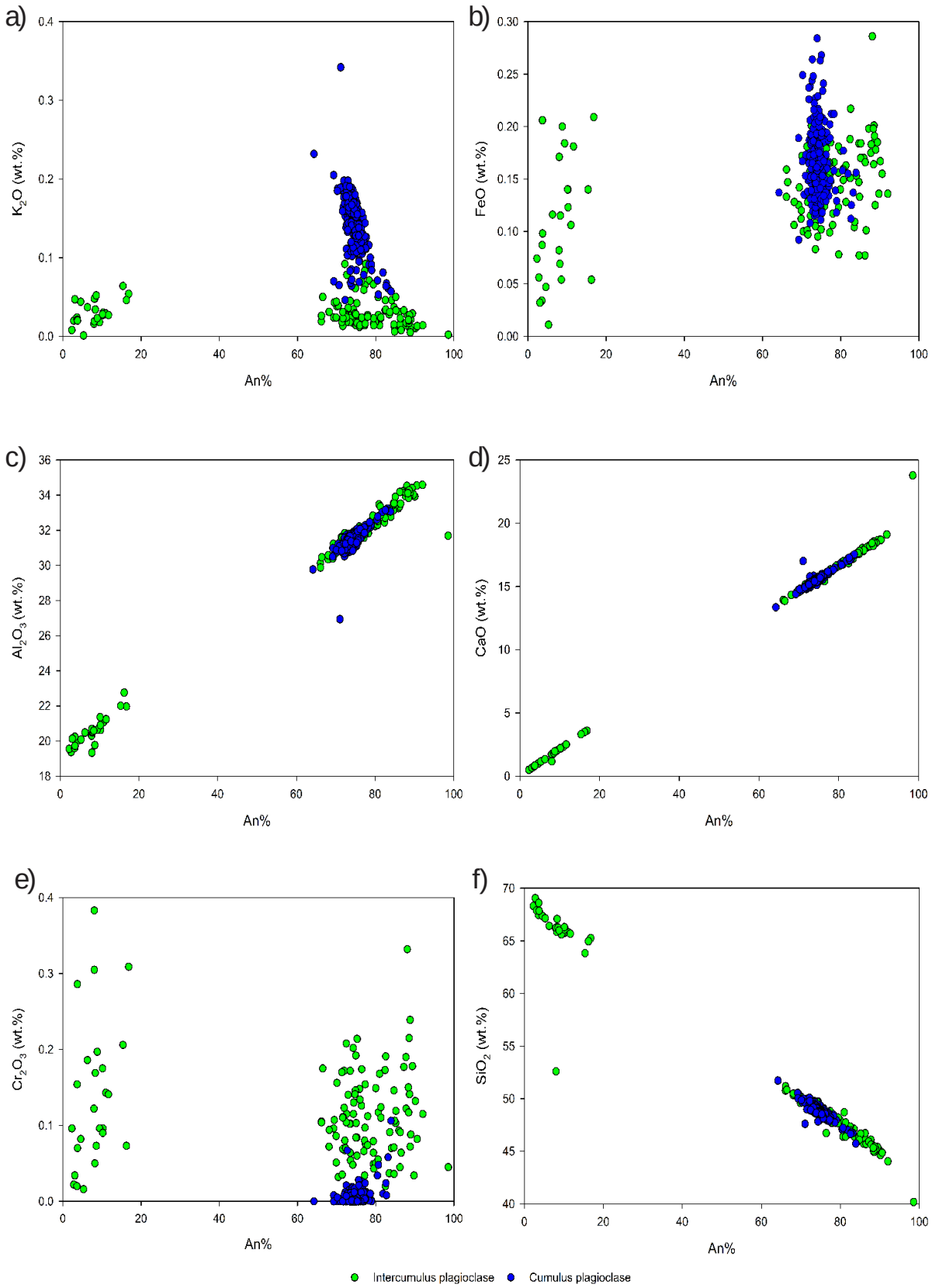

Figure 25: Binary variation diagrams for major element oxides vs. An% in both cumulus and intercumulus plagioclase crystals.

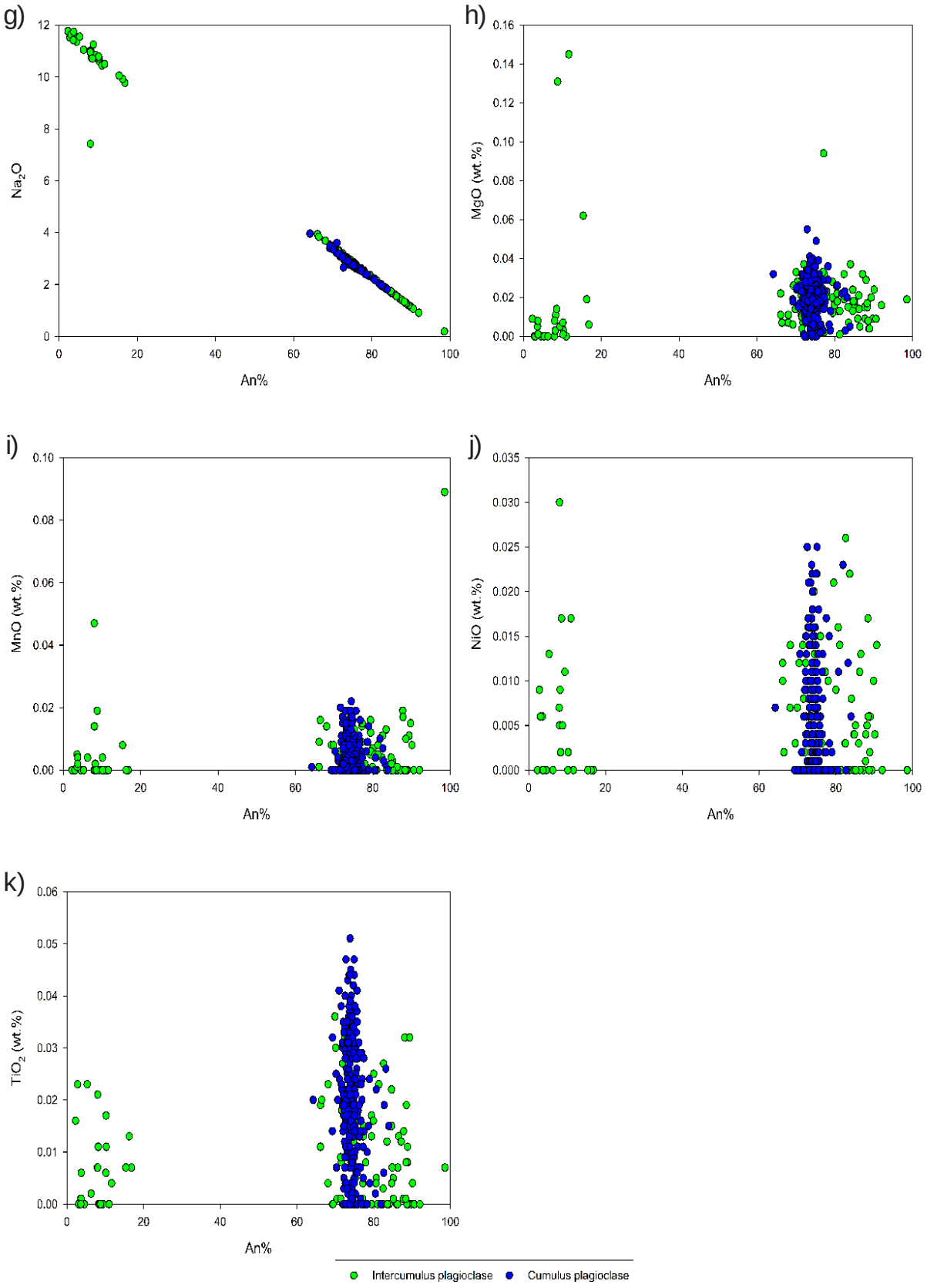

Figure 25: continued

The MgO, MnO, NiO, and TiO_2 contents all exhibit similar patterns in the two plagioclase populations. The concentration of each is similar for both cumulus and intercumulus plagioclase crystals **(Figures 23B-C. 24A-B & 25h-k)**. These major element oxides display no regular relationship with variations in An% **(Figure 24C)**.

3.4.2 Chromite

Chromite is encountered as the main component within the chromitite layers and as disseminated crystals in the anorthosite. In this section, the chromite encountered in the chromitite layers will be referred to as massive chromite, and those occurring in the anorthosite layers will be referred to as disseminated chromite. For the analysis of the chromite crystals, the following oxides were analysed: Al_2O_3, CaO, Cr_2O_3, $FeO_{(Total)}$, MgO, MnO, NiO, SiO_2, TiO_2, V_2O_3, and ZnO. The FeO analysed in the chromite minerals represents the total FeO content ($FeO_{(tot)}$). The data are presented in depth and **(Figures 26 – 29)** binary variation diagrams **(Figure 30)** to illustrate the changes in major element oxides with Mg# and how the major element oxides differ with depth in massive and disseminated chromite crystals for each sample cut. The microprobe data for all the analysed chromite crystals are presented in **Appendix C: Tables C1 and C2**. The magnesium number was calculated using Mg# = molar MgO / ($FeO_{(tot)}$ + MgO).

The analysed chromite crystals reveal that the $FeO_{(tot)}$ concentrations in disseminated chromite crystals are typically higher than that in massive chromite crystals **(Figures 26A, 30a & Table 6)**. The Al_2O_3 concentration in the massive and disseminated chromite is directly proportional to the Mg# **(Figure 30b)**. Figure 26B and Table 6 show that the Al_2O_3 content of the massive chromite is higher than in disseminated chromite.

The Cr_2O_3 content of the disseminated chromite ranges from 31,21 – 50,47%, and that of the massive chromite lies between 39,20 – 47,15%. Although there is a higher degree of variation in the disseminated chromite, the average values for the Cr_2O_3 content in both the chromite types fall within a similar range **(Figures 26C & 30c)**.

The MgO concentration in massive chromite crystals is much higher than in disseminated chromite crystals **(Figures 27A & 30d)**; this can also be observed from the average values in Table 6. Although MnO occurs in minor concentrations, disseminated chromite crystals

contain more MnO than massive chromite crystals **(Figures 27B & 30e)**. The CaO concentration is mostly similar when observing the binary variation diagram **(Figure 30f)** with a few of the disseminated chromite crystals exhibiting higher concentrations than the other crystals.

The concentration of TiO_2, V_2O_3, and ZnO are low, but the variation in the concentration between the disseminated and massive chromite is noteworthy as the disseminated chromite tend to contain higher concentrations than the massive chromite **(Figures 28A-C & 30g-i)**. NiO and SiO_2 content in both massive and disseminated chromite is mostly similar **(Figures 29 A-B, 30j & k)** and this can also be observed in the average values in **Table 6**.

Table 6: Average major element compositions and Mg# of massive and disseminated chromite as determined by EMPA. The uncertainties are expressed as 1 standard deviations.

Major element oxides and Mg#	In Chromitite Layers	In Anorthosite Layers
Al_2O_3	14,46 ± 2,93	8,61 ± 1,82
CaO	0,027 ± 0,055	0,01 ± 0,02
Cr_2O_3	45,36 ± 1,34	44,73 ± 4,51
$FeO_{(tot)}$	30,06 ± 4,27	39,03 ± 5,99
MgO	7,58 ± 2,04	3,74 ± 1,45
MnO	0,27 ± 0,05	0,36 ± 0,07
NiO	0,14 ± 0,02	0,15 ± 0,03
SiO_2	0,01 ± 0,01	0,02 ± 0,05
TiO_2	1,06 ± 0,19	1,60 ± 0,66
V_2O_3	0,50 ± 0,05	0,57 ± 0,06
ZnO	0,11 ± 0,02	0,13 ± 0,02
Mg#	0,34 ± 0,05	0,16 ± 0,07

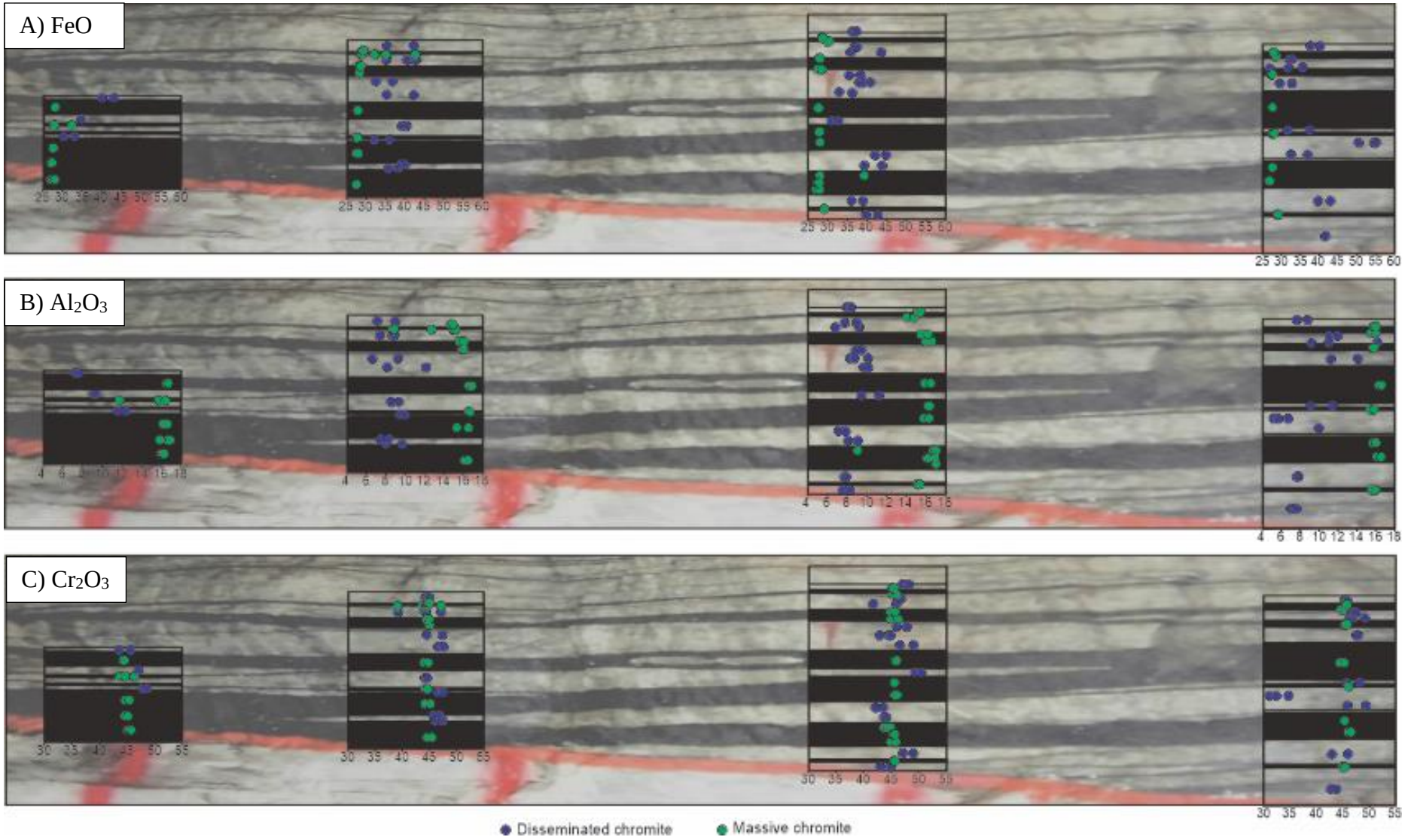

Figure 26: Chromite mineral chemistry depth diagrams displaying variations in the cumulus and intercumulus phases of major element oxides with depth for sample cuts D-A. A) $FeO_{(tot)}$ (wt.%), B) Al_2O_3 (wt.%), and C) Cr_2O_3 (wt.%).

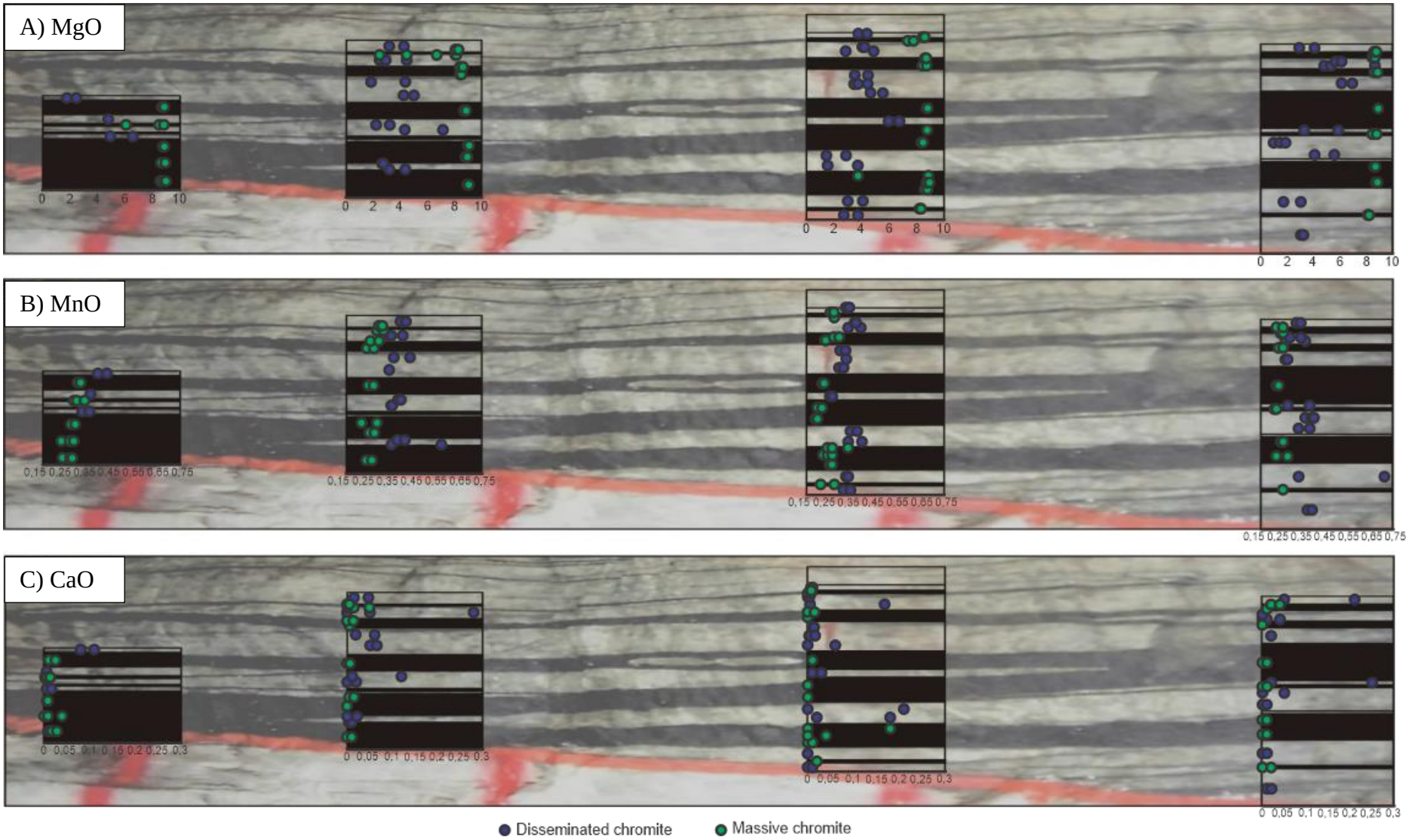

Figure 27: Chromite mineral chemistry depth diagrams displaying variations in the disseminated and massive chromite phases of major element oxides with depth for sample cuts D-A. A) MgO (wt.%), B) MnO (wt.%), and C) CaO(wt.%).

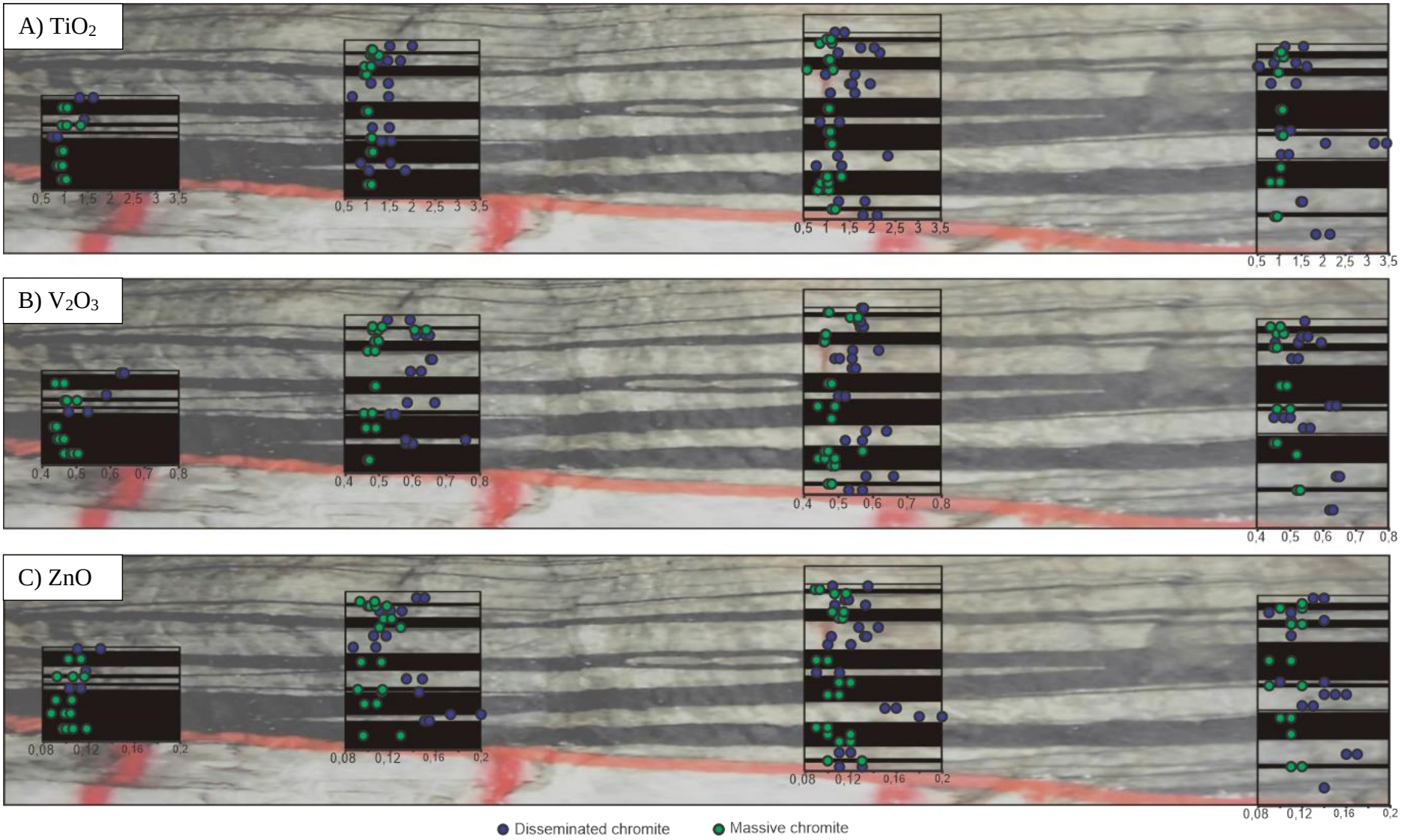

Figure 28: Chromite mineral chemistry depth diagrams displaying variations in the disseminated and massive chromite phases of major element oxides with depth for sample cuts D-A. A) TiO_2 (wt.%), B) V_2O_3 (wt.%), and C) ZnO (wt.%).

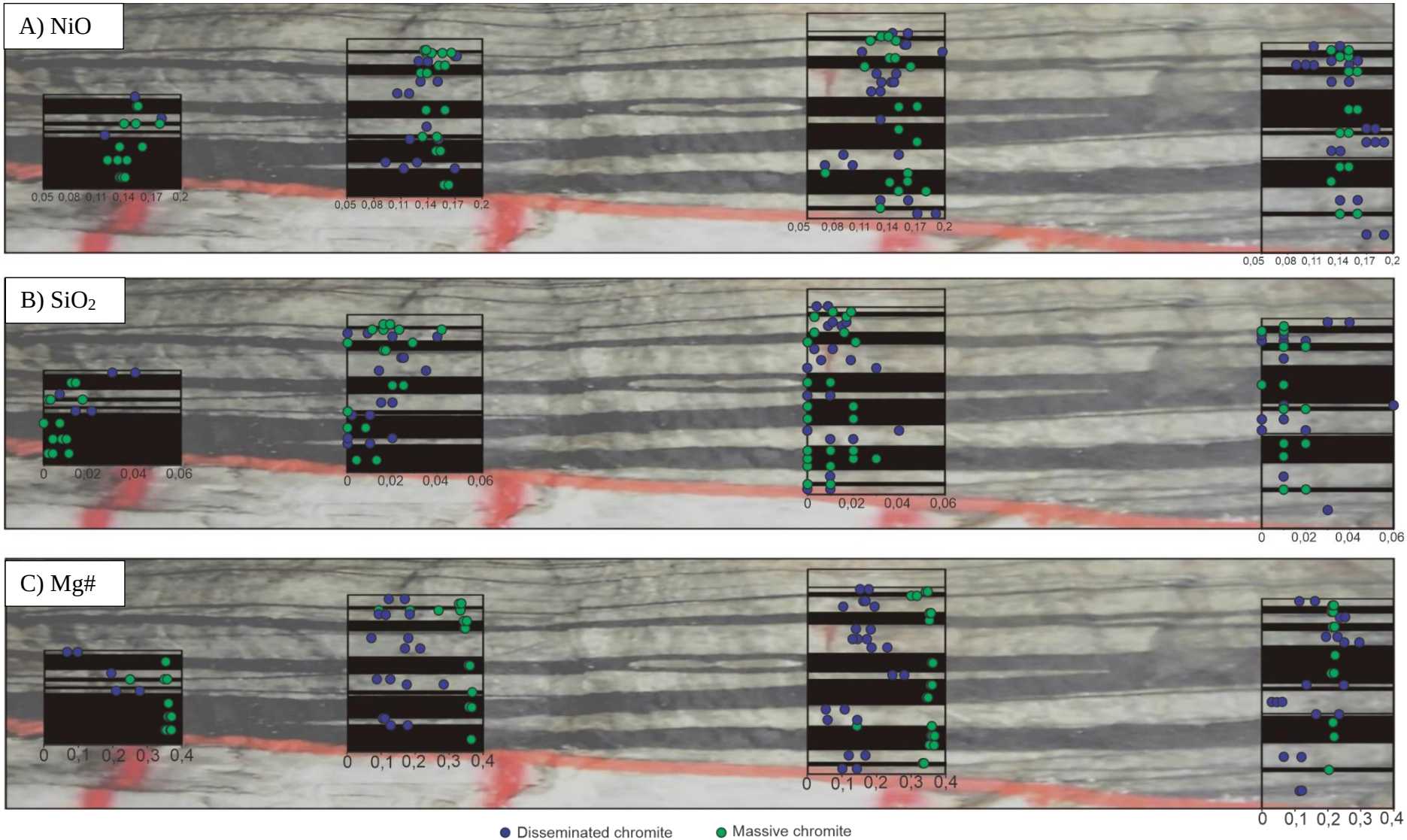

Figure 29: Chromite mineral chemistry depth diagrams displaying variations in the disseminated and massive chromite phases of major element oxides and Mg# with depth for sample cuts D-A. A) NiO (wt.%), B) SiO_2 (wt.%), and C) Mg#

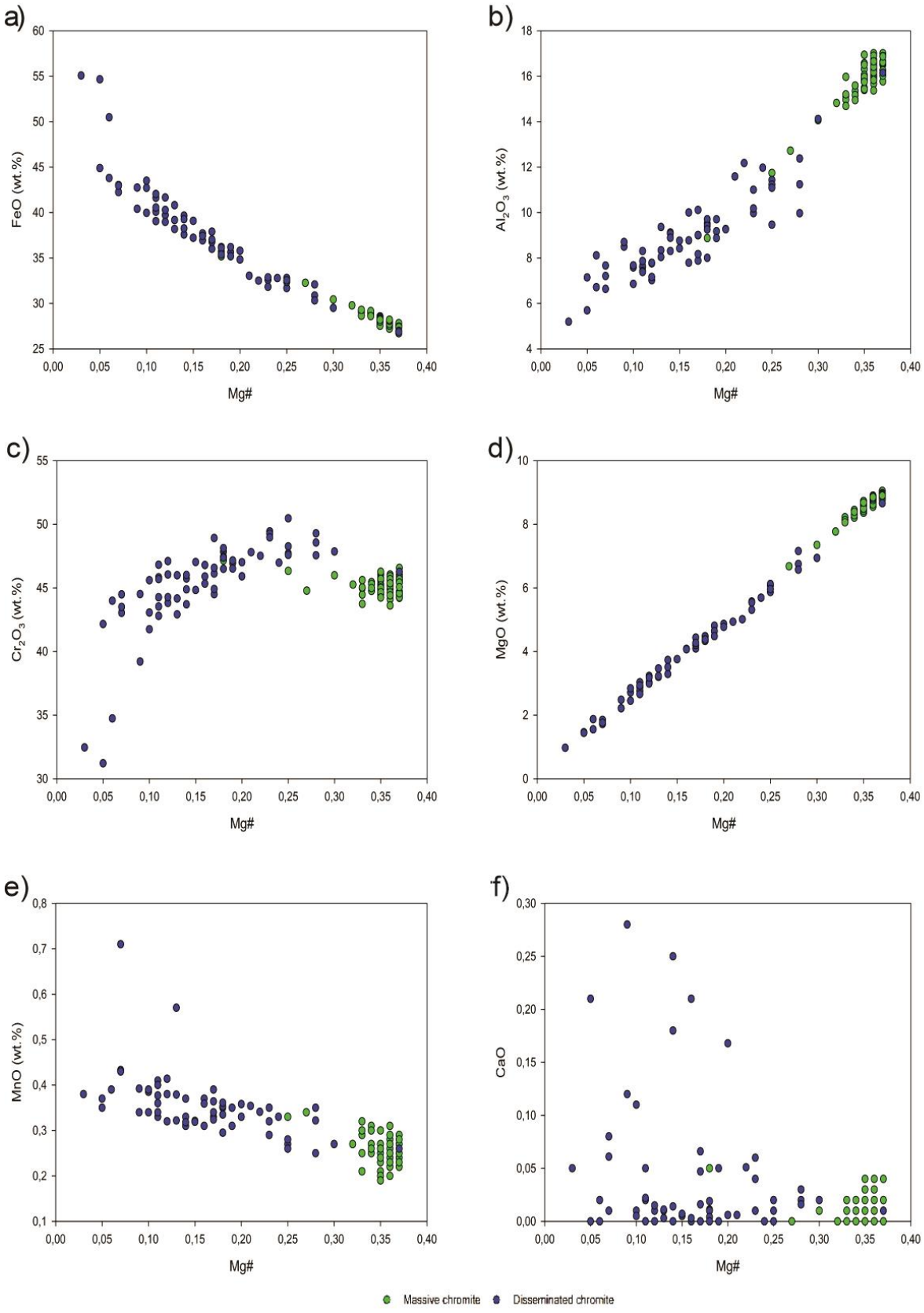

Figure 30: Major element oxides vs Mg# for massive and disseminated chromite crystals.

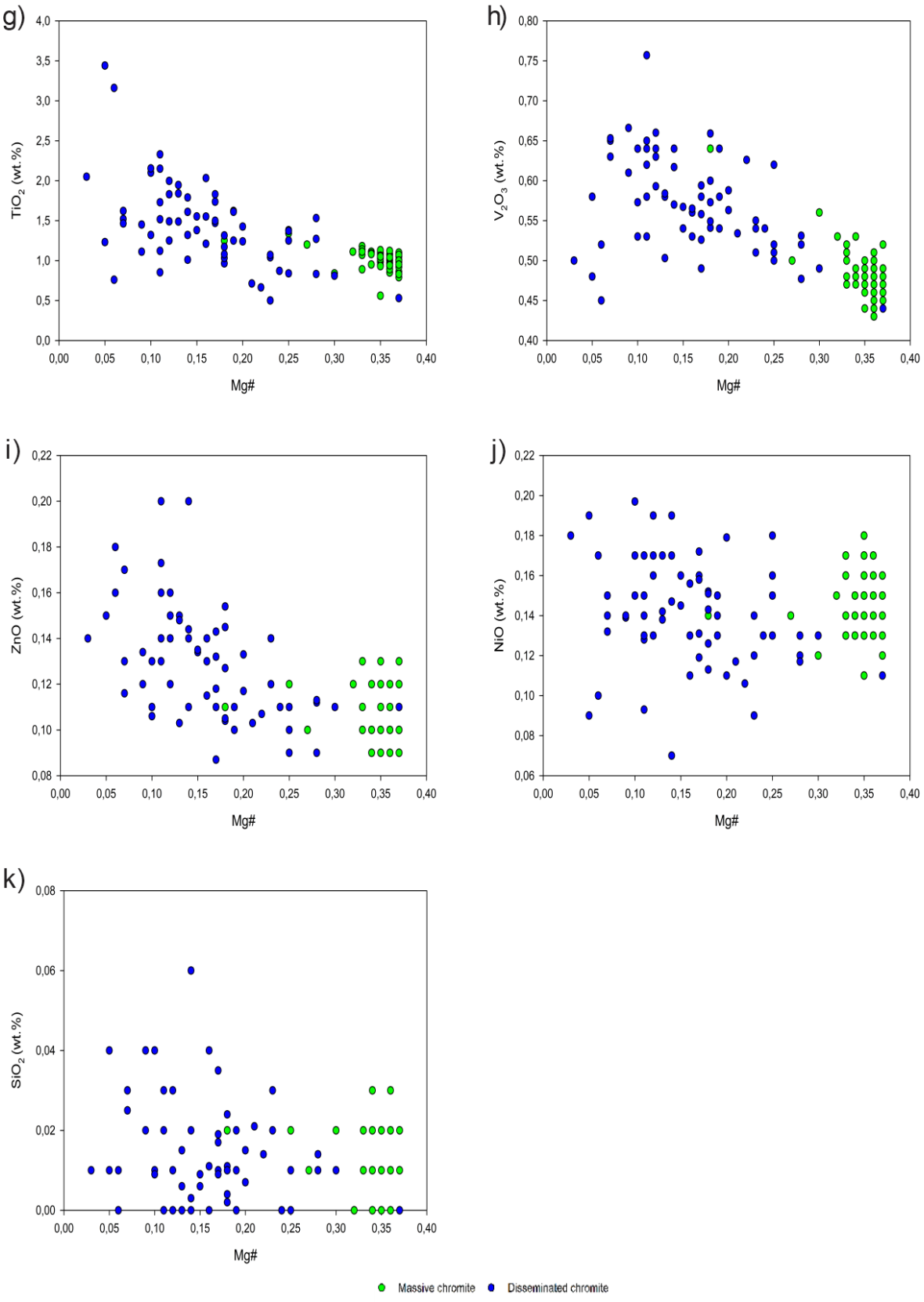

Figure 30: Continued

3.5 Plagioclase Sr-isotopic composition

For the isotopic study, the same cumulus and intercumulus plagioclase crystals analysed for mineral chemistry were analysed for Sr isotope ratios. The initial $^{87}Sr/^{86}Sr$ values were plotted in depth profiles **(Figures 31 – 35)** along with their 2 sigma error values to show how the initial $^{87}Sr/^{86}Sr$ ratios vary laterally and in depth along the study area. The data obtained from the analyses and the calculated initial $^{87}Sr/^{86}Sr$ ratios are available in Appendix D.

The initial $^{87}Sr/^{86}Sr$ (Sr_i) isotopic ratios for the cumulus plagioclase crystals range from 0,7022 to 0,7075, with an average value of 0,7062 ± 0,0005. For intercumulus plagioclase crystals initial $^{87}Sr/^{86}Sr$ (Sr_i) values lie between 0,7006 and 0,7097, with an average value of 0,7066 ± 0,0010. The average in-situ Sr_i values for the cumulus (anorthosite layers) and intercumulus (chromitite layers) plagioclase crystals for each thin section are presented in Table 7. The initial $^{87}Sr/^{86}Sr$ values appear to be to some extent greater in the intercumulus plagioclase than in the cumulus plagioclase with depth in sample cuts D – A **(Figures 31-35)**.

In sample cut D **(Figure 32)** the initial $^{87}Sr/^{86}Sr$ ratios range from 0,7039 – 0,7066 in the anorthosite layers (cumulus plagioclase) and from 0,7058 – 0,7069 in the chromitite layers, with averages of 0,7062 ± 0,0007 and 0,7063 ± 0,0003 respectively. The most noticeable difference which has been observed throughout the samples is that the second anorthosite layer from the top has ratios that are significantly lower than any of the other layers. Although the majority of the differences observed are almost negligible, it is also noteworthy to mention that the chromitite layers typically have greater initial $^{87}Sr/^{86}Sr$ ratios than the anorthosite layers.

The initial $^{87}Sr/^{86}Sr$ ratios in sample cut C **(Figure 33)** are between 0,7038 – 0,7070 with an average of 0,7062 ± 0,0004 in the anorthosite layers and between 0,7054 – 0,7088 with an average of 0,7065 ± 0,0006 in the chromitite layers. The chromitite layers in sample cut C mostly have greater values for initial $^{87}Sr/^{86}Sr$ ratios than in the anorthosite layers. It is also incumbent to note that the differences in the ratios moving from chromitite to anorthosite layers are more pronounced than in sample cut D.

In sample cut B **(Figure 34)** the chromitite layers have initial $^{87}Sr/^{86}Sr$ ratios ranging from 0,7006 to 0,7088 with an average of 0,7065 ± 0,0011. In the anorthosite layer the ratios range from 0,7054 to 0,7075, with an average of 0,07063 ± 0,0003. In almost all of the chromitite

layers the initial $^{87}Sr/^{86}Sr$ ratios tend to be much greater than in the anorthosite layers. The third chromitite layers from the top does, however, display an extremely low value of 0,7006, which is the lowest value observed in all the sample cuts.

In sample cut A the **(Figure 35)** chromitite and anorthosite layers have initial $^{87}Sr/^{86}Sr$ ratios from 0,7022 – 0,7073 and 0,7055 – 0,7097, with averages of 0,7062 ± 0,0007 and 0,7073 ± 0,0012 respectively. The initial $^{87}Sr/^{86}Sr$ ratios are visibly much higher in the chromitite layers than in the anorthosite layers, similar to the trends seen in the other sample cuts. The two lowermost chromitite layers on sample cut A also have the greatest values in all the sample cuts.

Table 7: Average in-situ ratios for $^{87}Sr/^{86}Sr$, $^{87}Rb/^{86}Sr$ and initial $^{87}Sr/^{86}Sr$ with the propagated errors for cumulus and intercumulus plagioclase. The 2SE errors on the initial isotope ratios include errors propagated from measured isotope ratios.

Cumulus plagioclase					Intercumulus plagioclase				
Comment	$^{87}Sr/^{86}Sr$	$^{87}Rb/^{86}Sr$	initial $^{87}Sr/^{86}Sr$	2SE	Comment	$^{87}Sr/^{86}Sr$	$^{87}Rb/^{86}Sr$	initial $^{87}Sr/^{86}Sr$	2SE
A1	0,7065	0,0022	0,7064	0,0001	A1	0,7084	0,3239	0,7074	0,0011
A2	0,7064	0,0077	0,7062	0,0003	A2	0,7094	0,0142	0,7089	0,0005
A3	0,7064	0,0098	0,7061	0,0001	A3	0,7084	0,0028	0,7083	0,0001
A4	0,7065	0,0109	0,7062	0,0002	A5	0,7073	0,0281	0,7065	0,0001
A5	0,7063	0,0103	0,7060	0,0001	A6	0,7058	0,0011	0,7057	0,0004
A6	0,7064	0,0274	0,7056	0,0002	A7	0,7068	0,0093	0,7065	0,0003
A7	0,7066	0,0016	0,7065	0,0002	A8	0,7069	0,0149	0,7065	0,0004
A8	0,7068	0,0023	0,7068	0,0004	A9	0,7071	0,0085	0,7069	0,0003
A9	0,7064	0,0017	0,7064	0,0002	B1	0,7076	0,0166	0,7072	0,0006
B1	0,7066	0,0018	0,7065	0,0001	B2	0,7079	0,0185	0,7073	0,0002
B2	0,7064	0,0055	0,7063	0,0002	B3	0,7069	0,0137	0,7065	0,0002
B4	0,7062	0,0032	0,7061	0,0002	B4	0,7080	0,0148	0,7076	0,0001
B5	0,7065	0,0074	0,7063	0,0001	B5	0,7076	0,0325	0,7067	0,0002
B6	0,7063	0,0032	0,7062	0,0002	B6	0,7065	0,0083	0,7062	0,0001
B7	0,7063	0,0017	0,7063	0,0002	B7	0,7063	0,0283	0,7055	0,0002
B8	0,7064	0,0021	0,7063	0,0002	B9	0,7094	0,0865	0,7068	0,0002
B9	0,7065	0,0024	0,7064	0,0002	B10	0,7065	0,0048	0,7064	0,0126
B10	0,7063	0,0040	0,7062	0,0004	B11	0,7078	0,0209	0,7072	0,0002
B11	0,7065	0,0058	0,7063	0,0002	B12	0,7067	0,0130	0,7063	0,0002
B12	0,7064	0,0015	0,7063	0,0002	C1	0,7064	0,0059	0,7062	0,0002
C1	0,7062	0,0020	0,7061	0,0002	C2	0,7069	0,0182	0,7064	0,0003
C2	0,7064	0,0026	0,7063	0,0002	C3	0,7064	0,0020	0,7063	0,0002
C3	0,7062	0,0081	0,7059	0,0002	C4	0,7067	0,0055	0,7066	0,0103
C4	0,7061	0,0009	0,7061	0,0002	C5	0,7067	0,0029	0,7066	0,0056
C5	0,7065	0,0023	0,7064	0,0002	C6	0,7065	0,0056	0,7064	0,0002

C6	0,7063	0,0012	0,7063	0,0002	C7	0,7065	0,0082	0,7063	0,0001
C7	0,7062	0,0028	0,7061	0,0002	C8	0,7074	0,0036	0,7073	0,0001
C8	0,7064	0,0044	0,7063	0,0002	D1	0,7065	0,0016	0,7064	0,0001
D3	0,7063	0,0014	0,7062	0,0002	D2	0,7063	0,0008	0,7063	0,0001
D4	0,7062	0,0089	0,7060	0,0002	D3	0,7064	0,0008	0,7064	0,0001
D5	0,7064	0,0018	0,7063	0,0002	D4	0,7062	0,0037	0,7061	0,0001
					D5	0,7064	0,0015	0,7064	0,0002

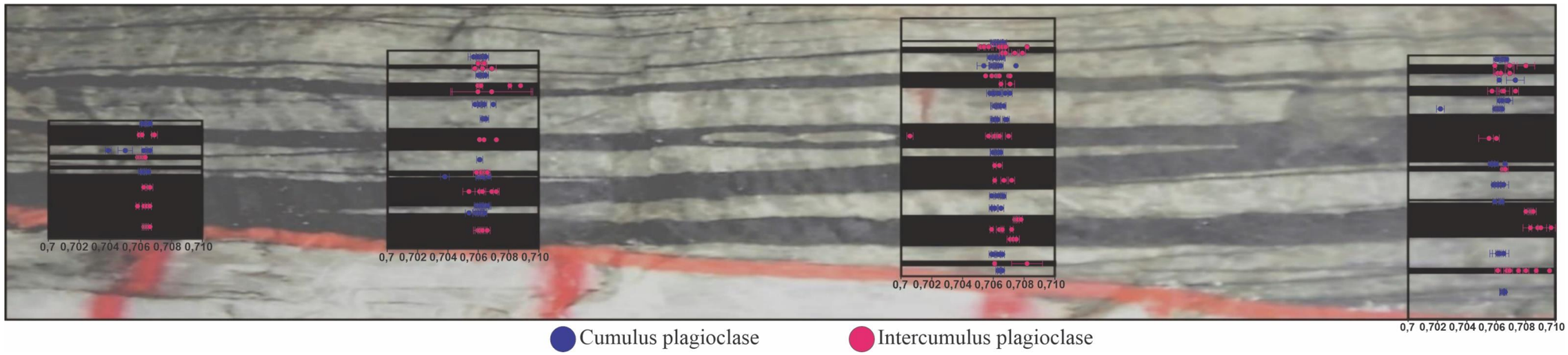

Figure 31: Initial $^{87}Sr/^{86}Sr$ values for cumulus and intercumulus plagioclase crystals analysed for each sample cut (D-A) along with error bars.

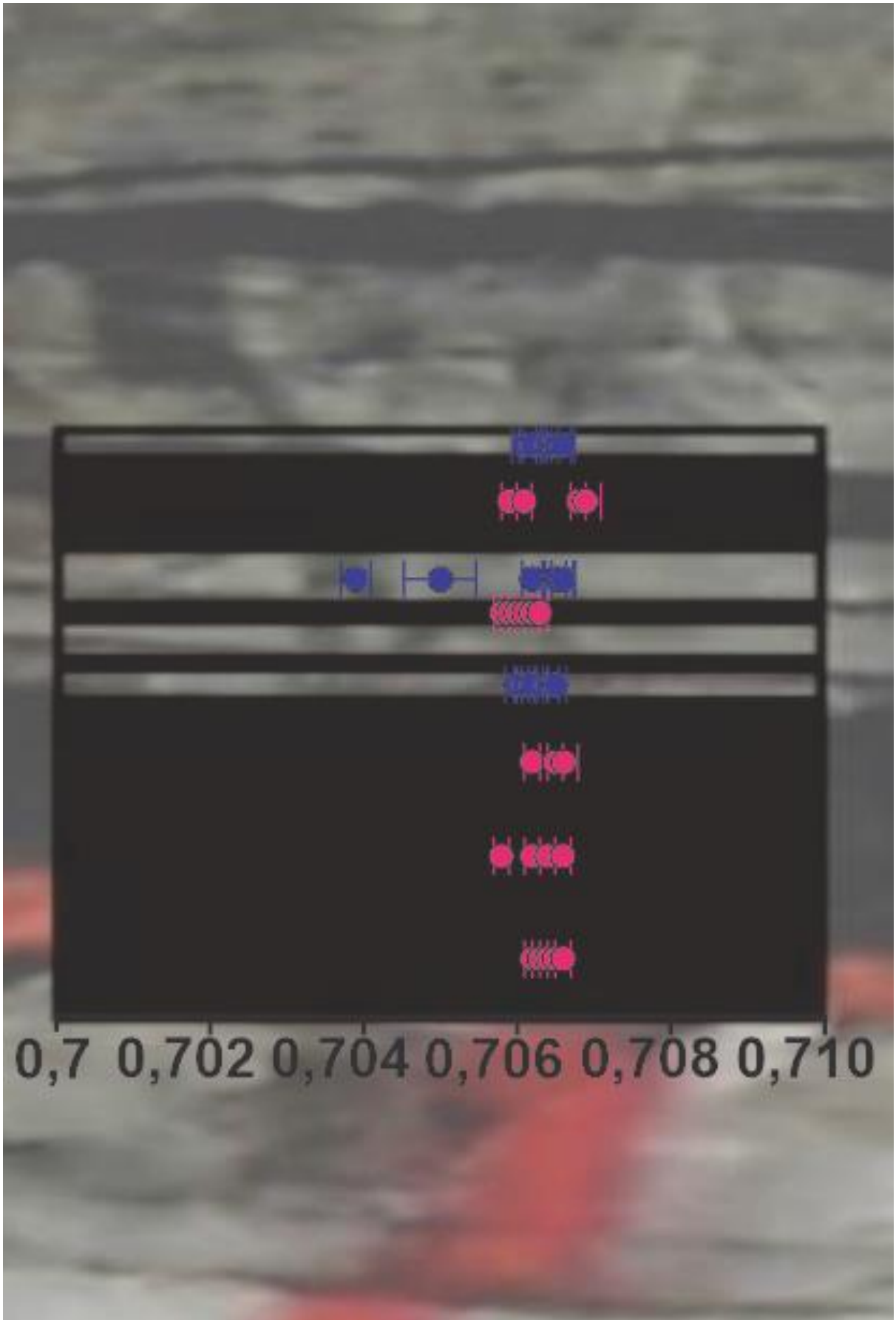

Figure 32: Initial $^{87}Sr/^{86}Sr$ values for cumulus and intercumulus plagioclase crystals analysed for sample cut D along with error bars.

Figure 33: Initial $^{87}Sr/^{86}Sr$ values for cumulus and intercumulus plagioclase crystals analysed for sample cut C along with error bars.

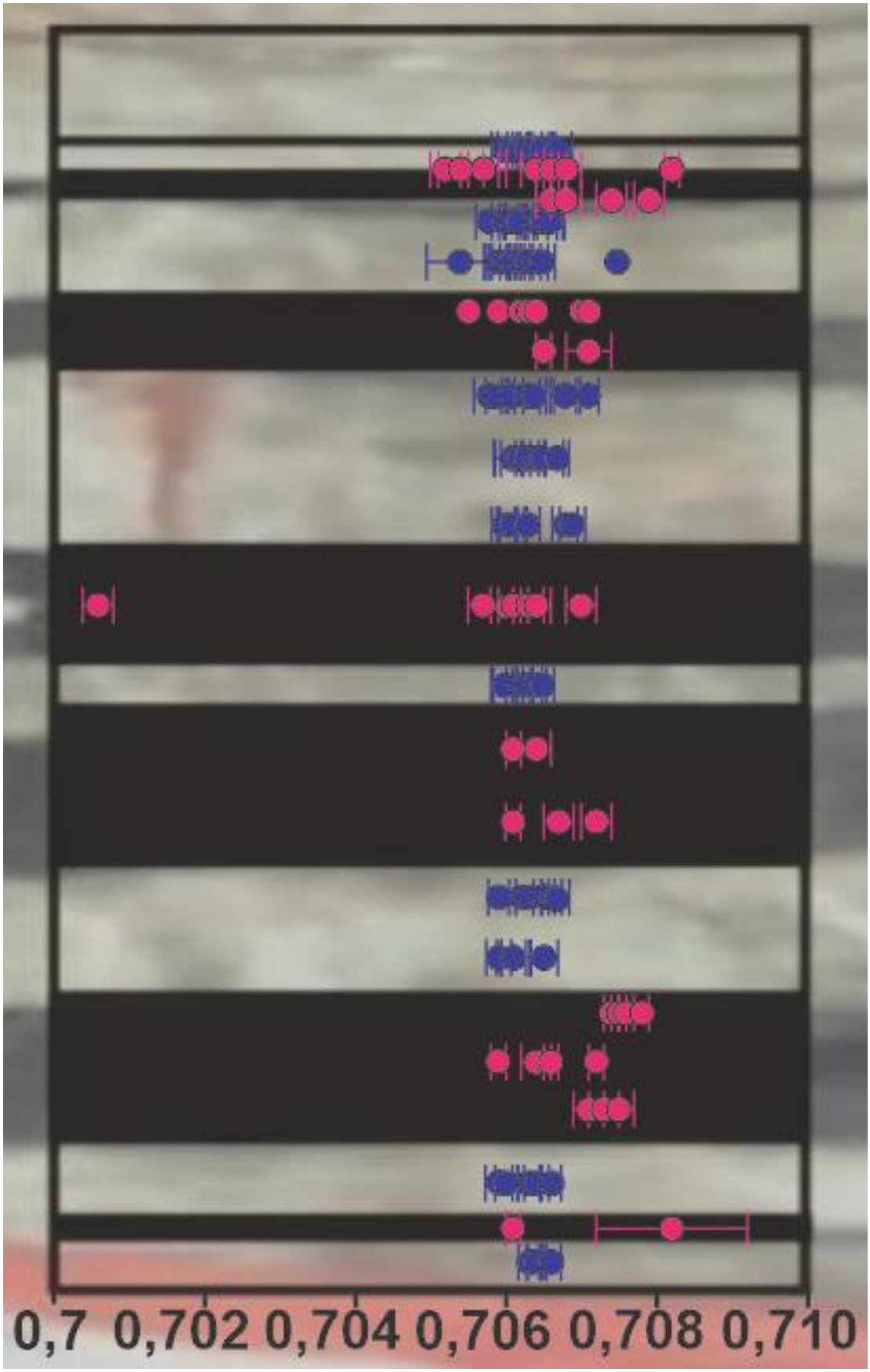

Figure 34: Initial $^{87}Sr/^{86}Sr$ values for cumulus and intercumulus plagioclase crystals analysed for sample cut B along with error bars.

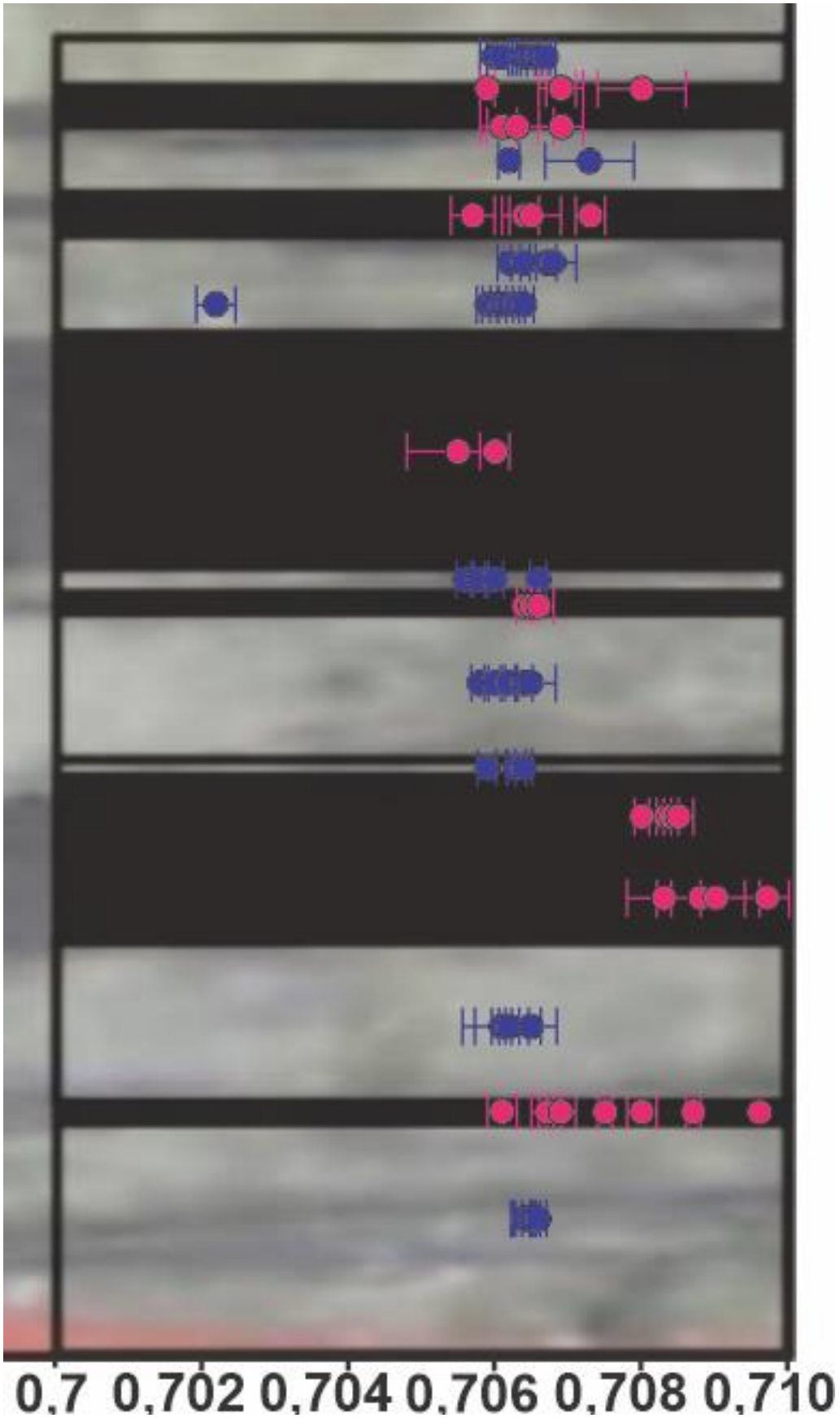

Figure 35: Initial $^{87}Sr/^{86}Sr$ values for cumulus and intercumulus plagioclase crystals analysed for sample cut A along with error bars.

4 Discussion

4.1 Field observations

In this section, all the observations made in the study area are discussed to help understand the morphology of the chromitite bifurcations in more detail by proposing possible explanations for the different structures and deformational features observed.

The study area is mainly composed of alternating layers of anorthosite and chromitite rock units, which are typical of the Upper Critical Zone of the Bushveld Complex. The difference, however, is that this area is riddled with numerous chromitite bifurcations. Features such as anorthosite inclusions within chromitite layers **(Figure 14)**, pothole-like chromitite structures **(Figure 15)**, faulting **(Figures 10g and 15)**, and plastically deformed chromitite layers **(Figure 10h)** were also observed.

The anorthosite inclusions were encountered in various sizes and occurred in circular or elongated shapes. In their study, Pebane and Latypov (2017) encountered similar anorthosite inclusions and came up with two interpretations on how they may have come to be. The first interpretation was that the elongated inclusions, which typically terminate into a wispy tail, were formed in-situ, and are related to the lateral termination of the anorthosite layers. Furthermore, they observed that the inclusions have either an irregular **(Figure 14a)** or planar **(Figure 14c)** contact with the host chromitite layer. The second interpretation was that the more rounded inclusions were transported from another anorthositic source as opposed to being formed in-situ.

Cawthorn (2003) claim that anorthosite lenses are crucial in forming bifurcations. The inclusions were formed when a thin chromitite layer was emplaced above the anorthosite footwall, followed by the formation of an incomplete anorthosite layer above the thin chromitite layer which formed growth bulges and discontinuous silicate patches. Another thin chromitite layer was emplaced above these anorthosite bulges and patches, forming inclusions and bifurcations through a repetition of the above processes. Nex (2004) proposed that the lenses/inclusions could have been created by the liquefaction of an anorthosite overlain by a chromitite layer. The anorthosite extruded and formed lenses above the chromitite layer, which were covered by another layer of chromitite. Cawthorn (2015) added to the above and

concluded that discontinuous anorthosite lenses were formed due to horizontal flowing plagioclase suspensions and the continuous chromitite layers accumulated due to seismic activity. The current study area, unlike the Dwars River Locality (DRL), has a lack of pronounced anorthosite lenses. This could imply that the lenses are not as crucial in forming bifurcations, or the processes involved in forming chromitite bifurcations, although comparable, might not necessarily be the same in all areas across the Critical Zone.

Mukherjee *et al.* (2017) provided a possible explanation of how the pothole-like structure could have formed. Their study focused on the emplacement mechanisms of the UG1 chromitite. They suggested that it was essential to understand the various features observed in the UG1, including potholes, before an interpretation of the emplacement of the UG1 could be made. They investigated an area from No.11 Shaft at Impala Platinum Limited, where potholes cut into the underlying layers. They hypothesised that the UG1 chromitite intruded into the footwall anorthosite from a magma chamber containing a superheated melt that upon cooling became saturated in chromite. The melt eroded the anorthosite footwall, which led to the formation of a pothole. The pothole-like structure in the study area could have also formed through thermo-chemical erosion. Mukherjee *et al.* (2017) further proposed that the continued erosion of the anorthosite and the accumulation of the melt inside the pothole led to the fracturing of the anorthosite footwall. The fractures were invaded by the melt and crystallised to form sills; therefore, this supports the intrusive model as the prevalent mechanism in the formation of chromitite bifurcations.

The displacement of the strata in **Figure 10g** and **h** provide clear evidence of post-depositional deformation. The layers were displaced during faulting (brittle deformation), which affected both the anorthosite and chromitite layers. Both normal and reverse fault movement can be observed in the study area. The faults are overlain and underlain by undisturbed layers. The sizes and positions of the faults indicate that the pressure/stresses involved were most probably localised (Nicholson, 2020).

4.2 Petrography

The petrography of the anorthosite appears to be consistent throughout the study area. The abundant mineral phase is fine to medium-crystalline (0.2 – 2 mm) cumulus plagioclase crystals followed by clinopyroxene, phlogopite, orthopyroxene, and chromite. The cumulus

plagioclase crystals contain several features that may reveal the conditions under which the anorthosite was formed, along with the events that took place subsequent to anorthosite formation. Firstly, the plagioclase crystals display lamellar twining along with wedge-shaped and bent deformation twinning, which are indicators of dislocation creep (Barnes & Maier, 2002; Nicholson, 2020). Another feature observed is the presence of cracks in some of the plagioclase crystals, along with undulatory extinction across the majority of the plagioclase crystals. According to Barnes & Maier (2002), these may be the results of brittle and intracrystalline plastic deformation, respectively.

The clinopyroxene occurring intergranularly to the plagioclase in the anorthosite suggests that the plagioclase crystallised first and then the clinopyroxene. This suggestion is further supported by the shape of the clinopyroxene crystals, which are typically anhedral, which might be because the already formed plagioclase crystals restricted the development of the crystal faces of the clinopyroxene crystals. There are, however, some clinopyroxene crystals that occur as inclusions within plagioclase crystals which might suggest that some of the clinopyroxene crystals nucleated simultaneously with the plagioclase, but the plagioclase crystallisation occurred at a faster pace and ended up constraining the growth of clinopyroxene (Vernon, 2008; Nicholson, 2020).

The orthopyroxene typically occurs as medium-crystalline subhedral to euhedral crystals, which might provide insight into how crystallisation took place. The crystals could indicate that the orthopyroxene and plagioclase crystals in the anorthosite could have crystalised simultaneously. Furthermore, some of the orthopyroxene crystals exhibit cracks similar to the plagioclase crystals suggesting that it could have been affected by the same deformation event.

Phlogopite occurs as an apparently post-cumulus mineral that likely crystallised from residual fluids in the magma chamber. There are no visible signs of alteration and deformation in the phlogopite crystals, suggesting that the events responsible for the ductile and brittle deformation of the plagioclase predates phlogopite crystallisation or that the phlogopite was capable of better accommodating the deformation events. The K_2O depletion in intercumulus plagioclase probably imply that phlogopite mineralisation occurred simultaneously with the crystallisation of plagioclase.

The anorthosite-chromitite contacts contain what may be important petrographic information. The chromite crystals vary in size throughout the anorthosite-chromitite contacts. At some contacts, smaller crystals are more abundant than larger crystals. However, Mukherjee *et al.* (2017) emphasised that the sizes and distribution of the chromite crystals cannot be used to make any valid argument to support theories of flow segregation and gravity settling. This is because the chromite crystals might have undergone recrystallisation. Some of the contacts exhibit severe fracturing of the anorthosite and chromite crystals, while others have no evidence of fracturing. Nicholson (2020) speculated that these areas could be indicative of a shear zone. Alteration of the minerals is an occurrence that is sometimes observed proximal to some of the contacts. Nicholson (2020) suggested that this alteration could be due to fluids interacting with the rocks. The alteration and fracturing observed in the study area can often be linked to epidote-filled veins. These veins typically cut through the anorthosite and terminate in the chromitite layers near the contact **(Figure 17B &D)**. In some instances, the veins have also been observed orientated laterally along the contacts **(Figure 17C)**.

The anorthosite sometimes hosts some veins filled with epidote, a secondary mineral. Veins are indicative of geological processes that occurred after the formation of their host rock. Most veins are formed through the precipitation or growth of minerals into areas formed by fractures (Bons *et al*., 2012). The veins observed might provide evidence of a small-scale tectonic event, which caused the brittle deformation observed throughout the anorthosite in the form of fractures. These fractures could have provided the necessary space for the growth of the epidote veins, however, the origin of the fluid responsible for this is unknown.

The main minerals in the chromitite layers are chromite, plagioclase, clinopyroxene, and phlogopite. The plagioclase, clinopyroxene and phlogopite occur interstitial to the chromite crystals. The chromite crystals, which are the most abundant, are typically fine-crystalline (approximately 0.05 mm - 0.6 mm). The chromitite layers provide additional evidence which supports some of the observations made in the anorthosite. Firstly, bent and wedge-shaped deformation twinning in the intercumulus plagioclase indicates evidence of dislocation creep as in the anorthosite (Barnes & Maier, 2002; Nicholson, 2020). Intense alteration can be observed in various chromitite layers, especially in plagioclase, clinopyroxene, and phlogopite crystals. This suggests that the melt from which the chromitite was crystalised contained a high amount of water. This is further supported by the presence of interspersed phlogopite, possibly crystallised from residual fluids (Veksler *et al*., 2015).

4.3 Mineral chemistry

4.3.1 Plagioclase mineral chemistry

The cumulus and intercumulus plagioclase crystals exhibit significant compositional variations. The cumulus plagioclase crystals contain An% ranging from 64 – 84, and the intercumulus plagioclase crystals have a much more extensive range in An%, which ranges from 2.26 – 98.58; however, the majority of the crystals are either bytownite or oligoclase **(Table 4 & Figure 20)**. The most significant variations observed in the major element oxides of the cumulus and intercumulus plagioclase are those in K_2O, $FeO_{(tot)}$, and Cr_2O_3. Cumulus plagioclase contains more K_2O and $FeO_{(tot)}$ than intercumulus plagioclase. The Cr_2O_3 content in the intercumulus plagioclase is much higher than in the cumulus plagioclase.

The anorthite content in the cumulus plagioclase shows no significant changes laterally or vertically throughout the study area. Intercumulus plagioclase has more variable anorthite content with significant lateral variations, and there is an increase in the number of plagioclase crystals with low An% moving from sample cut D to A **(Figure 24C)**. The lack of any significant variations in the An% with depth **(Figure 24C)** reveals very little information on the evolution of the magma. Although sample cuts A and B have some lower temperature plagioclase with significantly low An%, it does not reveal much, because they occur in the same layer as the plagioclase crystals with higher An%. The fact that only intercumulus plagioclase crystals exhibit lower An% could suggest that there was some variation in the pressure when it was being crystalised (Borghini *et al*., 2011). There have been experiments by Honma (2012) which ascertained that the anorthite content of plagioclase could be affected by the amount of water in the magma from which it crystallised. In Ca-rich magmas, An% tends to be higher for low temperatures (1850 ℃) and high-water content (100 MPa). Nicholson (2020) postulated that the chromite crystals occurring interspersed with phlogopite and the severely altered minerals in the chromitite layers compared to those in the anorthosite suggests that the chromitite layers were crystalised from a melt containing more water than the melt from which the anorthosite crystallised. She further concluded that this implied that the chromitite and anorthosite layers were crystallised from melts with different compositions and water content, which supports the intrusive models for the formation of the UG1 chromitite.

The large range of anorthite content in the intercumulus plagioclase crystals in chromitite layers has been observed in the Merensky Reef (Hutchinson *et al.,* 2015). They suggested that the variable An% of the intercumulus plagioclase crystals in chromitite layers was obtained by partially melting and re-crystalising cumulus plagioclase from the anorthosite. This suggestion is further supported by the fact that the partial melting of the footwall cumulates, caused by a newly injected magma eroding the anorthosite, would release significant amounts of plagioclase into the newly introduced magma (Eales *et al.,* 1998; Eales *et al.,* 1990). This explanation supports an intrusive model for the formation of the UG1. Another explanation for the extreme compositional ranges observed in the intercumulus plagioclase crystals could be attributed to the trapped liquid shift effect (Cameron, 1977; Veksler *et al*., 2018), wherein the late crystallising intercumulus plagioclase is derived from a heavily fractionally crystallised melt composition and is not effectively buffered by re-equilibration with lots of other, more calcic, plagioclase.

Another explanation that could be provided for the behaviour of An% in the study area is that the high An% of intercumulus plagioclase suggests that it might not have crystalised from interstitial melt trapped between chromite crystals. Instead, this could imply that the plagioclase formed at the boundary of a mushy layer directly in contact with the overlying flowing magma to form a cumulus phase rather than an intercumulus phase (Campbell, 1968; Barnes *et al*., 2016; Latypov *et al*., 2017; Nicholson, 2020). This explanation implies that the chromitite is crystalised on the chamber floor, where it would be possible for the interstitial melt to interact with the overlying magma (Latypov *et al*., 2017).

The greater K_2O content in cumulus plagioclase than in intercumulus plagioclase appears to be a strange phenomenon. Under normal circumstances, intercumulus plagioclase would be enriched in K, as it is a mobile element and be deficient in the cumulus plagioclase due to its incompatibility (Nicholson, 2020). A study by Veksler *et al.,* (2015) at the Nkwe Platinum Mine on the Eastern Limb of the Bushveld records a similar phenomenon. The difference from the current study is that the plagioclase is sodic as opposed to calcic, resulting in the effective buffering of Na-Ca ratios by the plagioclase melt equilibrium. Concentrations of elements such as K, which are not necessary for the stability of plagioclase, are not buffered by the plagioclase-melt equilibrium in the melt. Therefore, K concentrations become more variable due to the pronounced effect of electrochemical migration on the concentration of K. Nicholson (2020) argued that the above interpretation argues against the intrusive models but proposes an

alternative interpretation that could possibly support an intrusive model. The alternative argues that since phlogopite incorporates a substantial amount of K during crystallisation, its presence as an intercumulus mineral in the chromitite layers could explain the depletion of K in the liquid to produce intercumulus plagioclase crystals deficient in K.

The $FeO_{(tot)}$ content of the intercumulus plagioclase is less than that of cumulus plagioclase. According to Veksler *et al.,* (2015), this is an indication of reducing conditions during intercumulus plagioclase crystallisation. They argue that the low $FeO_{(tot)}$ content is due to the lowering of plagioclase-melt $D_{Fe(Total)}$, the combined partition coefficient of both oxidation states of iron, due to the more reducing conditions as opposed to it being from the depletion of $FeO_{(tot)}$ from the intercumulus melt, which would not only be contradictory with a reasonable crystallisation model, but also the data they have collected.

4.3.2 Chromite mineral chemistry

The $FeO_{(tot)}$ and Al_2O_3 content of the massive (chromite in chromitite layers) and disseminated chromite (chromite in anorthosite layers) exhibit the most significant variations compared to all the other major element oxides. The massive chromite crystals commonly contain elevated concentrations of Al_2O_3 and lower abundances of $FeO_{(tot)}$ than what is observed in disseminated chromite crystals. The MgO content also displays variations whereby MgO content is greater in massive chromite than in disseminated chromite; this is manifested in the Mg# values. The Cr_2O_3 contents for both massive and disseminated chromite are roughly similar, with the difference being that the disseminated chromite exhibits more variable concentrations. Other noteworthy variations in the major element oxides were observed in the content of MnO, TiO_2, and V_2O_3, which tend to be more concentrated in the disseminated chromite than in the massive chromite.

The concentration of Al_2O_3 content can be explained by the fact that the cumulus plagioclase consumed most of it during crystallisation resulting in lesser concentrations being observed in the disseminated chromite. According to Nicholson (2020), the enrichment of $FeO_{(tot)}$ along with lower MgO concentrations observed in disseminated chromite compared to in massive chromite crystals, can be explained by the re-equilibration of chromite by one of the following:

1. The trapped liquid shift effect (Cameron, 1977; Veksler *et al*., 2018). The trapped liquid shift effect explains that the mineral composition of a crystallised rock unit differs from the composition of the melt from which it was crystallised due to post-cumulus modification (Nicholson, 2020; Veksler *et al*., 2018). Post-cumulus modification could be caused by the re-equilibrium of chromite with intercumulus/trapped melt, resulting in divalent and trivalent cation exchange. The other manner is through sub-solidus reactions between chromite and silicates, if cooling occurs at an adequately slow rate, which will result in an exchange of divalent cations (Nicholson, 2020; Barnes, 1998; Barnes & Roeder, 2001; Chistyakova, 2016).
2. Nicholson (2020) considered the presence and absence of plagioclase and that the chromite-melt ratios are not the only factors that control re-equilibration of chromite. There could be evidence of interstitial liquids with differing compositions in parts of the crystal mush, creating a chemical gradient (Veksler *et al*., 2018). Nicholson (2020) further stipulated that even though her study does not necessarily contain evidence of different trends of chromite in different lithologies there is sufficient evidence to support the mobility of alkali elements during the evolution of the crystal mush. According to Veksler *et al*. (2018) the dissolution of a mineral in one layer and the continuous crystallization of the same mineral in another layer can be attributed to the production of chemical gradients and element mobility.

4.4 Plagioclase Sr-isotopic composition

The in-situ plagioclase strontium isotopic data revealed that there are minor variations in the initial $^{87}Sr/^{86}Sr$ ratios. The initial $^{87}Sr/^{86}Sr$ ratios of the intercumulus plagioclase are typically greater than for cumulus plagioclase, but also considerably more variable **(Table 8)**. The greatest variations in initial $^{87}Sr/^{86}Sr$ ratios are observed within the intercumulus plagioclase (chromitite layers). Although there is no evidence of any increase or decrease in depth in the initial $^{87}Sr/^{86}Sr$ ratios, there is evidently a gradual increase laterally from sample cut D to A **(Figures 31-35)**. The most significant lateral increase occurs in the chromitite layers, more especially in the two lowermost chromitite layers in sample cuts B and A corresponding to thin sections B1-B4 and A1-A3, respectively **(Figures 34-35)**.

Table 8: Initial $^{87}Sr/^{86}Sr$ ratios ranges for cumulus and intercumulus plagioclase.

Sample cut	D	C	B	A
		Cumulus		
Range	0,7039-0,7066	0,7038-07070	0,7054-07075	0,7022-0,7073
		Intercumulus		
Range	0,7058-0,7069	0,7054-0,7088	0,7006-0,7082	0,7055-0,7097

In sample cut D **(Figure 32)** there is clearly no notable difference in the initial $^{87}Sr/^{86}Sr$ ratios between cumulus and intercumulus plagioclase, both laterally and with depth. The most noticeable variation in this sample cut is that the uppermost chromitite layer has slightly higher ratios but are however still in the same error margin as the other ratios. The second anorthosite layer from the top of the sample cut exhibits a few ratios which are much lower than the other ratios in sample cut D.

In sample cut C **(Figure 34),** most of the initial $^{87}Sr/^{86}Sr$ ratios seem to be similar, however, in a few chromitite layers there are a few ratios which are slightly more elevated than the others, although they are mostly within the same error margin as the rest of the ratios. On the second lowermost anorthosite layer in the sample cut, a lone ratio that is significantly below all the other ratios is also noted.

The initial $^{87}Sr/^{86}Sr$ ratios observed in sample cut B **(Figure 34)** are mostly within the same range. However, it is noteworthy to mention that most of the chromitite layers tend to have slightly elevated ratios than the anorthosite layers.

Sample cut A **(Figure 35)** reveals more significant variations in the initial $^{87}Sr/^{86}Sr$ ratios than any other sample cut. From the uppermost chromitite layer to the third layer there is a slight decrease in the initial $^{87}Sr/^{86}Sr$ ratios. From the third layer to the lower most chromitite layer there is a more pronounced increase in the initial $^{87}Sr/^{86}Sr$ ratios. This lower most layer returned ratios that are more radiogenic and a local maximum in the order of 0.709 -0.710 were obtained. The anorthosite layers exhibit initial $^{87}Sr/^{86}Sr$ ratios within a similar range as in the other sample cuts.

It might also be noteworthy to mention that the lowermost chromitite layer in sample cut D splits and the upper offshoot merges with the uppermost chromitite layer from sample cut D in

sample cut A **(Figure 31)**. The initial $^{87}Sr/^{86}Sr$ ratios for these chromitite layers remain mostly consistent throughout the sample cuts. However, for the lower offshoot of the lowermost layer in sample cut D, the initial $^{87}Sr/^{86}Sr$ ratios vary considerably, which increases from sample cut D to A **(Figure 31)**.

From a Sr-isotopic perspective, the following interpretations may hold true:

1. A lack of significant variations in the Sr-isotopic composition across chromitite bifurcations might suggest that there was no addition of a new magma into the chamber. However, such an explanation would not meet the mass balance requirements, as the Cr contained in a typical basaltic magma is typically around 300 ppm and can only crystallise one thick chromitite layer, after which the resident magma will be depleted in Cr (Pebane & Latypov, 2017).
2. A lack of significant Sr-isotopic variations may be expected if there were influxes of new magma into the chamber, but the magmas had the same isotopic signatures as the resident melt to account for the limited variations observed in the initial $^{87}Sr/^{86}Sr$ ratios.
3. A lack of significant Sr-isotopic variations across bifurcated chromitite layers may even be explained if magmas that were isotopically distinct from the resident magma did enter the chamber, with the lack of any substantial variations in initial $^{87}Sr/^{86}Sr$ ratios resulting from a large reservoir of melt which buffered any resolvable changes to the system.

The initial $^{87}Sr/^{86}Sr$ ratios published by Kinnaird *et al.* (2002) from core BK and SK9 from the Western and North-western Bushveld Complex respectively **(Figure 36-37)**, reveal slightly similar patterns as in those obtained from Shaft No.11 of Impala Platinum Limited in the Western Limb of the Bushveld Complex. Their data reveal that there are some intercumulus plagioclase that exhibit anomalously higher ratios in the chromitite layers and stringers than in the cumulus plagioclase from the anorthosite layers (Kinnaird *et al*., 2002). This data led to the assumption that every chromitite layer was the result of a new magma pulse (Kinnaird *et al*., 2002; Kinnaird *et al*., 2005). Although the authors do not directly make mention of chromitite bifurcations, it provides some insight into how chromitite bifurcations were formed.

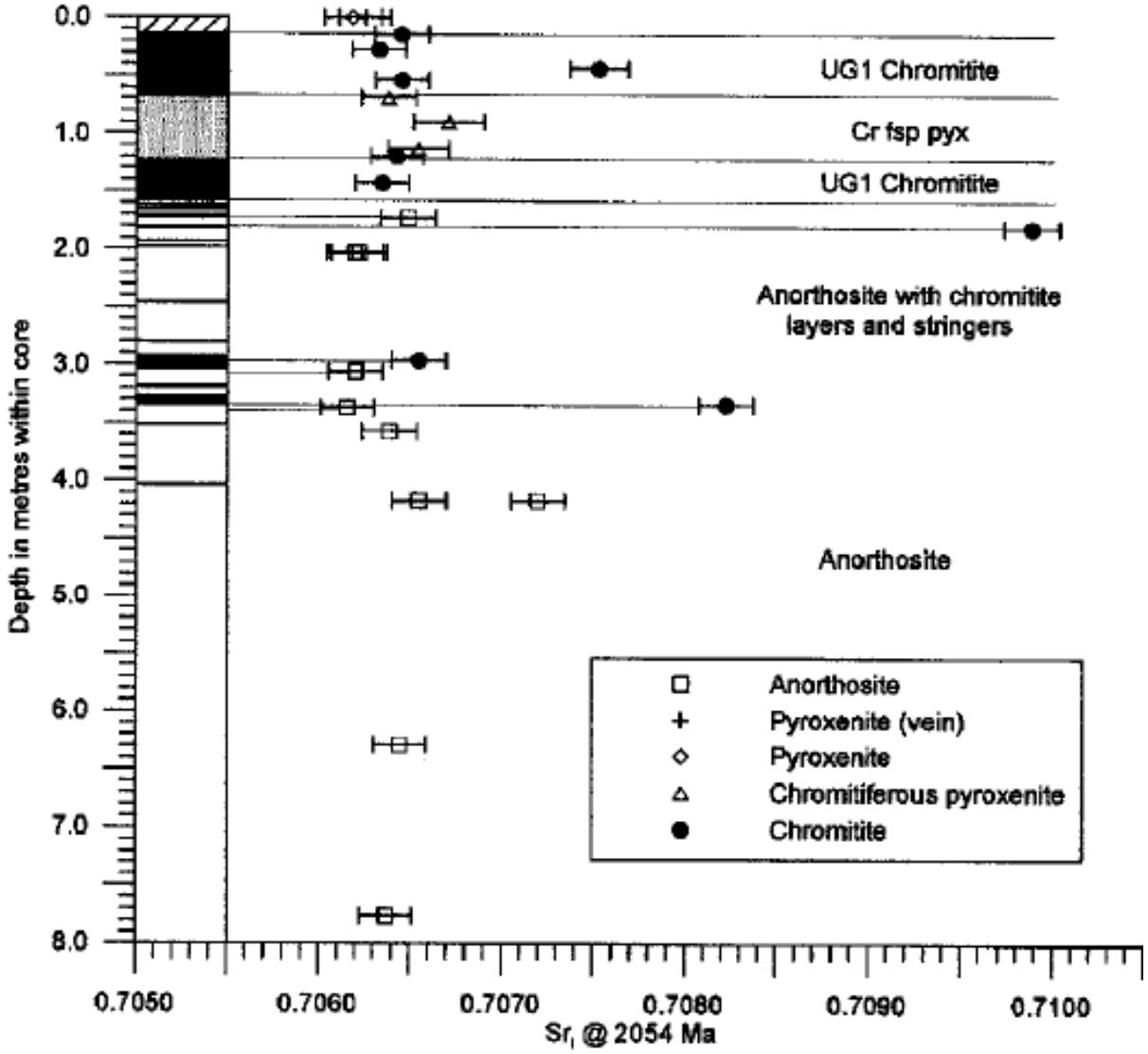

Figure 36: Initial strontium isotope ratio profile through the UG1 chromitite package, footwall anorthosite and hanging wall pyroxenite from core BK obtained in the Western Bushveld. Horizontal bars indicate 2SE error for Sr values. Note high initial $^{87}Sr/^{86}Sr$ ratios in chromitite-hosted interstitial plagioclase samples, with highest values in footwall chromitite stringers. From Kinnaird *et al.* (2002)

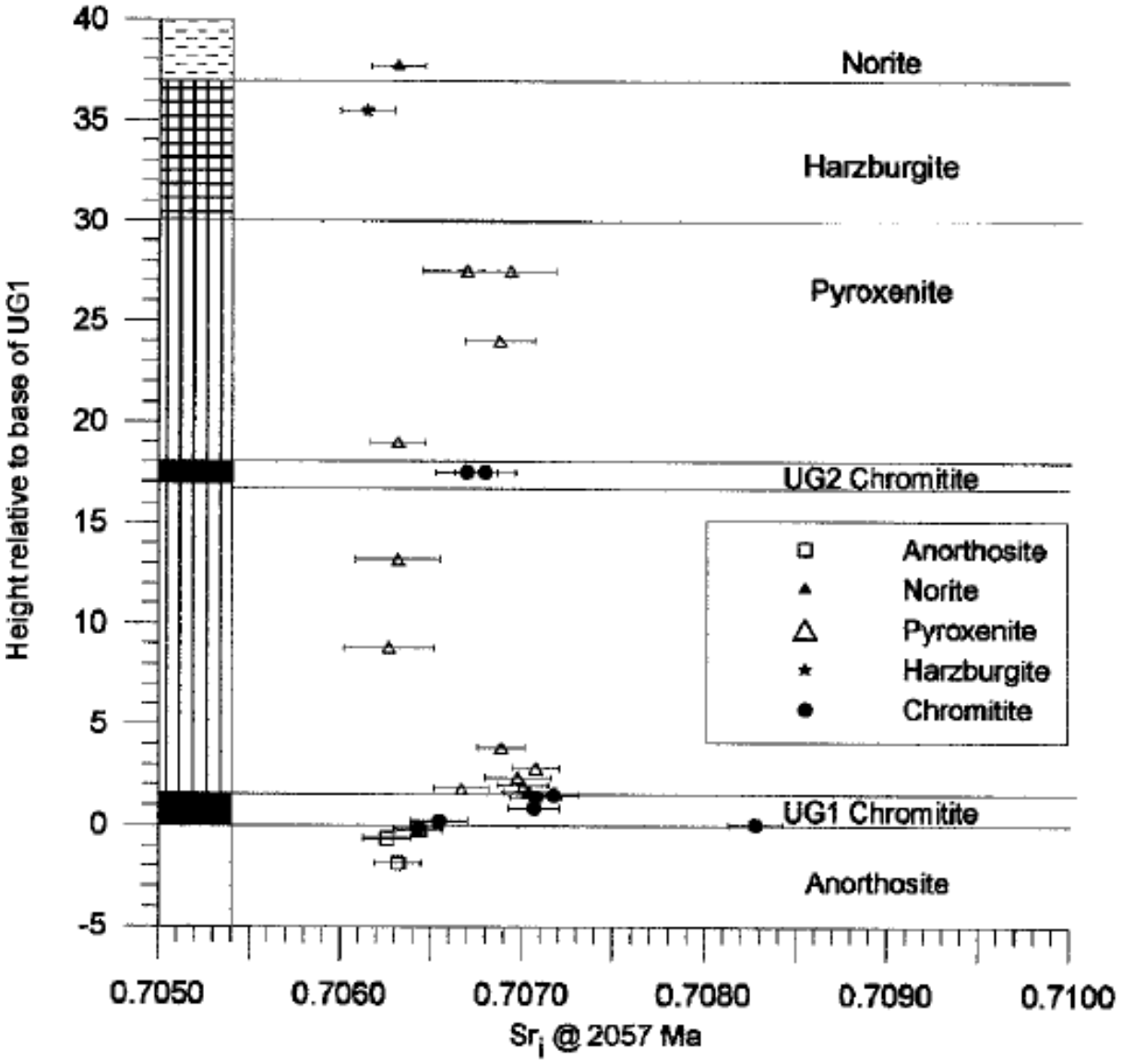

Figure 37: Initial strontium isotope ratio profile for UG1 footwall anorthosite through hanging-wall pyroxenite and harzburgite to norite above UG2. Data from core SK9, Union section, northwest Bushveld, de Klerk (unpublished data) and Schoenberg *et al.*, 1999. Horizontal bars indicate 2SE error for Sr values as published in Kinnaird *et al*. (2002).

5 Conclusion

The field relations, petrography and geochemical data collected in this study has led to several observations which provide some insight into how the chromitite bifurcations at Shaft no.11 at Impala Platinum Ltd were formed. Before any hypothesis can be drawn up it is imperative to note some of the significant differences and similarities of the current study area with what other researchers have observed at Dwars River Locality (DRL) and other areas that have been studied.

In the current study area, there is an absence of well-defined anorthosite lenses unlike what has been reported by Cawthorn (2003), Nex (2004), Voordouw *et al.* (2009), Cawthorn (2015), and Pebane & Latypov (2017) from other localities. The absence of distinct anorthosite lenses in the current study area does not necessarily refute previous models but makes it clear that there could have been different processes involved in the formation of bifurcations at different localities, including those that do not require the formation of anorthosite lenses as pointed out by Nicholson (2020).

Another observation is that there are very few anorthosite inclusions in the current study area in comparison to what Pebane & Latypov (2017) reported at the DRL. Not only are they fewer, but there have also been some differences observed, such as wisp tail of inclusions at DRL, which have not been observed at the Shaft No. 11. According to Nicholson (2020), the fact that these inclusions are not partially attached to the anorthosite could possibly contradict intrusive models (e.g., Lee, 1981 and Voordouw *et al.*, 2009), but this could also be explained by the forceful injection of a chromitite rich slurry resulting in the displacement of the inclusions, as proposed by Pebane & Latypov (2017).

The concordant manner in which the thin chromitite layers occur is another noteworthy observation. This layering suggests the chromite layers were formed due to gravity settling or in-situ crystallisation on the chamber floor. The presence of small-scale pothole structures observed in the study area may support the hypotheses of Mukherjee *et al.* (2017) and Pebane & Latypov (2017) that thermo-chemical erosion was integral in the formation of chromitite bifurcations.

What can be drawn from the petrography is that: (1) brittle deformation occurred after ductile deformation. Evidence of this is seen in the fractures cutting across the bent and wedge-shaped deformation twins in plagioclase crystals. (2) According to Nicholson (2020) the anorthosite-chromitite with highly fractured chromite crystals are indicative of a shear zone or an area of high brittle deformation. (3) There is also evidence of fluid in the system, which is made evident by the presence of micro veins, altered minerals and phlogopite, a hydrous mineral. Phlogopite and alteration is more abundant in the chromitite layers, indicating that fluids were more abundant than in the anorthosite layers. The thin chromitite layers which occur within the anorthosite layers are an indication of post cumulus textural growth (Nicholson, 2020). (4) The fractured cumulus plagioclase crystals (in anorthosite layers) and the elongated massive chromite crystals (in chromitite layers) at the anorthosite-chromitite boundaries provide evidence of a rheological contrast during emplacement, the anorthosite being more brittle and the chromitite ductile. This, along with the overlapping of plagioclase and chromite crystals, provides evidence that the anorthosite was likely emplaced as a plagioclase mush and the chromitite as a chromite-rich slurry.

The mineral chemistry of the plagioclase and chromite crystals has led to the following conclusions: (1) The high anorthite content observed in plagioclase from the chromitite layers could mean that they are not truly intercumulus. If it were truly intercumulus, the anorthite content would be considerably lower than that observed in cumulus plagioclase (Nicholson, 2020). The anorthite content in the intercumulus plagioclase could also be affected by factors such as different magma compositions, temperature, pressure and water content (Nicholson, 2020). (2) The low concentrations of K_2O and Na_2O observed in plagioclase from chromitite layers could be as a result of selective migration of alkali in the layers, implying that chromitite crystalized along the chamber floor, thus refuting intrusive models (Nicholson, 2020). However, the depletion of K_2O in the chromitite layers could also suggest that the phlogopite associated with these layers was mineralised simultaneously with the plagioclase and therefore, used up the K_2O. The trends observed in the $FeO_{(tot)}$ and MgO concentrations in the chromite crystals can be explained by re-equilibration caused by either (1) the trapped liquid shift or (2) the production of chemical gradients and element mobility. According to Nicholson (2020) these compositional differences observed do not necessarily indicate that the massive and disseminated chromite crystals were produced from compositionally different magmas.

The initial $^{87}Sr/^{86}Sr$ ratios reveal no significant variations with depth in the sample cuts and in the two plagioclase phases observed. This could imply that (1) there was no involvement of isotopically different magmas being injected into the magma chamber. (2) The magmas intruding into the chamber could have had similar isotopic signatures. (3) The magmas that intruded into the magma chamber had distinct isotopic signatures, but there was a large reservoir of melt which buffered any changes that could have occurred.

Based on the morphology of the study area along with the above petrographic and geochemical interpretations, it is probable that the following processes were involved in the formation of chromitite bifurcations:

1. The occurrence of an anorthosite footwall observed in the study must be explained first to be able elaborate on how the chromitite bifurcations were formed. For this, it is envisaged that a partially consolidated anorthosite mush, on the chamber floor, was thermo-chemically eroded resulting in an irregular floor **(Figure 38A)**.
2. It is proposed that the thick chromitite layer at the base was formed by the intrusion of a chromite-rich slurry that subsequently settled on the irregular anorthosite floor. This explanation for the development of the thick basal chromitite layer is preferred, as it accounts for mass balance requirements (Eales & Cawthorn, 1996) **(Figure 38 B)**.
3. This was followed by the development of anorthosite-chromitite cyclic units which formed chromitite bifurcations above the basal chromitite layer. When this occurred, the system was most probably close to the cotectic and moved between the plagioclase and chromite stability fields due to fluctuations in the pressure caused by roof rupturing events, magma influxes, or even as a result of shock waves from seismic activity. The presence of a large reservoir of melt that buffers compositional and isotopic changes provides the best explanation for the limited variation in the anorthite content and initial $^{87}Sr/^{86}Sr$ isotope ratios **(Figure 38 C)**.
4. The intrusion of a second chromite-rich slurry, which leads to renewed thermo-chemical erosion and the deposition of the thick, upper chromitite layer, with the thin chromitite layers now appearing as offshoots from the base of this layer **(Figure 38D)**.
5. The underlying cumulates probably had fractures or weak zones extending to the basal chromitite layer, introduced by events such as seismic activity in the area. These fractures/weak zones provided the newly intruded chromitite slurry with pathway to intrude downward to the basal chromitite layers, allowing for the development of the thick chromitite offshoots, connecting the two thick upper and basal chromitite layers.

Some of the fractures were less prominent and only resulted in development of more bifurcations as they were infiltrated by the slurry **(Figure 38E)**.

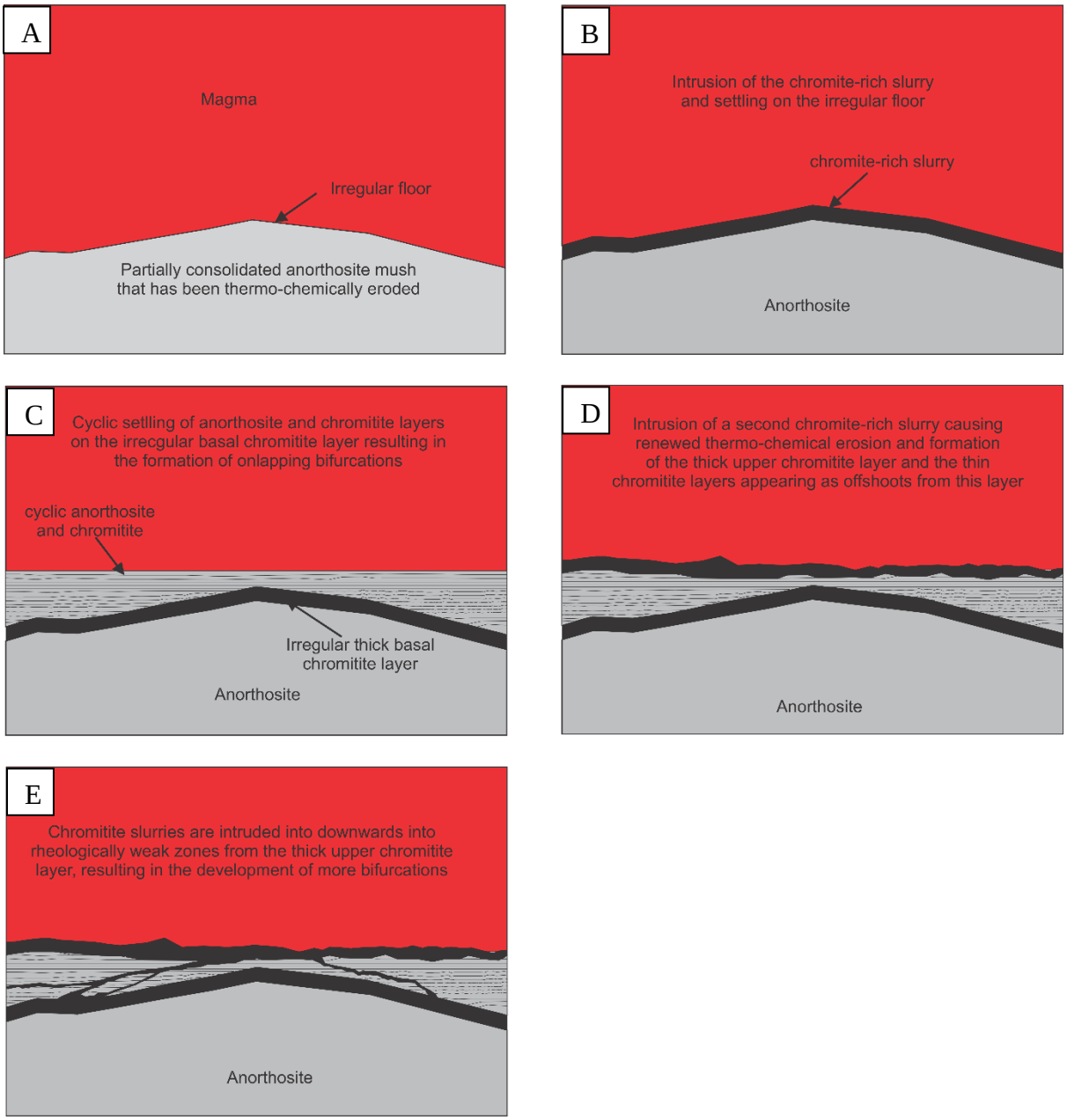

Figure 38: Conceptual model for the development of chromitite bifurcations at Shaft No. 11 of Impala Platinum Mine, Rustenburg.

This model was developed with the aid of interpretations from other researchers. It incorporates theory that floor cumulates were thermo-chemically eroded, as proposed by Pebane & Latypov (2017) and Mukherjee *et al.* (2017), as well as the idea that chromite-rich slurries were responsible for the formation of chromitite layers by Voordouw *et al.* (2009). The model also takes into consideration the theory of Cawthorn (2015), that there were some pressure changes in the magma chamber responsible for the deposition of thin chromitite layers. It is clear that

based on the field observations obtained from the Dwars River Locality (e.g. Cawthorn, 2003; Nex, 2004; Voordouw *et al.*, 2009; Pebane & Latypov, 2017), as well as those from other locations (e.g. Nex, 2004; Cawthorn, 2015; Mukherjee *et al.*, 2017; Nicholson, 2020), including the current study area, that not all of the studied bifurcations are the same. This implies that there is no one model that can completely explain the formation of chromitite bifurcations.

6 References

- Barnes, S.-J., 1998. Chromite in komatiites, 1. Magmatic controls on crystallization and composition. *Journal of Petrology,* **39(10)**, pp. 1689-1720.

- Barnes, S.-J. & Maier, W. D., 2002. Platinim-group elements and microstructures of normal Merensky Reef from Impala Platinum mines, Bushveld Complex. *Journal of Petrology,* **43(1)**, pp. 103-128.

- Barnes, S.-J., Mole, D. R., Le Vaillant, M., Campbell, M. J., Verrall, M. R., Roberts, M. P. & Evans, N. J., 2016. Poikilitic textures, heteradcumulates and zoned orthopyroxenes in the Ntaka Ultramafic Complex, Tanzania: implications for crystallization mechanisms of oikocrysts.. *Journal of Petrology,* **57**, pp. 1171-1198.

- Barnes, S.-J. & Roeder, P. L., 2001. The range of spinel compositions in terrestrial mafic and ultramafic rocks. *Journal of Petrology,* **12(12)**, pp. 2279-2302.

- Bons, P. D., Elburg, M. A. & Gomez-Rivas, E., 2012. A review of the formation of tectonic veins and their microstructures. *Journal of Structural Geology,* **43**, pp. 32-62.

- Borghini, G., Fumagalli, P. & Rampone, E., 2011. The geobarometric significance of plagioclase in mantle peridoites: A link between nature and experiments. *Lithos,* **126**, pp. $42^{-5}3$.

- Cameron, E. N., 1977. Chromite in the central sector of the Eastern Bushveld Complex, South Africa. *American Mineralogist,* **62**, pp. 1082-1096.

- Cameron, E. N., 1978. The Lower Zone of the Eastern Bushveld Complex in the Oliphants River Trough. *Journal of Petrology,* **19**, pp. 437-462.

- Campbell, I. H., 1968. The origin of heteradcumulate and adcumulate textures in the Jimberlana Norite. *Geological Magazine,* **105**, pp. 378-383.

- Cawthorn, R. G., 2003. Genesis of magmatic oxide deposits - a view from the Bushveld Complex. *Norges geologiske undersøkelse, Special Publication,* **9**, pp. 11-21.

- Cawthorn, R.G. 2015. The Bushveld Complex, South Africa, *In*: Charlier, B., Namur, O., Latypov, R., Tegner, C (eds), *Layered Intrusions.* 1st ed. New York: Springer, pp. 517 – 587

- Cawthorn, R. G. & Walraven, F., 1998. Emplacement and crystallization time for the Bushveld Complex. *Journal of Petrology,* **39(9)**, pp. 1669 - 1687.

- Chistyakova, S., 2016. Chromitite dykes in the in the Monchegorsk Layered Intrusion, Russia: In-situ crystallization from chromite-saturated magma flowing in conduits. *Journal of Petrology*, **56(12)**, pp. 2395-2424.

- Chitiyo, G., Schweitzer, J., De Waal, S., Lambert, P. & Ogilvie, P., 2008. Predictability of pothole characteristics and their spatial distribution at Rustenburg Platinum Mine (Rustenburg Section). *The Southern African Institute of Mining and Metallurgy,* **12(108)**, pp. 733-740.

- Clarke, B., Uken, R. & Reinhardt, J., 2009. Structural and compositional constraints on the emplacement of the Bushveld Complex, South Africa. *Lithos*, **111**, pp. 21-36.

- Eales, H.V. & Cawthorn, R.G. 1996. The Bushveld Complex pp. 181-230. *In*: Cawthorn, R.G. (eds), *Layered Intrusions.* Elsevier, Amsterdam, 531pp.

- Eales, H. V., De Klerk, W. J. & Teigler, B., 1990. Evidence for magma mixing processes within the Critical and Lower Zones of the northwestern Bushveld Coomplex, South Africa,. *Chemical Geology*, **88**, pp. 261-278.

- Eales, H. V., Field, M., De Klerk, W. J. & Scoon, R. N., 1988. Regional trends of chemical variation and thermal erosion in the Upper Critical Zone, Western Bushveld Complex. *Mineralogical Magazine,* **52**, pp. 63-79.

- Elburg, M., Vroon, P., van der Wagt, B., Tchalikian, A., 2005. Sr and Pb isotopic composition of five USGS glasses (BHVO-2G, BIR-1G, BCR-2G, TB-1G, NKT-1G). *Chemical Geology*, **223**, pp. 196-207.

- Honma, U., 2012. Hydrous and anhydrous melting experiment of an alkali basalt and a transitional tholeiite from the Oginosen volcano, Southwest Japan: The possible influence of melt depolymerization on Ca-Na partitioning between plagioclse and the melt. *Journal of Mineralogical and Petrological Sciences*, **107**, pp. 8-32.

- Hutchinson, D., Foster, J., Prichard, H. & Gilbert, S., 2015. Concentration of particulate platinum-group minerals during magma emplacement; a case study from the Merensky Reef, Bushveld Complex. *Journal of Petrography,* **56(1)**, pp. 113-159.

- Kiefer, R. & Viljoen, M. J., 2006. PGE exploration targets to the west of the Pilanesberg, South Africa. *South African Journal of Geology,* **109**, pp. 459-474.

- Kinnaird, J. A., Hutchinson, D., Schurmann, L., Nex, P. A. M. & de Lange, R., 2005. Petrology and mineralisation of the southern Platreef: nothern limb of the Bushveld Complex, South Africa. *Mineralium Deposita,* **40**, pp. 576^{-5}97.

- Kinnaird, J. A., Kruger, K. A., Nex, P. A. M. & Cawthorn, R. G., 2002. Chromitite formation—a key to understanding processes of platinum enrichment. *Applied Earth Science,* **111(1)**, pp. 23-35.

- Latypov, R., Chistyakova, S. & Mukherjee, R., 2017. A novel hypothesis for origin of massive chromitites in the Bushveld Igneous Complex.. *Journal of Petrology*, **58(10)**, pp. 1899-1940.

- Lee, C.A. 1981. Post-deposition structures in the Bushveld Complex mafic sequence. *Journal of the Geological Society*, **138**, pp. 327-341.

- Li, C., Ripley, E. M. & Merino, E., 2004. Replacement of base metal sulfides by actinolite, epidote, calcite, and magnetite in the UG2 and Merensky Reef of the Bushveld Complex, South Africa. *Economic Geology*, **99**, pp. 173-184.

- Maghdour-Mashhour, R. & Hayes, B., 2021. A turbulent magmatic density current and the origin of the anastomosing UG-1 chromitites at Dwars River in the Bushveld Complex. *Journal of Petrology,* **62(7)**, pp. 1-23.

- Magson, J., Roelofse, F., Bybee, G. & Bolhar, R., 2023. Constraints on the Nd-isotopic composition and nature of the last major infux of magma into the Bushveld Complex. *Contributions to Mineralogy and Petrology*, **178(14)**, pp. 1-17.

- Maier, W. D., Barnes, S. -J. & Groves, D. I., 2013. The Bushveld Complex, South Africa: formation of platinum–palladium, chrome- and vanadium-rich layers via hydrodynamic sorting of a mobilized cumulate slurry in a large, relatively slowly cooling, subsiding magma chamber. *Mineralium Deposita*, **48**, pp. 1-56.

- Mitchell, A. A., 1990. The stratigraphy, petrography, and mineralogy of the northwestern Bushveld Complex. *South African Journal of Geology*, **93**, pp. 818-831.

- Molyneux, T. G., 1974. A geological investigation of the Bushveld Complex in Sekhukhuneland and part of the Steelport Valley. *South African Journal of Geology*, **77**, pp. 329-338.

- Mukherjee, R., Latypov, R., Balakrishnan, A. 2017. An intrusive origin of some massive chromitite layers: insights from field relationships at the Impala Platinum Mine, Bushveld Igneous Complex. *Ore Geological Reviews*, **90**, pp. 94-109.

- Nebel, O., Scherer, E. E. & Mezger, K., 2011. Evaluation of the ^{87}Rb decay constant by age comparison against the U-Pb system. *Earth and Planetary Science Letters,* **301**, pp. 1-8.

- Nex, P. A. M., 2004. Formation of bifurcating chromitite layers of the UG1 in the Bushveld Igneous Complex, an analogy with sand volcanoes. *Journal of the Geological Society, London,* **161**, pp. 903-909.

- Nex, P. A. M., Kinnaird, J. A., van der Vyver, B. A., Ingle, L. J. & Cawthorn, R. G., 1998. A new stratigraphy for the Main Zone of the Bushveld Complex, in the Rustenburg area. *South African Journal of Geology,* **101**, pp. 215-223.

- Nicholson, M., 2020. A geochemical and petrological investigation of bifurcating chromitite layers of the UG1 at the Impala Platinum mine, Rustenburg.. *Unpublished Masters Dissertation*, University of the Free State, Bloemfontein, 130pp.

- Pebane, M. & Latypov, R., 2017. The significance of magmatic erosion for bifurcation of UG1 chromitite layers in the Bushveld Complex. *Ore Geology Reviews,* **90**, pp. 65-93.

- Sampson, E., 1932. Magmatic chromite deposits in Southern Africa. *Economic Geology*, **27**, pp. 113-144.

- Schoenberg, R., Kruger, F. J., Nägler, T. F., Meisel, T. & Kramers, J. D., 1999. PGE enrichment in chromitite layers and the Merensky Reef of the western Bushveld Complex; a Re–Os and Rb–Sr isotope study.. *Earth and Planetary Science Letters,* **172(1-2)**, pp. 49-64.

- Scoon, R. N., Costin, G. & Gräbe, P. J., 2017. Geology and origin of the vanadiferous Fe-Ti oxide-rich Kennedy's Vale discordant body, Eastern Limb of the Bushveld Complex, South Africa. *South African Journal of Geology*, **120(2)**, pp. 251-270.

- Smith, D., Basson, I. & Reid, D., 2004. Normal Reef subfacies of the Merensky Reef at Northam Platinum Mine, Zwartklip facies, Western Bushveld Complex, South Africa. *Canadian Mineralogist,* **42**, pp. 243-260.

- Veksler, I. V., Reid, D. L., Dulski, P., Keiding, J. K., Schannor, M., Hecht, L. & Trumbull, B., 2015. Electrochemical processes in a crystal mush: cyclic units in the Upper Critical Zone of the Bushveld Complex, South Africa. *Journal of Petrology,* **56(6)**, pp. 1229-1250.

- Veksler, I. V., Sedunova, A. P., Darin, A. V., Anosova, M. O., Reid, D. L., Kaufmann, F. E. D., Hecht, L. & Trumbull, R. B., 2018. Chemical and textural re-equilibration in the UG2 chromitite layer of the Bushveld Complex, South Africa. *Journal of Petrology,* **59(6)**, pp. 1193-1216.

- Vernon, R. H., 2008. *Microstructures of igneous rocks.* 2nd ed. Cambrige: Cambridge University Press.

- Voordouw, R., Gutzmer, J. & Beukes, N. J., 2009. Intrusive origin for Upper Group (UG1, UG2) stratiform chromitite seams in the Dwars River area, Bushveld Complex, South Africa. *Mineralia Petrology,* **97**, pp. 75-94.

- Yao, Z., Mungall, J. E. & Jenkins, M. C., 2021. The Rustenburg Layered Suite formed as a stack of mush with transient magma chambers. *Nature Communications,* **12**, pp. 1-13.

- Zeh, A., Ovtcharova, M., Wilson, A. H. & Schaltegger, U., 2015. The Bushveld Complex was emplaced and cooled in less than one million years - results of zirconology, and geotectonic implications. *Earth an Planetary Science Letters,* **418**, pp. 103-114.

Appendices

Appendix A – Modal mineralogy

Appendix B – Plagioclase mineral chemistry data

Appendix C – Chromite mineral chemistry data

Appendix D – In-situ strontium isotope data

Appendix A

Anorthosite host rock modal mineralogy

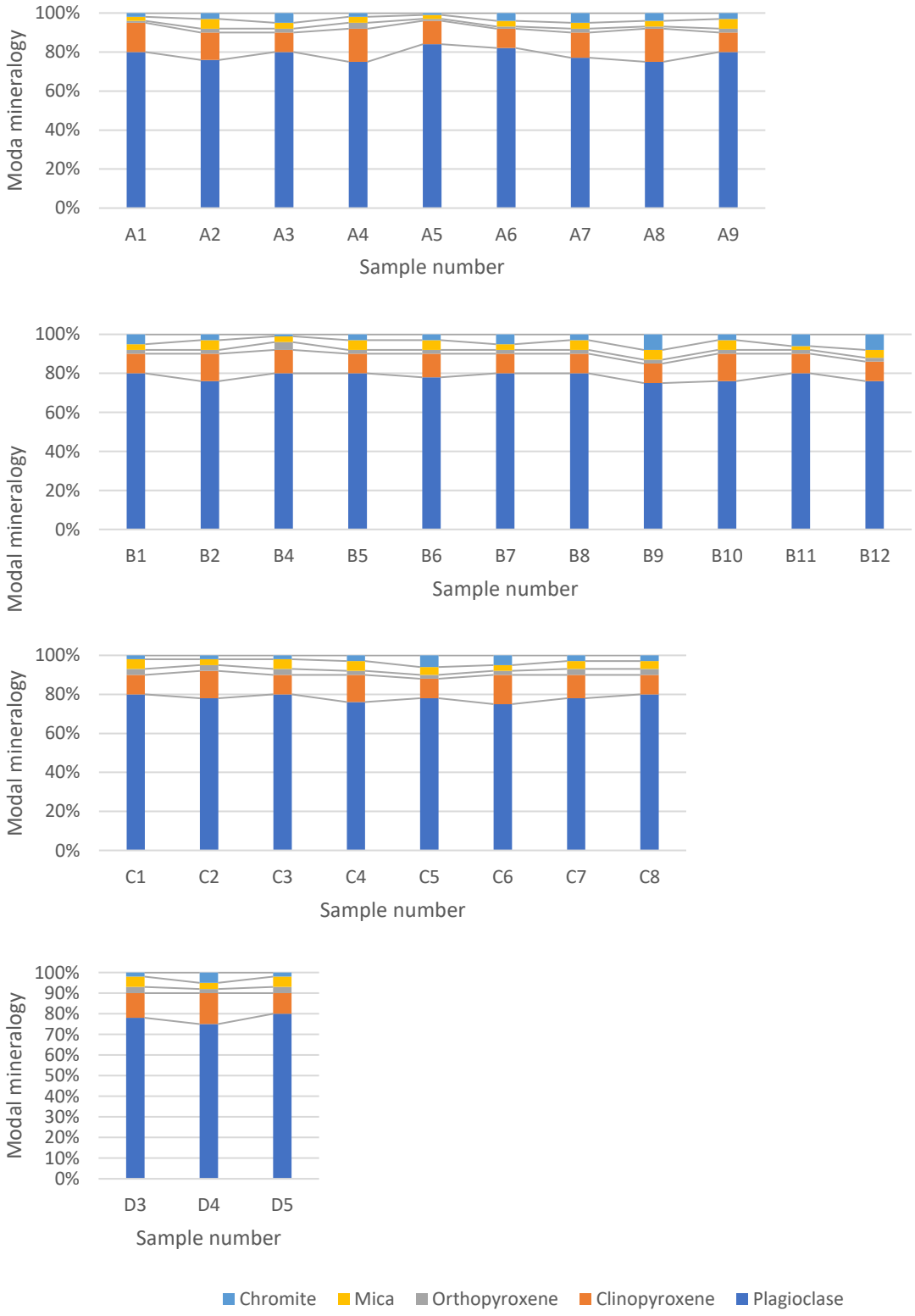

Chromitite modal mineralogy

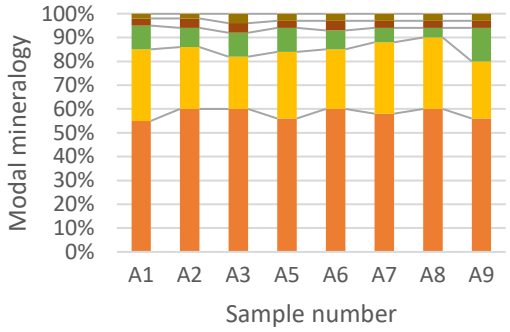

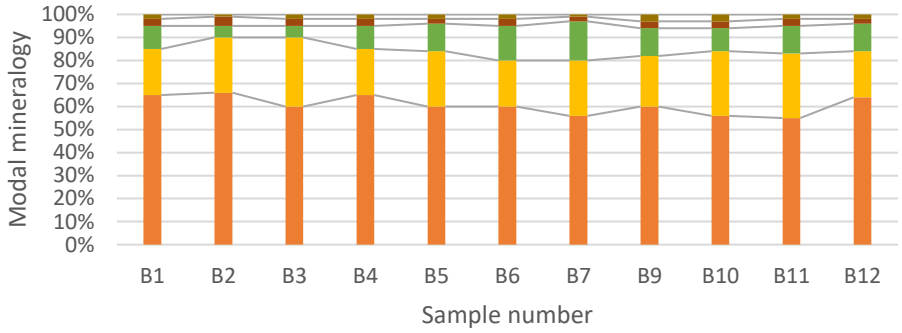

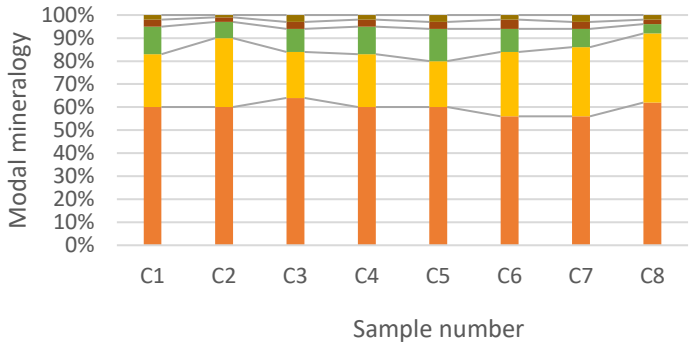

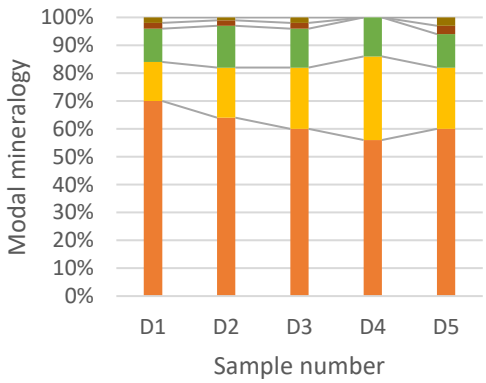

Appendix B – Plagioclase mineral chemistry

Table B-1: Electron Microprobe data for plagioclase minerals in anorthosite layers (cumulus plagioclase) (wt.%).

						A							
Sample number	**SiO_2**	**TiO_2**	**Al_2O_3**	**Cr_2O_3**	**$FeO_{(tot)}$**	**MnO**	**MgO**	**CaO**	**NiO**	**Na_2O**	**K_2O**	**Total**	**An%**
A1	48,46	0,01	32,09	0,01	0,16	0,01	0,04	16,25	0,02	2,43	0,09	99,57	78,28
A1	49,40	0,01	31,11	n.d	0,18	n.d	0,03	15,13	n.d	3,02	0,15	99,04	72,84
A1	49,52	n.d	31,43	n.d	0,20	0,01	0,02	15,33	n.d	2,94	0,15	99,59	73,62
A1	49,24	0,01	31,35	0,01	0,19	n.d	0,02	15,42	n.d	2,86	0,17	99,26	74,14
A1	48,86	0,01	31,13	n.d	0,19	n.d	0,02	15,52	0,01	2,87	0,16	98,76	74,27
A1	49,27	0,03	31,21	0,01	0,19	0,01	0,01	15,42	n.d	2,91	0,17	99,22	73,83
A1	49,18	0,02	31,58	n.d	0,16	0,00	0,02	15,47	n.d	2,91	0,17	99,51	73,86
A1	49,18	0,02	31,23	n.d	0,19	n.d	0,02	15,45	n.d	2,85	0,16	99,09	74,31
A1	50,53	0,01	30,49	0,01	0,19	n.d	0,02	14,41	n.d	3,40	0,21	99,27	69,24
A1	49,12	0,02	31,26	n.d	0,20	0,01	0,01	15,44	0,02	2,91	0,17	99,15	73,83
A2	48,71	0,01	31,65	n.d	0,21	n.d	0,01	15,65	n.d	2,73	0,14	99,12	75,39
A2	49,04	0,01	31,35	n.d	0,22	0,00	0,03	15,50	n.d	2,88	0,14	99,17	74,20
A2	49,11	0,02	31,57	n.d	0,20	0,01	0,02	15,61	n.d	2,81	0,17	99,51	74,73
A2	49,10	0,01	31,49	n.d	0,22	n.d	0,02	15,59	0,01	2,86	0,13	99,43	74,49
A2	48,66	0,03	31,63	n.d	0,24	n.d	0,02	15,80	0,00	2,73	0,14	99,24	75,59
A2	48,99	0,02	31,48	n.d	0,21	n.d	0,03	15,44	0,02	2,79	0,17	99,14	74,61
A2	48,30	n.d	31,95	0,01	0,21	n.d	0,02	16,22	n.d	2,51	0,13	99,34	77,60
A2	49,20	0,02	31,21	0,01	0,23	n.d	0,02	15,38	0,00	2,94	0,18	99,19	73,52
A2	49,47	0,01	31,21	n.d	0,24	0,00	0,01	15,12	n.d	3,09	0,18	99,34	72,23
A2	48,81	0,00	31,21	n.d	0,23	n.d	0,02	15,51	n.d	2,86	0,19	98,84	74,17
A3	48,93	0,02	31,51	n.d	0,14	n.d	0,02	15,54	0,00	2,87	0,11	99,14	74,50
A3	48,63	0,02	31,48	n.d	0,12	n.d	0,04	15,68	0,02	2,82	0,08	98,90	75,05
A3	49,41	0,03	31,23	n.d	0,16	0,01	0,02	15,37	n.d	3,06	0,10	99,39	73,09
A3	49,32	0,02	31,00	n.d	0,21	0,01	0,02	15,10	0,00	3,03	0,19	98,91	72,61
A3	49,50	n.d	30,98	n.d	0,21	0,02	0,01	15,21	0,02	3,14	0,16	99,25	72,15
A3	49,47	0,02	31,02	n.d	0,19	0,01	0,02	15,03	n.d	3,12	0,18	99,06	71,93
A3	49,67	0,02	30,98	n.d	0,19	0,00	0,02	15,01	0,01	3,06	0,17	99,12	72,38
A3	48,95	0,01	31,51	n.d	0,17	0,00	0,02	15,66	n.d	2,79	0,14	99,24	74,99
A3	49,39	0,02	31,20	n.d	0,18	n.d	0,03	15,29	n.d	2,91	0,16	99,16	73,73
A4	49,18	0,05	31,20	n.d	0,28	n.d	0,01	15,45	n.d	2,90	0,17	99,23	73,97
A4	49,23	0,03	31,28	0,01	0,27	n.d	0,01	15,51	0,01	2,73	0,17	99,25	75,06
A4	48,94	0,02	31,37	n.d	0,26	0,01	0,01	15,48	0,01	2,78	0,16	99,05	74,79
A4	49,67	0,01	30,78	n.d	0,25	0,01	0,02	14,83	n.d	3,34	0,19	99,09	70,28
A4	49,33	0,03	31,14	0,01	0,26	0,00	0,03	15,28	0,02	3,04	0,19	99,32	72,75
A4	49,52	0,02	31,04	n.d	0,24	0,00	0,02	15,21	n.d	3,03	0,20	99,28	72,70
A4	49,34	0,02	31,21	n.d	0,25	n.d	0,02	15,29	0,01	3,02	0,17	99,32	72,97
A4	49,08	0,02	31,39	0,01	0,22	0,02	0,02	15,45	n.d	2,83	0,16	99,18	74,42
A4	49,37	0,03	31,11	0,02	0,21	0,01	0,02	15,27	n.d	2,97	0,18	99,19	73,18
A5	49,05	0,02	31,53	0,02	0,19	0,00	0,02	15,60	n.d	2,82	0,15	99,40	74,73
A5	49,61	0,02	30,75	n.d	0,17	0,00	0,02	15,01	n.d	3,17	0,16	98,90	71,73
A5	49,73	0,02	30,97	n.d	0,18	0,01	0,03	15,00	0,01	3,06	0,17	99,17	72,32
A5	49,03	0,04	31,49	n.d	0,16	0,01	0,03	15,64	n.d	2,77	0,16	99,31	75,04
A5	49,35	0,01	31,31	n.d	0,18	n.d	0,03	15,46	0,02	2,91	0,16	99,42	73,92
A5	48,91	n.d	31,40	0,01	0,17	n.d	0,03	15,71	0,01	2,78	0,14	99,17	75,12
A6	51,71	0,02	29,77	n.d	0,14	0,00	0,03	13,35	0,01	3,96	0,23	99,22	64,21
A6	49,81	0,01	31,33	0,01	0,14	0,01	0,03	15,16	0,02	3,03	0,14	99,68	72,84

Table B-1: Continued

A													
Sample number	**SiO_2**	**TiO_2**	**Al_2O_3**	**Cr_2O_3**	**$FeO_{(tot)}$**	**MnO**	**MgO**	**CaO**	**NiO**	**Na_2O**	**K_2O**	**Total**	**An%**
A6	49,26	0,04	31,34	n.d	0,12	0,01	0,01	15,38	0,01	2,93	0,15	99,24	73,71
A6	49,50	0,01	31,32	n.d	0,12	0,00	0,02	15,34	0,01	2,96	0,14	99,42	73,56
A6	49,29	0,02	31,43	n.d	0,13	0,01	0,01	15,55	n.d	2,79	0,14	99,37	74,87
A6	47,98	0,02	32,19	n.d	0,12	0,01	0,00	16,39	n.d	2,36	0,09	99,17	78,91
A6	49,25	0,02	31,45	0,01	0,15	0,02	0,01	15,48	0,01	2,95	0,11	99,46	73,88
A6	49,20	0,02	31,31	0,01	0,14	0,01	0,02	15,45	0,01	2,94	0,13	99,24	73,82
A6	49,54	n.d	31,22	n.d	0,12	0,01	n.d	15,26	n.d	3,05	0,14	99,35	72,85
A7	48,38	0,00	31,58	n.d	0,14	n.d	0,02	15,92	0,01	2,63	0,11	98,78	76,55
A7	49,03	0,01	31,13	n.d	0,13	n.d	0,02	15,37	0,01	2,94	0,14	98,79	73,67
A7	48,71	0,02	31,51	0,01	0,12	n.d	0,02	15,84	0,01	2,85	0,11	99,20	73,67
A7	48,68	0,01	31,57	0,01	0,15	0,00	0,03	15,82	0,02	2,76	0,12	99,16	75,51
A7	49,08	0,00	31,24	0,02	0,13	0,01	0,03	15,55	n.d	2,96	0,10	99,12	73,98
A7	49,39	0,02	31,08	n.d	0,15	n.d	0,03	15,25	0,00	3,12	0,11	99,16	72,51
A7	48,88	0,02	31,11	n.d	0,15	0,01	0,03	15,48	0,02	2,95	0,16	98,81	73,72
A7	48,97	0,02	31,19	0,01	0,16	n.d	0,02	15,48	0,00	2,92	0,16	98,93	73,88
A7	48,73	0,01	31,43	n.d	0,15	n.d	0,01	15,56	n.d	2,84	0,14	98,87	74,55
A7	49,00	0,01	31,17	0,01	0,16	0,01	0,02	15,21	0,01	3,03	0,18	98,83	72,72
A7	49,09	0,02	31,23	n.d	0,16	n.d	0,03	15,48	0,00	2,91	0,18	99,10	73,86
A7	49,26	0,03	30,95	n.d	0,19	0,01	0,01	15,12	n.d	3,04	0,19	98,80	72,54
A7	49,20	0,01	30,93	n.d	0,17	0,00	0,02	15,17	n.d	3,05	0,20	98,76	72,51
A7	49,01	0,04	31,26	0,02	0,17	0,01	0,04	15,40	n.d	2,95	0,19	99,08	73,45
A7	49,14	0,02	31,28	n.d	0,14	n.d	0,02	15,57	0,02	3,02	0,18	99,37	73,30
A8	49,58	0,01	31,23	0,02	0,15	0,01	0,03	15,23	n.d	3,09	0,16	99,51	72,50
A8	49,36	0,03	31,22	0,02	0,12	0,00	0,02	15,25	n.d	2,98	0,14	99,13	73,30
A8	48,70	0,02	31,54	n.d	0,14	n.d	0,02	15,90	0,00	2,70	0,13	99,16	75,88
A8	49,39	0,01	31,31	n.d	0,15	0,00	0,02	15,38	0,01	2,90	0,12	99,29	74,07
A8	49,36	0,01	31,32	n.d	0,16	n.d	0,03	15,29	n.d	2,94	0,12	99,23	73,69
A8	49,24	n.d	31,20	n.d	0,14	n.d	0,02	15,36	0,02	2,93	0,15	99,04	73,72
A8	48,76	0,02	31,78	n.d	0,14	0,01	0,03	16,01	n.d	2,62	0,11	99,47	76,65
A8	49,11	0,02	31,47	0,02	0,15	0,00	0,01	15,49	n.d	2,77	0,15	99,18	74,86
A8	47,96	0,00	32,30	n.d	0,13	n.d	0,01	16,47	0,00	2,37	0,08	99,34	78,98
A8	48,97	n.d	31,59	n.d	0,18	0,00	0,01	15,54	n.d	2,89	0,13	99,30	74,30
A8	49,47	0,01	31,18	0,01	0,16	0,01	0,01	15,21	0,00	3,00	0,15	99,20	73,07
A8	49,43	0,01	31,09	n.d	0,15	0,00	0,01	15,16	n.d	3,11	0,14	99,10	72,39
A9	49,08	n.d	31,67	n.d	0,20	0,00	0,02	15,82	n.d	2,71	0,13	99,62	75,75
A9	49,38	0,04	31,31	n.d	0,20	n.d	0,02	15,49	0,01	2,88	0,16	99,47	74,16
A9	48,75	0,03	31,09	n.d	0,19	0,00	0,02	15,51	0,00	2,72	0,16	98,47	75,23
A9	49,48	0,02	31,24	n.d	0,16	0,01	0,01	15,28	n.d	2,94	0,17	99,32	73,41
A9	49,67	0,02	31,13	n.d	0,14	n.d	0,01	15,17	n.d	2,94	0,17	99,25	73,31
A9	48,98	0,02	31,19	n.d	0,14	n.d	0,01	15,36	n.d	2,79	0,14	98,63	74,65
A9	49,20	0,01	31,19	0,01	0,12	0,00	0,03	15,30	n.d	2,95	0,09	98,90	73,77
A9	49,48	0,02	31,24	n.d	0,13	0,01	0,02	15,27	0,02	3,00	0,08	99,26	73,43
A9	49,00	n.d	31,74	0,07	0,15	0,01	0,03	15,79	n.d	2,65	0,10	99,55	72,75

Table B-1: Continued

						B							
Sample number	**SiO_2**	**TiO_2**	**Al_2O_3**	**Cr_2O_3**	**$FeO_{(tot)}$**	**MnO**	**MgO**	**CaO**	**NiO**	**Na_2O**	**K_2O**	**Total**	**An%**
B1	50,05	0,02	31,09	n.d	0,17	0,00	0,02	14,97	0,00	3,10	0,16	99,58	72,09
B1	50,07	0,02	31,02	n.d	0,18	0,02	0,03	14,92	0,01	3,08	0,15	99,49	72,17
B1	49,76	0,03	31,20	n.d	0,15	0,01	0,02	15,17	0,00	2,92	0,15	99,40	73,51
B1	48,35	n.d	32,19	n.d	0,21	n.d	0,03	16,22	0,00	2,41	0,12	99,53	78,28
B1	49,83	0,03	31,02	n.d	0,23	n.d	0,03	14,80	0,01	3,07	0,20	99,22	71,86
B1	49,72	0,02	31,14	n.d	0,19	0,02	0,02	14,95	0,01	2,96	0,17	99,19	72,89
B1	48,81	0,01	31,75	n.d	0,21	n.d	0,02	15,55	0,01	2,61	0,16	99,12	75,98
B1	49,32	0,01	31,35	0,01	0,18	0,01	0,02	15,12	n.d	2,75	0,17	98,93	74,49
B1	49,36	0,02	31,45	0,02	0,20	0,01	0,02	15,47	n.d	2,76	0,15	99,46	74,90
B2	49,25	0,04	31,03	0,01	0,15	0,00	0,02	15,52	n.d	2,93	0,16	99,11	73,86
B2	48,88	0,03	31,25	0,02	0,17	0,00	0,02	15,68	n.d	2,77	0,15	98,97	75,15
B2	49,01	0,03	31,27	0,01	0,17	0,01	0,01	15,55	n.d	2,83	0,16	99,04	74,53
B2	49,19	0,01	31,19	n.d	0,16	0,00	0,02	15,52	0,01	2,87	0,18	99,13	74,21
B2	49,10	0,01	31,26	n.d	0,15	n.d	0,01	15,50	0,02	2,79	0,14	98,99	74,81
B2	49,09	0,02	31,18	n.d	0,16	0,01	n.d	15,47	0,01	2,87	0,17	98,97	74,16
B2	49,22	0,04	31,18	n.d	0,20	0,00	0,03	15,36	n.d	2,89	0,19	99,12	73,81
B2	49,26	0,02	30,98	n.d	0,19	0,01	0,04	15,20	0,01	2,91	0,17	98,78	73,55
B2	48,94	0,02	31,16	n.d	0,20	n.d	0,01	15,56	0,00	2,82	0,15	98,85	74,68
B4	49,30	0,03	31,02	n.d	0,21	0,01	0,02	15,40	n.d	2,94	0,17	99,09	73,63
B4	48,65	0,03	31,10	0,01	0,20	0,00	0,05	15,45	n.d	2,70	0,17	98,35	75,26
B4	49,05	0,02	31,06	n.d	0,21	n.d	0,03	15,60	n.d	2,78	0,16	98,91	74,88
B4	49,45	0,02	31,26	0,01	0,20	n.d	0,00	15,37	n.d	2,92	0,16	99,40	73,73
B4	49,56	0,04	30,93	n.d	0,22	n.d	0,01	15,18	0,01	2,95	0,18	99,08	73,25
B4	48,87	0,04	31,16	0,01	0,20	0,01	0,01	15,57	n.d	2,81	0,16	98,83	74,68
B5	49,72	0,03	30,52	n.d	0,19	n.d	0,01	15,15	0,01	3,10	0,18	98,91	72,26
B5	49,40	0,01	30,99	0,01	0,21	n.d	0,02	15,34	0,01	2,88	0,18	99,04	73,86
B5	49,50	0,03	30,75	n.d	0,17	n.d	0,03	15,23	0,01	2,99	0,20	98,90	73,00
B5	49,47	0,01	30,76	n.d	0,20	0,01	0,00	15,26	0,01	2,95	0,16	98,82	73,39
B5	49,39	0,02	30,88	n.d	0,19	n.d	0,01	15,36	0,01	2,92	0,17	98,94	73,71
B5	48,64	0,03	31,18	n.d	0,23	n.d	0,01	15,76	0,01	2,75	0,15	98,74	75,38
B5	49,71	0,02	30,71	n.d	0,24	0,01	0,02	14,94	n.d	3,13	0,17	98,94	71,84
B5	47,60	0,02	26,94	n.d	0,17	0,00	0,02	17,01	0,00	3,60	0,34	95,71	71,07
B5	49,61	0,02	30,84	n.d	0,22	0,00	0,02	15,26	0,01	2,98	0,19	99,14	73,11
B6	49,46	0,01	30,96	0,01	0,12	0,01	0,03	15,29	0,01	2,94	0,11	98,94	73,71
B6	48,93	0,02	31,34	n.d	0,15	n.d	0,03	15,81	0,00	2,74	0,10	99,11	75,73
B6	49,47	0,03	30,92	0,01	0,14	0,01	0,03	15,29	n.d	2,97	0,15	99,00	73,34
B6	49,05	0,01	31,20	n.d	0,16	0,02	0,03	15,56	0,00	2,80	0,13	98,95	74,87
B6	49,46	0,02	31,02	n.d	0,13	0,01	0,03	15,20	0,01	2,94	0,14	98,94	73,52
B6	49,18	0,02	30,91	n.d	0,13	n.d	0,02	15,52	n.d	2,90	0,14	98,83	74,12
B6	49,56	0,03	30,83	n.d	0,13	n.d	0,03	15,05	0,02	3,01	0,16	98,81	72,75
B7	50,07	0,02	30,69	0,01	0,15	0,00	0,02	14,89	n.d	3,06	0,16	99,07	72,20
B7	49,64	0,03	31,16	n.d	0,15	n.d	0,06	15,12	n.d	2,97	0,20	99,32	72,94
B7	49,20	0,02	31,24	n.d	0,17	0,00	0,03	15,52	n.d	2,87	0,17	99,21	74,23

Table B-1: Continued

A													
Sample number	**SiO_2**	**TiO_2**	**Al_2O_3**	**Cr_2O_3**	**$FeO_{(tot)}$**	**MnO**	**MgO**	**CaO**	**NiO**	**Na_2O**	**K_2O**	**Total**	**An%**
B7	48,99	0,03	31,40	n.d	0,15	0,02	0,01	15,71	0,00	2,69	0,15	99,14	75,71
B7	49,64	0,04	31,11	n.d	0,17	0,00	0,02	15,33	n.d	2,94	0,16	99,41	73,57
B7	49,30	0,02	31,18	0,02	0,20	n.d	0,03	15,39	n.d	2,90	0,16	99,20	73,91
B7	49,48	0,02	31,23	n.d	0,15	0,00	0,01	15,30	0,00	2,93	0,18	99,30	73,49
B8	48,75	0,02	31,37	0,01	0,19	0,01	0,02	15,71	0,00	2,82	0,16	99,05	74,83
B8	49,24	0,02	31,21	n.d	0,17	0,01	0,02	15,17	0,00	3,06	0,19	99,08	72,48
B8	49,16	0,00	30,88	n.d	0,19	0,00	0,01	15,09	n.d	3,05	0,16	98,54	72,59
B8	48,82	0,02	31,25	n.d	0,18	0,00	0,03	15,49	0,01	2,90	0,18	98,89	73,96
B8	48,78	0,03	31,16	n.d	0,20	0,01	0,01	15,46	n.d	2,83	0,16	98,63	74,41
B8	48,70	0,01	31,36	n.d	0,19	n.d	0,00	15,71	n.d	2,75	0,14	98,87	75,33
B8	48,78	0,02	31,56	n.d	0,16	n.d	0,02	15,60	0,00	2,77	0,17	99,10	74,91
B8	48,55	0,04	31,41	n.d	0,18	0,01	0,02	15,66	0,00	2,79	0,17	98,82	74,93
B8	49,21	0,03	31,14	0,01	0,17	0,01	0,03	15,33	n.d	2,92	0,16	99,02	73,70
B9	48,75	n.d	31,56	n.d	0,14	0,01	0,02	15,59	0,00	2,77	0,12	98,96	75,19
B9	48,89	0,01	31,38	n.d	0,15	n.d	0,03	15,47	0,01	2,84	0,15	98,93	74,43
B9	49,29	0,02	31,28	0,01	0,18	n.d	0,03	15,25	n.d	2,95	0,16	99,17	73,37
B9	49,42	0,02	31,77	0,01	0,19	0,00	0,01	15,61	0,00	2,81	0,16	99,99	74,76
B9	48,53	0,02	30,99	n.d	0,18	0,00	0,00	15,35	n.d	2,84	0,16	98,07	74,22
B9	48,26	0,01	31,70	0,02	0,19	n.d	0,01	15,77	0,01	2,57	0,14	98,67	76,57
B9	48,63	0,02	31,26	0,01	0,20	n.d	0,01	15,45	n.d	2,93	0,16	98,65	73,79
B9	49,44	0,00	31,43	n.d	0,19	0,02	0,04	15,48	0,00	2,85	0,17	99,62	74,27
B9	48,44	0,03	31,48	n.d	0,19	0,01	0,04	15,73	0,01	2,68	0,13	98,74	75,85
B10	49,03	0,01	31,25	n.d	0,13	0,01	0,02	15,26	n.d	2,98	0,15	98,85	73,27
B10	48,85	0,02	31,43	n.d	0,16	0,01	0,02	15,43	n.d	2,94	0,15	98,99	73,76
B10	49,16	0,02	31,42	0,01	0,14	0,01	0,01	15,38	n.d	2,87	0,15	99,17	74,12
B10	48,37	0,01	31,77	0,01	0,17	n.d	0,03	15,83	n.d	2,68	0,13	99,01	75,99
B10	48,59	0,04	31,66	n.d	0,19	0,01	0,01	15,73	0,00	2,70	0,14	99,07	75,66
B10	48,78	0,01	31,68	n.d	0,18	n.d	0,02	15,47	n.d	2,84	0,14	99,13	74,46
B10	48,90	0,00	31,32	0,01	0,18	n.d	0,01	15,26	n.d	2,96	0,17	98,81	73,26
B10	48,97	0,04	31,40	n.d	0,17	n.d	0,02	15,44	0,01	2,95	0,18	99,18	73,56
B11	48,93	0,02	31,80	n.d	0,17	n.d	0,02	15,57	0,00	2,74	0,15	99,40	75,19
B11	48,86	0,01	31,72	0,01	0,18	0,02	0,03	15,50	n.d	2,80	0,15	99,27	74,70
B11	48,49	0,02	31,49	n.d	0,17	n.d	0,03	15,36	n.d	2,79	0,16	98,50	74,58
B11	49,05	0,02	31,73	0,01	0,18	0,01	0,02	15,47	0,01	2,90	0,15	99,53	74,07
B11	49,18	0,03	31,81	n.d	0,18	0,00	0,01	15,50	n.d	2,91	0,13	99,77	74,06
B11	47,02	n.d	33,04	0,01	0,16	0,01	0,02	17,01	0,02	2,03	0,08	99,40	81,85
B11	48,76	0,01	31,94	0,00	0,16	n.d	0,02	15,66	n.d	2,67	0,14	99,37	75,78
B11	48,26	0,02	32,01	0,01	0,14	0,01	0,00	16,00	n.d	2,56	0,12	99,14	77,00
B12	48,65	0,02	32,14	0,00	0,13	0,00	0,03	16,06	n.d	2,58	0,12	99,74	76,95
B12	49,09	0,02	31,70	0,00	0,14	0,02	0,03	15,54	n.d	2,85	0,16	99,54	74,42
B12	48,86	0,01	31,72	0,00	0,14	n.d	0,04	15,43	n.d	2,84	0,15	99,18	74,36
B12	49,09	0,01	31,65	0,01	0,16	n.d	0,01	15,41	n.d	2,86	0,16	99,35	74,15
B12	48,73	0,02	31,57	0,00	0,16	0,01	0,01	15,42	n.d	2,80	0,17	98,90	74,54
B12	49,25	0,01	31,67	0,00	0,16	0,00	0,01	15,44	0,00	2,87	0,16	99,57	74,13

Table B-1: Continued

B													
Sample number	**SiO_2**	**TiO_2**	**Al_2O_3**	**Cr_2O_3**	**$FeO_{(tot)}$**	**MnO**	**MgO**	**CaO**	**NiO**	**Na_2O**	**K_2O**	**Total**	**An%**
B12	48,70	0,03	32,09	0,01	0,15	0,01	0,00	15,93	n.d	2,65	0,12	99,68	76,36
B12	49,07	0,03	31,65	0,00	0,14	0,00	0,03	15,38	n.d	2,91	0,17	99,39	73,76
B12	48,18	0,01	32,27	0,01	0,15	n.d	0,02	16,19	0,02	2,52	0,11	99,49	77,51
C													
Sample number	**SiO_2**	**TiO_2**	**Al_2O_3**	**Cr_2O_3**	**$FeO_{(tot)}$**	**MnO**	**MgO**	**CaO**	**NiO**	**Na_2O**	**K_2O**	**Total**	**An%**
C1	49,08	0,00	31,32	0,00	0,11	n.d	0,02	15,06	0,00	3,18	0,05	98,83	72,18
C1	49,98	0,02	31,22	0,00	0,14	n.d	0,02	14,69	0,01	3,33	0,07	99,46	70,63
C1	50,03	0,03	30,98	0,00	0,09	n.d	0,02	14,40	n.d	3,49	0,07	99,11	69,26
C1	48,57	0,01	31,87	0,00	0,16	0,01	0,01	15,78	0,01	2,74	0,12	99,27	75,52
C1	49,14	0,02	31,40	0,00	0,19	0,01	0,02	15,21	n.d	2,95	0,15	99,09	73,36
C1	48,67	0,01	31,56	0,00	0,18	n.d	0,01	15,45	n.d	2,87	0,16	98,93	74,17
C1	48,94	0,04	31,60	0,00	0,15	n.d	0,01	15,29	0,02	2,89	0,14	99,07	73,90
C1	49,39	0,05	31,11	0,00	0,17	n.d	0,03	15,19	0,00	3,05	0,15	99,13	72,76
C1	49,55	0,04	31,35	0,00	0,13	0,00	0,01	15,02	n.d	3,04	0,14	99,28	72,56
C1	49,16	0,02	31,06	0,00	0,15	0,02	0,03	15,00	0,01	3,17	0,16	98,79	71,64
C1	49,37	0,01	30,99	0,01	0,15	n.d	0,03	14,98	n.d	3,11	0,17	98,82	72,00
C1	48,48	0,02	31,71	0,00	0,16	n.d	0,01	15,89	n.d	2,66	0,13	99,06	76,20
C2	48,50	0,01	31,82	0,00	0,17	n.d	0,02	15,99	0,01	2,78	0,07	99,36	75,77
C2	48,02	0,03	32,15	0,01	0,15	n.d	0,02	16,12	0,00	2,62	0,08	99,19	76,93
C2	48,98	0,02	31,36	0,00	0,13	0,00	0,01	15,29	n.d	2,90	0,15	98,84	73,80
C2	49,41	0,03	31,19	0,00	0,17	n.d	0,02	15,02	n.d	3,14	0,18	99,14	71,82
C2	49,63	0,04	31,10	0,00	0,15	0,00	0,03	14,81	n.d	3,22	0,19	99,17	70,98
C2	48,54	0,01	31,88	0,00	0,15	0,00	0,03	15,68	0,03	2,80	0,11	99,22	75,10
C2	49,42	0,04	31,26	0,00	0,17	n.d	0,00	15,07	0,01	3,12	0,16	99,26	72,08
C2	49,86	0,03	30,88	0,01	0,17	n.d	0,03	14,78	n.d	3,35	0,19	99,28	70,18
C3	49,17	0,01	31,53	0,00	0,19	n.d	0,01	15,23	n.d	3,08	0,16	99,38	72,51
C3	49,47	0,03	31,63	0,01	0,19	0,01	0,03	15,18	0,02	3,00	0,16	99,71	72,99
C3	49,48	0,03	31,51	0,00	0,16	0,02	0,02	15,24	n.d	3,02	0,14	99,60	73,00
C3	49,07	0,03	31,77	0,00	0,16	0,01	0,02	15,35	0,00	2,97	0,06	99,43	73,82
C3	49,38	0,03	31,74	0,00	0,12	n.d	0,03	15,38	n.d	3,01	0,07	99,76	73,54
C3	49,18	0,03	31,66	0,00	0,14	0,01	0,02	15,57	0,01	3,00	0,07	99,70	73,87
C4	49,46	0,02	31,66	0,01	0,15	n.d	0,01	15,23	n.d	2,92	0,16	99,62	73,54
C4	49,36	0,03	31,78	0,01	0,16	n.d	0,01	15,37	n.d	2,90	0,17	99,78	73,81
C4	48,75	0,02	31,93	0,00	0,19	n.d	0,03	15,78	n.d	2,66	0,15	99,51	76,02
C4	49,04	0,01	31,66	0,00	0,13	n.d	0,02	15,32	n.d	2,91	0,16	99,26	73,75
C4	49,26	0,04	31,68	0,01	0,16	n.d	0,01	15,32	n.d	2,89	0,16	99,52	73,85
C4	48,84	0,02	31,80	0,00	0,16	0,01	0,02	15,67	0,01	2,79	0,14	99,46	75,03
C5	48,98	0,02	31,92	0,00	0,15	n.d	0,02	15,64	n.d	2,84	0,15	99,73	74,60
C5	48,93	0,03	31,62	0,00	0,13	0,00	0,03	15,43	0,02	2,90	0,16	99,25	73,92
C5	48,53	0,02	32,10	0,00	0,17	0,02	0,02	16,02	n.d	2,60	0,13	99,60	76,74
C5	48,46	0,03	32,04	0,00	0,16	0,01	0,02	15,87	0,00	2,61	0,14	99,34	76,47
C5	49,19	0,03	31,37	n.d	0,15	n.d	0,01	15,30	0,03	3,08	0,19	99,34	72,57
C5	49,42	0,01	31,45	0,01	0,16	0,01	0,03	15,27	n.d	3,09	0,19	99,63	72,44

Table B-1: Continued

C													
Sample number	**SiO_2**	**TiO_2**	**Al_2O_3**	**Cr_2O_3**	**$FeO_{(tot)}$**	**MnO**	**MgO**	**CaO**	**NiO**	**Na_2O**	**K_2O**	**Total**	**An%**
C5	48,83	0,02	32,01	n.d	0,16	0,01	0,01	15,68	0,01	2,76	0,15	99,64	75,22
C5	49,77	0,02	31,57	n.d	0,13	n.d	0,00	15,13	0,02	3,10	0,16	99,88	72,28
C5	48,86	0,03	31,89	n.d	0,16	n.d	0,01	15,63	0,01	2,79	0,14	99,52	74,99
C6	49,03	0,02	31,60	n.d	0,16	n.d	0,01	15,36	n.d	2,90	0,17	99,26	73,78
C6	49,10	0,01	31,49	n.d	0,17	n.d	0,03	15,17	n.d	3,05	0,13	99,15	72,80
C6	49,05	0,01	31,64	0,00	0,16	0,00	0,02	15,41	0,00	2,95	0,16	99,40	73,62
C6	48,74	0,01	31,73	n.d	0,14	0,02	0,02	15,35	0,02	2,85	0,14	99,01	74,22
C6	48,57	0,03	31,72	n.d	0,13	0,01	0,03	15,70	0,00	2,80	0,13	99,13	75,03
C6	48,80	0,01	31,80	0,00	0,11	0,01	0,03	15,50	n.d	2,78	0,14	99,16	74,91
C6	48,52	n.d	31,87	0,01	0,14	0,01	0,02	15,87	n.d	2,74	0,10	99,27	75,75
C6	47,10	0,00	32,60	0,03	0,16	n.d	0,03	16,79	n.d	2,21	0,07	98,99	80,44
C6	47,22	0,02	32,78	0,05	0,18	0,00	0,03	16,71	0,01	2,18	0,05	99,22	80,68
C6	48,52	0,03	31,81	0,01	0,14	n.d	0,03	15,51	n.d	2,82	0,13	99,00	74,68
C6	48,71	0,02	31,73	n.d	0,18	0,01	0,02	15,47	0,01	2,89	0,11	99,14	74,23
C6	49,05	0,02	31,35	0,01	0,17	0,01	0,03	15,12	0,02	3,02	0,17	98,94	72,77
C6	47,99	0,03	32,17	0,00	0,15	n.d	0,02	16,13	0,00	2,53	0,11	99,13	77,40
C6	48,62	0,03	31,55	0,01	0,14	0,00	0,02	15,30	n.d	2,92	0,18	98,76	73,57
C6	48,92	0,02	31,52	n.d	0,13	0,01	0,03	15,30	n.d	2,97	0,18	99,07	73,24
C6	48,64	0,03	31,76	n.d	0,15	n.d	0,01	15,61	n.d	2,86	0,16	99,21	74,47
C6	48,50	0,02	31,85	0,02	0,18	0,02	0,01	15,58	0,00	2,81	0,17	99,17	74,63
C6	48,17	0,03	31,69	0,01	0,17	0,01	0,03	15,68	0,00	2,71	0,16	98,65	75,50
C7	48,36	0,01	32,10	0,01	0,17	n.d	0,02	15,93	n.d	2,65	0,14	99,39	76,28
C7	48,89	0,03	31,73	0,00	0,13	0,00	0,01	15,59	n.d	2,82	0,14	99,34	74,73
C7	48,58	0,01	32,07	n.d	0,15	0,00	0,02	15,75	0,01	2,74	0,14	99,46	75,46
C7	47,72	0,02	32,46	0,01	0,14	0,01	0,01	16,32	n.d	2,39	0,10	99,16	78,63
C7	48,81	0,02	31,73	0,01	0,16	n.d	0,01	15,60	0,01	2,84	0,13	99,31	74,68
C7	49,11	0,02	31,71	0,00	0,16	0,00	0,01	15,32	n.d	2,89	0,14	99,36	73,98
C7	48,97	0,04	31,67	n.d	0,20	n.d	0,02	15,36	n.d	2,90	0,17	99,33	73,82
C7	49,14	0,04	31,48	n.d	0,20	n.d	0,03	15,24	n.d	3,01	0,17	99,29	72,98
C7	48,79	0,00	31,76	n.d	0,18	0,01	0,03	15,64	0,02	2,86	0,17	99,44	74,42
C7	47,91	n.d	31,97	0,00	0,19	0,00	0,02	16,00	n.d	2,57	0,15	98,81	76,81
C7	48,92	0,02	31,54	0,01	0,19	0,01	0,03	15,30	0,00	2,88	0,18	99,08	73,86
C7	48,31	0,01	31,83	0,03	0,19	0,01	0,02	15,95	0,01	2,61	0,16	99,13	76,48
C8	48,66	0,02	31,67	0,00	0,14	n.d	0,02	15,49	0,01	2,83	0,14	98,98	74,52
C8	48,91	0,02	31,60	0,00	0,15	0,01	0,01	15,44	0,00	2,92	0,15	99,21	73,88
C8	49,06	0,02	31,69	0,00	0,15	n.d	0,03	15,31	n.d	2,87	0,14	99,26	74,07
C8	48,88	0,03	31,42	n.d	0,20	0,00	0,03	15,26	0,00	2,94	0,19	98,97	73,32
C8	48,79	0,04	31,78	n.d	0,21	0,00	0,02	15,66	n.d	2,86	0,17	99,52	74,43
C8	48,33	0,01	31,48	n.d	0,19	n.d	0,02	15,55	0,01	2,75	0,17	98,50	75,05
C8	47,85	0,01	32,16	0,00	0,20	0,00	0,01	16,04	n.d	2,53	0,13	98,93	77,26
C8	48,69	0,00	31,69	n.d	0,20	0,00	0,04	15,59	n.d	2,85	0,15	99,21	74,52
C8	48,63	0,03	31,69	n.d	0,21	0,01	0,02	15,47	n.d	2,83	0,17	99,07	74,37

Table B-1: Continued

						D						
Sample number	**SiO_2**	**TiO_2**	**Al_2O_3**	**Cr_2O_3**	**$FeO_{(tot)}$**	**MnO**	**MgO**	**CaO**	**NiO**	**Na_2O**	**K_2O**	**Total**	**An%**
D3	48,82	n.d	31,04	n.d	0,14	n.d	0,02	15,46	0,00	2,96	0,12	98,57	73,73
D3	48,47	0,02	31,29	n.d	0,17	n.d	0,02	15,73	0,01	2,81	0,13	98,64	75,06
D3	48,70	0,01	31,17	n.d	0,15	n.d	0,03	15,45	n.d	2,94	0,15	98,59	73,78
D3	48,99	0,02	30,92	n.d	0,15	0,00	0,03	15,31	n.d	3,06	0,13	98,60	72,90
D3	48,75	0,05	31,15	n.d	0,14	n.d	0,04	15,42	n.d	2,92	0,14	98,61	73,86
D3	48,84	0,00	31,06	n.d	0,15	0,02	0,03	15,35	0,02	3,07	0,14	98,67	72,86
D3	48,07	0,03	31,52	n.d	0,14	0,00	0,02	15,91	n.d	2,67	0,13	98,49	76,15
D3	48,89	0,02	30,92	n.d	0,15	0,01	0,02	15,17	n.d	3,09	0,18	98,44	72,36
D3	48,98	0,04	30,83	n.d	0,14	n.d	0,02	14,93	n.d	3,18	0,16	98,28	71,52
D4	48,76	0,03	31,59	0,00	0,14	n.d	0,03	15,56	n.d	2,82	0,13	99,06	74,75
D4	48,44	0,02	31,89	0,00	0,12	0,01	0,03	15,82	n.d	2,77	0,14	99,24	75,32
D4	48,49	0,00	31,70	0,00	0,13	n.d	0,03	15,59	n.d	2,80	0,13	98,87	74,91
D4	48,72	0,05	31,75	n.d	0,17	0,00	0,02	15,45	n.d	2,76	0,15	99,06	74,91
D4	48,60	0,02	31,61	n.d	0,13	0,00	0,04	15,49	n.d	2,76	0,15	98,79	74,98
D4	48,82	0,02	31,66	n.d	0,15	n.d	0,03	15,26	0,01	2,92	0,16	99,02	73,59
D4	48,85	0,00	31,38	n.d	0,17	0,02	0,02	15,25	n.d	3,00	0,16	98,85	73,09
D4	49,17	0,02	31,45	n.d	0,15	0,00	0,03	15,29	0,01	2,99	0,16	99,29	73,16
D4	48,93	0,01	31,23	0,01	0,14	0,00	0,03	15,14	0,03	3,06	0,18	98,74	72,47
D4	46,73	0,03	33,24	0,06	0,14	0,00	0,02	17,21	0,01	1,88	0,06	99,38	83,18
D4	48,36	0,04	31,93	0,03	0,13	n.d	0,02	15,72	n.d	2,71	0,13	99,06	75,64
D4	48,55	0,02	32,06	0,02	0,13	n.d	0,02	15,91	n.d	2,67	0,11	99,49	76,21
D4	45,73	0,02	33,07	0,11	0,16	n.d	0,01	17,53	0,01	1,82	0,06	98,50	83,92
D4	46,79	0,02	33,17	0,01	0,13	0,00	0,00	17,09	n.d	1,93	0,07	99,20	82,75
D4	46,66	0,01	33,15	0,02	0,11	0,01	0,02	17,27	n.d	1,97	0,06	99,27	82,62
D5	47,99	0,01	31,85	0,02	0,19	0,00	0,02	16,17	n.d	2,53	0,14	98,93	77,30
D5	48,71	0,02	31,23	n.d	0,21	0,01	0,03	15,49	n.d	2,78	0,18	98,66	74,74
D5	48,57	0,04	31,32	n.d	0,19	n.d	0,02	15,64	n.d	2,75	0,16	98,69	75,17
D5	47,83	0,00	30,84	n.d	0,16	0,01	0,02	15,32	n.d	2,82	0,16	97,15	74,35
D5	48,68	0,03	31,37	0,01	0,18	0,00	0,01	15,36	0,01	2,80	0,16	98,60	74,51
D5	48,27	0,04	31,53	0,02	0,17	n.d	0,01	15,75	n.d	2,70	0,14	98,62	75,69
D5	48,12	0,01	31,42	n.d	0,13	n.d	0,02	15,84	0,00	2,73	0,14	98,41	75,66
D5	48,66	0,02	31,37	0,00	0,16	0,01	0,02	15,41	0,02	2,90	0,17	98,72	73,90
D5	48,53	0,03	31,28	n.d	0,15	n.d	0,02	15,68	n.d	2,74	0,16	98,59	75,32

Table B-2: Electron Microprobe data for plagioclase major element oxide for interstitial plagioclase minerals in chromitite layers (intercumulus plagioclase) (wt.%)

A

Sample number	SiO_2	TiO_2	Al_2O_3	Cr_2O_3	$FeO_{(tot)}$	MnO	MgO	CaO	NiO	Na_2O	K_2O	Total	An%
A1	47,13	0,01	33,14	0,04	0,10	0,01	0,02	17,39	n.d	1,89	0,03	99,75	83,46
A1	44,63	0,004	33,93	0,13	0,17	0,01	0,02	18,67	0,004	1,12	0,01	98,70	90,13
A1	45,16	n.d	34,02	0,03	0,14	0,02	0,01	18,67	0,01	1,17	0,01	99,23	89,80
A2	69,06	0,02	19,37	0,02	0,06	n.d	n.d	0,60	0,01	11,52	0,02	100,67	2,77
A2	68,30	0,02	19,55	0,10	0,07	n.d	0,01	0,49	n.d	11,76	0,01	100,32	2,26
A2	65,76	0,01	20,64	0,10	0,12	n.d	0,003	2,20	0,002	10,60	0,03	99,46	10,26
A3	66,17	0,01	20,30	0,12	0,08	n.d	n.d	1,72	0,01	11,00	0,02	99,43	7,93
A5	45,71	n.d	33,25	0,09	0,17	n.d	0,01	18,04	0,003	1,61	0,03	98,92	85,94
A5	49,50	0,02	31,59	0,05	0,08	n.d	0,001	15,47	0,01	3,05	0,03	99,81	73,55
A5	50,17	0,03	30,89	0,16	0,17	n.d	0,03	14,77	n.d	3,46	0,04	99,72	70,09
A5	65,86	0,01	20,49	0,05	0,07	n.d	0,003	1,77	0,01	10,97	0,05	99,28	8,15
A6	48,70	n.d	33,47	0,17	0,16	n.d	0,01	16,74	0,01	2,16	0,01	101,45	80,98
A6	50,76	0,01	30,12	0,11	0,13	0,001	0,02	13,94	0,01	3,93	0,02	99,06	66,12
A7	46,61	n.d	32,44	0,17	0,19	0,004	0,03	17,22	0,003	2,01	0,03	98,71	82,38
A7	45,02	0,01	33,98	0,24	0,19	n.d	0,004	18,56	0,01	1,29	0,01	99,30	88,80
A7	46,40	n.d	32,77	0,07	0,15	n.d	0,04	17,46	0,01	1,80	0,05	98,74	84,04
A7	67,45	0,001	20,22	0,02	0,03	0,01	0,01	0,78	0,01	11,65	0,02	100,19	3,57
A8	47,99	n.d	31,83	0,003	0,17	0,001	0,04	16,21	0,003	2,43	0,07	98,75	78,32
A8	48,43	n.d	31,88	0,10	0,15	n.d	0,03	16,17	0,01	2,59	0,07	99,43	77,24
A8	67,37	n.d	20,03	0,08	0,05	n.d	n.d	0,98	n.d	11,37	0,04	99,92	4,55
A9	46,23	n.d	33,35	0,05	0,08	n.d	0,02	17,80	0,01	1,56	0,02	99,11	86,22
A9	49,44	0,02	31,41	0,12	0,16	n.d	0,02	15,40	0,02	2,92	0,03	99,53	74,29
A9	48,80	0,02	31,74	0,08	0,19	n.d	0,03	15,96	n.d	2,51	0,09	99,41	77,40
A9	67,85	0,001	20,24	0,29	0,21	0,004	0,01	0,80	n.d	11,51	0,02	100,92	3,68

B

Sample number	SiO_2	TiO_2	Al_2O_3	Cr_2O_3	$FeO_{(tot)}$	MnO	MgO	CaO	NiO	Na_2O	K_2O	Total	An%
B1	46,55	0,01	33,38	0,10	0,17	0,003	0,02	17,58	0,01	1,67	0,05	99,54	85,12
B1	40,18	0,01	31,69	0,05		0,09	0,02	23,78	n.d	0,19	0,00	97,38	98,58
B1	47,34	0,003	32,77	0,02	0,15	0,01	0,02	16,84	0,003	1,95	0,05	99,15	82,47
B1	67,89	n.d	20,13	0,03	0,03	n.d	n.d	0,66	0,01	11,64	0,05	100,43	3,03
B2	49,21	0,02	31,77	0,19	0,21	n.d	0,02	15,68	0,01	2,88	0,03	100,02	74,93
B2	65,85	n.d	21,07	0,14	0,11	n.d	n.d	2,33	0,02	10,45	0,03	99,99	10,97
B2	49,21	0,03	31,27	0,20	0,14	0,01	0,001	15,48	n.d	2,95	0,02	99,31	74,26
B2	49,70	0,03	30,99	0,17	0,18	0,01	0,01	15,04	0,002	3,23	0,03	99,38	71,89
B2	67,07	n.d	20,53	0,17	0,12	0,002	0,01	1,76	0,002	10,75	0,03	100,43	8,27
B2	47,56	0,03	32,24	0,15	0,18	0,01	0,02	16,60	0,01	2,28	0,02	99,09	80,01
B3	47,80	0,02	32,33	0,05	0,18	0,01	0,02	16,58	n.d	2,36	0,02	99,36	79,43
B3	65,61	n.d	20,64	0,10	0,18	n.d	0,01	2,03	0,01	10,85	0,02	99,45	9,38
B3	49,72	0,02	31,49	0,13	0,16	0,01	0,03	15,47	0,01	2,93	0,03	100,00	74,39
B3	66,25	0,02	20,69	0,31	0,17	0,01	0,01	1,73	0,01	10,95	0,05	100,19	8,00
B3	50,35	0,004	30,35	0,07	0,11	0,01	0,01	14,33	0,01	3,70	0,03	98,97	68,06
B4	66,09	0,02	20,90	0,09	0,14	n.d	0,001	2,20	n.d	10,72	0,03	100,19	10,18

Table B-2: Continued

B													
Sample number	**SiO_2**	**TiO_2**	**Al_2O_3**	**Cr_2O_3**	**$FeO_{(tot)}$**	**MnO**	**MgO**	**CaO**	**NiO**	**Na_2O**	**K_2O**	**Total**	**An%**
B4	47,94	0,02	32,43	0,05	0,14	0,001	0,02	16,60	n.d	2,29	0,02	99,50	79,94
B4	48,87	0,02	31,28	0,08	0,20	n.d	0,01	15,65	0,004	2,83	0,04	98,97	75,18
B4	52,59	0,01	19,33	0,38		0,05	11,18	1,17	0,03	7,42	0,02	96,55	8,00
B4	65,68	0,004	21,24	0,14	0,18	n.d	0,15	2,51	n.d	10,50	0,03	100,41	11,63
B5	51,18	0,02	29,88	0,10	0,16	0,01	0,01	13,93	0,01	3,93	0,03	99,25	66,14
B5	68,59	n.d	19,59	0,15	0,09	0,001	0,001	0,78	n.d	11,42	0,02	100,65	3,62
B5	50,21	n.d	30,39	0,10	0,13	0,01	0,01	14,44	n.d	3,53	0,02	98,82	69,25
B5	67,85	0,01	19,72	0,07	0,10	0,002	0,001	0,83	n.d	11,74	0,02	100,33	3,73
B5	48,57	0,01	31,37	0,21	0,19	0,01	0,02	15,81	0,01	2,86	0,02	99,08	75,28
B6	48,01	0,004	31,57	0,08	0,10	0,01	0,02	16,13	n.d	2,63	0,01	98,56	77,17
B6	49,68	n.d	31,35	0,05	0,10	n.d	0,02	15,50	0,01	2,98	0,02	99,70	74,15
B7	49,69	0,02	30,90	0,12	0,17	n.d	0,03	15,32	0,001	3,15	0,08	99,46	72,59
B7	66,26	n.d	20,59	0,07	0,05	n.d	0,01	1,81	0,02	10,71	0,05	99,58	8,53
B7	50,24	0,04	30,82	0,09	0,11	0,01	0,01	14,71	n.d	3,49	0,02	99,54	69,87
B7	49,61	0,03	31,36	0,06	0,11	n.d	0,02	15,25	0,01	3,02	0,03	99,49	73,51
B7	65,26	0,01	21,97	0,31	0,21	n.d	0,01	3,59	n.d	9,78	0,05	101,17	16,81
B7	49,66	n.d	30,83	0,12	0,14	0,01	0,01	15,05	n.d	3,23	0,03	99,07	71,93
B9	46,10	0,001	33,93	0,19	0,18	0,02	0,02	18,25	0,001	1,40	0,01	100,09	87,73
B9	64,97	0,01	22,75	0,07	0,05	n.d	0,02	3,49	n.d	9,92	0,05	101,34	16,24
B9	46,96	0,03	32,70	0,19	0,22	0,01	0,02	17,03	0,03	1,97	0,03	99,18	82,55
B10	46,46	0,004	33,14	0,04	0,08	0,004	0,02	17,67	n.d	1,75	0,01	99,17	84,71
B10	63,82	0,01	22,00	0,21	0,14	0,01	0,06	3,31	n.d	10,05	0,06	99,67	15,35
B10	48,19	n.d	32,77	0,04	0,08	0,01	0,01	16,66	n.d	2,37	0,01	100,15	79,50
B10	45,68	0,01	33,51	0,06	0,10	n.d	0,01	17,97	0,01	1,54	0,01	98,91	86,51
B10	47,68	0,01	32,18	0,07	0,11	0,002	0,02	16,35	n.d	2,54	0,03	98,98	77,92
B10	67,14	0,02	20,08	0,02	0,01	n.d	n.d	1,16	0,01	11,55	0,00	100,00	5,26
B11	44,87	n.d	34,55	0,08	0,16	n.d	0,01	18,68	0,01	1,06	0,01	99,43	90,61
B11	45,61	0,03	34,53	0,33	0,29	n.d	0,03	18,28	0,01	1,35	0,03	100,48	88,08
B12	45,91	0,01	34,22	0,18	0,20	n.d	0,03	18,13	n.d	1,45	0,03	100,15	87,19
B12	47,70	n.d	32,63	0,08	0,16	0,02	0,03	16,51	n.d	2,32	0,07	99,51	79,40
B12	46,03	0,02	33,44	0,15	0,18	n.d	0,01	17,56	0,004	1,73	0,04	99,16	84,67
B12	66,30	0,01	21,36	0,18	0,14	0,004	0,01	2,21	n.d	10,79	0,03	101,01	10,14
B12	45,40	0,03	34,39	0,18	0,19	0,01	0,02	18,44	n.d	1,19	0,03	99,88	89,39
C													
Sample number	**SiO_2**	**TiO_2**	**Al_2O_3**	**Cr_2O_3**	**$FeO_{(tot)}$**	**MnO**	**MgO**	**CaO**	**NiO**	**Na_2O**	**K_2O**	**Total**	**An%**
C1	49,24	0,02	31,71	0,10	0,11	0,001	0,01	15,34	0,002	3,03	0,02	99,58	73,54
C1	49,02	0,03	31,61	0,17	0,17	0,01	0,01	15,47	0,02	3,06	0,05	99,61	73,49
C1	46,39	0,01	32,30	0,12	0,15	n.d	0,02	16,90	n.d	2,22	0,03	98,13	80,68
C1	48,21	0,01	31,68	0,13	0,18	0,002	0,02	15,90	0,003	2,68	0,07	98,88	76,34
C2	44,99	0,01	34,14	0,07	0,13	n.d	0,004	18,53	0,002	1,28	0,01	99,16	88,83
C2	66,41	0,002	20,48	0,19	0,12	0,004	n.d	1,34	n.d	11,05	0,04	99,63	6,27
C2	47,66	0,01	32,83	0,06	0,12	0,01	0,03	16,66	0,02	2,37	0,02	99,80	79,43

Table B-2: Continued

C

Sample number	SiO_2	TiO_2	Al_2O_3	Cr_2O_3	$FeO_{(tot)}$	MnO	MgO	CaO	NiO	Na_2O	K_2O	Total	An%
C2	49,78	0,001	31,17	0,03	0,10	n.d	0,03	14,67	0,01	3,38	0,04	99,20	70,43
C3	45,62	0,01	34,15	0,12	0,18	0,02	0,01	18,19	0,004	1,39	0,02	99,71	87,79
C3	46,71	0,01	34,18	0,09	0,17	0,001	0,01	17,86	n.d	1,55	0,02	100,61	86,29
C3	49,60	0,02	31,80	0,14	0,16	n.d	0,02	15,27	0,01	3,11	0,04	100,16	72,95
C3	49,31	n.d	31,80	0,10	0,14	n.d	0,01	15,28	n.d	3,05	0,02	99,71	73,38
C4	46,40	n.d	33,23	0,09	0,11	n.d	0,01	17,19	0,02	1,84	0,03	98,92	83,60
C4	48,56	0,01	31,88	0,10	0,10	0,01	0,02	15,74	n.d	2,89	0,01	99,32	74,99
C4	48,32	n.d	32,13	0,15	0,12	0,01	0,003	15,88	n.d	2,78	0,01	99,41	75,86
C5	47,74	0,02	33,35	0,11	0,16	0,01	0,01	16,94	n.d	2,13	0,02	100,49	81,33
C5	46,27	0,02	33,53	0,07	0,15	n.d	0,02	17,61	n.d	1,75	0,02	99,44	84,67
C5	50,43	n.d	31,23	0,11	0,14	n.d	0,03	14,52	0,003	3,51	0,04	100,01	69,41
C5	44,92	0,02	33,83	0,22	0,20	0,01	0,01	18,41	n.d	1,31	0,02	98,95	88,54
C6	46,67	0,00	33,90	0,12	0,18	n.d	0,02	17,80	n.d	1,70	0,03	100,42	85,14
C6	44,04	n.d	34,58	0,12	0,14	n.d	0,02	19,10	n.d	0,90	0,01	98,91	92,05
C6	45,19	n.d	34,16	0,09	0,18	n.d	0,00	18,41	0,01	1,25	0,02	99,30	88,98
C7	48,03	0,001	31,97	0,03	0,17	0,01	0,09	16,14	0,01	2,58	0,08	99,12	77,18
C7	45,05	0,01	34,24	0,12	0,16	n.d	0,02	18,35	0,01	1,31	0,02	99,28	88,43
C7	45,44	n.d	34,27	0,14	0,19	n.d	0,01	18,21	n.d	1,27	0,03	99,57	88,66
C7	45,32	0,001	34,11	0,15	0,20	n.d	0,02	18,43	0,02	1,33	0,02	99,60	88,34
C8	46,73	0,01	31,68	0,17	0,14	n.d	0,01	15,42	n.d	2,61	0,02	96,79	76,42
C8	46,08	0,01	33,52	0,11	0,13	0,002	0,02	17,63	0,004	1,74	0,01	99,26	84,83
C8	50,84	0,02	30,47	0,18	0,15	0,02	0,01	13,86	0,002	3,84	0,05	99,42	66,44
C8	47,15	0,004	32,52	0,06	0,16	0,01	0,02	16,75	0,02	2,19	0,05	98,92	80,62

D

Sample number	SiO_2	TiO_2	Al_2O_3	Cr_2O_3	$FeO_{(tot)}$	MnO	MgO	CaO	NiO	Na_2O	K_2O	Total	An%
D1	65,99	n.d	19,76	0,20	0,20	0,02	0,13	1,96	0,01	11,25	0,02	99,54	8,77
D1	49,43	n.d	31,41	0,07	0,13	0,004	0,02	15,13	n.d	3,22	0,03	99,43	72,11
D1	49,34	0,03	31,67	0,21	0,20	0,01	0,02	15,17	0,01	3,17	0,02	99,85	72,47
D1	49,56	0,01	31,42	0,07	0,10	0,01	0,00	14,95	0,01	3,27	0,01	99,40	71,60
D2	49,59	0,03	31,83	0,07	0,12	n.d	0,02	15,16	n.d	3,20	0,03	100,03	72,28
D2	49,95	0,001	31,62	0,04	0,10	n.d	0,01	14,92	n.d	3,29	0,02	99,94	71,43
D2	48,94	0,01	31,45	0,10	0,16	0,01	0,01	15,33	0,001	3,20	0,02	99,23	72,49
D2	49,90	0,01	31,41	0,17	0,18	n.d	0,02	14,96	0,01	3,31	0,02	99,99	71,35
D2	49,30	0,02	31,57	0,11	0,10	n.d	0,01	15,17	n.d	3,31	0,02	99,60	71,63
D3	48,40	0,01	31,25	0,15	0,19	n.d	n.d	15,60	0,01	2,86	0,06	98,54	74,81
D3	49,59	0,04	30,67	0,05	0,12	n.d	0,01	14,54	0,01	3,43	0,04	98,50	69,94
D3	48,52	0,03	31,66	0,06	0,15	0,01	0,02	15,63	0,01	2,84	0,02	98,95	75,22
D4	50,48	0,02	30,58	0,09	0,13	0,01	0,01	14,34	0,01	3,69	0,03	99,39	68,11
D4	50,00	0,02	31,52	0,08	0,16	n.d	0,04	14,89	0,01	3,12	0,09	99,93	72,10
D4	47,98	n.d	32,04	0,07	0,17	n.d	0,03	16,12	n.d	2,63	0,06	99,08	76,97
D4	46,38	0,02	32,85	0,12	0,13	0,01	0,001	17,02	n.d	2,14	0,02	98,70	81,33
D4	48,10	0,02	32,21	0,13	0,13	n.d	0,003	15,90	0,02	2,77	0,01	99,30	75,97

Table B-2: Continued

						D							
Sample number	**SiO_2**	**TiO_2**	**Al_2O_3**	**Cr_2O_3**	**$FeO_{(tot)}$**	**MnO**	**MgO**	**CaO**	**NiO**	**Na_2O**	**K_2O**	**Total**	**An%**
D4	47,91	n.d	31,71	0,14	0,15	n.d	0,02	15,75	0,01	2,93	0,03	98,64	74,68
D5	47,71	n.d	32,28	0,11	0,12	n.d	0,02	16,23	0,01	2,52	0,03	99,02	77,97
D5	49,31	0,02	31,01	0,11	0,13	n.d	0,01	15,01	0,01	3,27	0,03	98,91	71,58
D5	48,45	0,02	31,40	0,08	0,12	0,01	0,02	15,56	n.d	2,86	0,03	98,55	74,94
D5	48,04	0,01	31,79	0,15	0,16	0,02	0,002	16,03	n.d	2,59	0,02	98,80	77,32

Appendix C – Chromite mineral chemistry data

Table C-1: Electron Microprobe data for chromite major element oxide for chromite crystals from chromitite layers (massive chromite) (wt.%)

A												
Sample number	**Al_2O_3**	**CaO**	**Cr_2O_3**	**$FeO_{(tot)}$**	**MgO**	**MnO**	**NiO**	**SiO_2**	**TiO_2**	**V_2O_3**	**ZnO**	**Mg#**
A1	15,97	0,02	44,97	29,12	8,14	0,25	0,16	0,02	0,89	0,52	0,11	0,33
A1	15,58	n.d	45,45	28,95	8,21	0,25	0,14	0,01	0,95	0,53	0,12	0,34
A2	16,51	0,01	46,03	26,91	8,82	0,22	0,13	0,01	0,79	0,52	0,11	0,37
A2	16,12	n.d	46,57	26,71	8,76	0,27	0,13	0,01	1,01	0,52	0,11	0,37
A3	15,67	0,01	45,4	27,58	8,62	0,24	0,15	0,02	1,03	0,46	0,11	0,36
A3	16,01	n.d	45,33	27,69	8,69	0,25	0,14	0,01	1,02	0,45	0,1	0,36
A5	15,39	n.d	46,04	28,05	8,46	0,21	0,14	0,02	1,04	0,46	0,12	0,35
A5	15,81	0,01	46,05	27,6	8,79	0,22	0,15	0,01	1,08	0,5	0,09	0,36
A6	16,31	n.d	45,3	27,62	8,9	0,22	0,15	0,01	1,02	0,47	0,09	0,36
A6	16,61	0,01	44,46	27,59	8,93	0,23	0,16	n.d	1,07	0,49	0,11	0,37
A7	15,66	n.d	45,77	27,56	8,61	0,23	0,15	0,02	0,97	0,46	0,11	0,36
A7	15,77	n.d	45,47	27,4	8,86	0,25	0,16	0,01	0,98	0,45	0,12	0,37
A8	15,47	0,01	45,29	28,41	8,47	0,24	0,15	n.d	0,98	0,46	0,12	0,35
A8	15,98	0,01	44,66	28,51	8,67	0,25	0,14	0,01	1,09	0,48	0,1	0,35
A9	15,82	0,04	45,78	27,9	8,61	0,25	0,15	0,01	0,99	0,44	0,12	0,35
A9	15,99	0,02	45,64	27,98	8,75	0,22	0,13	0,01	1,04	0,47	0,12	0,36
B												
Sample number	**Al_2O_3**	**CaO**	**Cr_2O_3**	**$FeO_{(tot)}$**	**MgO**	**MnO**	**NiO**	**SiO_2**	**TiO_2**	**V_2O_3**	**ZnO**	**Mg#**
B1	15,35	0,02	45,45	29,14	8,31	0,27	0,13	n.d	1,11	0,48	0,1	0,34
B1	15,13	0,02	45,61	29,16	8,22	0,21	0,13	0,01	1,18	0,47	0,13	0,33
B2	17,01	n.d	45,85	26,97	8,79	0,25	0,15	n.d	0,79	0,48	0,12	0,37
B2	16,94	0,01	44,97	27,89	8,58	0,26	0,18	0,01	1,04	0,49	0,11	0,35
B3	16,23	n.d	45,66	27,78	8,74	0,24	0,16	n.d	1,03	0,49	0,1	0,36
B3	16,89	0,04	45,55	27,33	8,94	0,26	0,14	0,02	0,86	0,46	0,12	0,37
B3	16,07	n.d	45,3	27,37	8,71	0,22	0,16	0,03	1,01	0,44	0,1	0,36
B4	9,07	0,18	43,7	39,26	3,73	0,33	0,07	0,02	1,32	0,57	0,2	0,14
B4	16,74	n.d	44,92	27,94	8,87	0,24	0,16	n.d	1	0,47	0,1	0,36
B4	17,01	n.d	44,38	28,03	8,84	0,26	0,16	0,01	0,97	0,46	0,09	0,36
B5	16,31	n.d	45,58	28,04	8,46	0,2	0,17	0,02	1,07	0,48	0,1	0,35
B5	15,77	n.d	46,14	28,09	8,36	0,19	0,17	n.d	1,1	0,48	0,11	0,35
B6	16,24	n.d	45,68	27,76	8,78	0,22	0,15	0,02	1,07	0,44	0,12	0,36
B6	16,36	n.d	45,6	27,95	8,76	0,2	0,15	n.d	1,02	0,49	0,11	0,36
B7	15,91	0,01	45,92	27,7	8,74	0,22	0,15	0,01	1,04	0,47	0,09	0,36
B7	16,47	0,01	45,69	27,5	8,78	0,23	0,17	n.d	1,02	0,48	0,1	0,36
B9	15,96	n.d	44,933	28,49	8,728	0,236	0,163	0,021	1,13	0,457	0,113	0,35
B9	16,572	n.d	46,266	27,526	8,429	0,233	0,113	n.d	0,558	0,459	0,11	0,35
B10	16,197	n.d	44,908	27,841	8,693	0,272	0,14	0,016	1,038	0,463	0,114	0,36
B10	15,492	0,015	45,702	28,045	8,587	0,295	0,146	0,003	1,057	0,461	0,104	0,35
B11	14,816	n.d	45,264	29,775	7,768	0,273	0,147	0,003	1,105	0,534	0,116	0,32

Table C-1: Continued

B												
Sample number	**Al_2O_3**	**CaO**	**Cr_2O_3**	**$FeO_{(tot)}$**	**MgO**	**MnO**	**NiO**	**SiO_2**	**TiO_2**	**V_2O_3**	**ZnO**	**Mg#**
B11	14,058	0,007	45,994	30,415	7,35	0,274	0,119	0,017	0,84	0,557	0,106	0,30
B12	15,17	0,007	45,307	28,707	8,446	0,257	0,139	0,011	1,085	0,472	0,093	0,34
B12	15,427	0,008	45,175	28,57	8,587	0,272	0,131	0,019	0,99	0,47	0,089	0,35
C												
Sample number	**Al_2O_3**	**CaO**	**Cr_2O_3**	**$FeO_{(tot)}$**	**MgO**	**MnO**	**NiO**	**SiO_2**	**TiO_2**	**V_2O_3**	**ZnO**	**Mg#**
C1	16,141	0,01	45,512	27,595	8,946	0,264	0,158	0,013	1,002	0,465	0,096	0,37
C1	16,497	n.d	44,578	27,534	9,039	0,239	0,163	0,004	1,09	0,471	0,129	0,37
C2	16,544	n.d	44,224	27,476	8,93	0,253	0,154	0,008	1,053	0,491	0,097	0,37
C2	15,367	n.d	45,196	27,991	8,798	0,275	0,149	n.d	1,121	0,461	0,108	0,36
C3	16,561	0,015	44,247	27,819	9,05	0,219	0,15	n.d	1,096	0,48	0,091	0,37
C3	16,651	0,005	44,706	27,429	8,982	0,287	0,134	n.d	1,07	0,455	0,113	0,37
C4	16,901	n.d	44,106	27,977	8,85	0,272	0,159	0,025	1,021	0,487	0,094	0,36
C4	16,572	0,006	44,858	27,795	8,703	0,248	0,138	0,02	0,96	0,49	0,112	0,36
C5	16,029	0,006	44,876	28,479	8,423	0,242	0,132	0,017	0,98	0,488	0,129	0,35
C5	15,876	0,005	45,039	28,358	8,476	0,273	0,139	0,016	0,928	0,466	0,11	0,35
C6	14,964	0,014	44,468	28,995	8,127	0,315	0,166	0,011	1,071	0,5	0,1	0,33
C6	15,196	0,004	43,741	28,638	8,061	0,287	0,156	0,016	1,135	0,481	0,1	0,33
C6	12,723	0,001	44,784	32,258	6,683	0,336	0,142	0,011	1,198	0,498	0,102	0,27
C6	8,697	0,278	39,204	42,74	2,476	0,337	0,144	0,042	1,445	0,606	0,117	0,09
C6	8,867	0,049	47,15	35,183	4,476	0,35	0,138	0,023	1,254	0,641	0,107	0,18
C7	14,694	0,005	45,032	29,293	8,055	0,295	0,136	0,016	1,114	0,509	0,106	0,33
C7	14,946	n.d	44,757	29,145	8,277	0,31	0,138	0,019	1,086	0,481	0,093	0,34
C8	16,059	0,014	44,485	28,259	8,616	0,257	0,159	n.d	0,936	0,498	0,114	0,35
C8	15,593	n.d	44,994	28,599	8,388	0,295	0,152	0,029	1,08	0,487	0,121	0,34
D												
Sample number	**Al_2O_3**	**CaO**	**Cr_2O_3**	**$FeO_{(tot)}$**	**MgO**	**MnO**	**NiO**	**SiO_2**	**TiO_2**	**V_2O_3**	**ZnO**	**Mg#**
D1	16,26	0,017	45,682	26,939	8,875	0,27	0,135	0,004	0,923	0,484	0,106	0,37
D1	16,015	0,011	45,418	27,451	8,963	0,278	0,133	0,002	1,001	0,465	0,097	0,37
D1	15,902	0,028	45,203	27,618	8,554	0,27	0,136	0,004	0,934	0,505	0,1	0,36
D1	15,966	0,009	44,995	28,112	8,62	0,236	0,139	0,011	1,021	0,491	0,118	0,35
D2	16,612	0,008	44,567	27,384	8,933	0,284	0,141	0,008	0,95	0,444	0,087	0,37
D2	16,874	n.d	45,063	26,982	8,904	0,231	0,12	0,004	0,827	0,464	0,099	0,37
D2	15,828	0,039	45,131	27,206	8,618	0,268	0,131	0,01	0,849	0,449	0,104	0,36
D3	16,168	0,006	45,36	27,543	8,756	0,272	0,158	0,007	0,961	0,442	0,091	0,36
D3	16,597	0,008	44,644	27,734	8,843	0,291	0,133	n.d	0,894	0,433	0,105	0,36
D4	16,406	0,002	43,619	28,073	8,806	0,285	0,151	0,002	1,036	0,472	0,106	0,36
D4	15,753	0,013	44,647	27,992	8,486	0,298	0,138	0,003	0,929	0,466	0,092	0,35
D4	11,739	0,006	46,326	32,387	6,073	0,332	0,177	0,017	1,344	0,502	0,116	0,25
D5	16,501	0,025	44,241	28,188	8,679	0,301	0,152	0,012	1,052	0,464	0,113	0,35
D5	16,65	0,011	44,417	28,201	8,849	0,314	0,153	0,014	0,942	0,438	0,102	0,36

Table C-2: Electron microprobe data for chromite major element oxides for chromite crystals in anorthosite layers (disseminated chromite) (wt.%)

A

Sample number	Al_2O_3	CaO	Cr_2O_3	$FeO_{(tot)}$	MgO	MnO	NiO	SiO_2	TiO_2	V_2O_3	ZnO	Total	Mg#
A1	7,02	0,01	43,82	41,66	3,23	0,38	0,19	0,03	1,83	0,63	0,14	98,94	
A1	7,59	0,02	42,80	41,62	3,03	0,36	0,17	0,03	2,15	0,62	0,14	98,53	0,11
A2	7,76	n.d	46,05	39,70	3,03	0,32	0,16	0,01	1,49	0,64	0,16	99,32	0,12
A2	7,66	0,01	43,04	43,02	1,72	0,71	0,14	0,35	1,52	0,65	0,17	98,98	0,07
A3	9,97	0,01	49,44	32,57	5,57	0,32	0,14	0,02	1,04	0,54	0,12	99,71	0,23
A3	10,00	n.d	45,90	36,93	4,08	0,37	0,13	n.d	1,21	0,56	0,13	99,32	0,16
A4	5,19	0,05	32,45	55,07	0,97	0,38	0,18	0,01	2,05	0,50	0,14	96,98	0,03
A4	5,69	n.d	31,21	54,66	1,46	0,35	0,19	0,01	3,44	0,48	0,15	97,63	0,05
A4	6,71	n.d	34,73	50,48	1,87	0,39	0,17	n.d	3,16	0,45	0,16	98,13	0,06
A5	9,12	0,25	45,73	37,57	3,29	0,37	0,17	0,06	1,01	0,64	0,14	98,35	0,14
A5	11,43	0,02	48,26	31,68	5,87	0,27	0,18	0,01	1,25	0,62	0,10	99,68	0,25
A6	11,23	0,02	47,70	32,78	6,12	0,26	0,15	0,01	1,38	0,51	0,11	100,26	0,25
A6	14,12	0,02	47,86	29,50	6,94	0,27	0,13	0,01	0,81	0,49	0,11	100,25	0,30
A7	11,00	0,04	49,25	31,82	5,31	0,35	0,09	0,02	0,50	0,51	0,14	99,03	0,23
A7	16,15	0,01	46,27	26,85	8,66	0,26	0,11	n.d	0,53	0,44	0,11	99,37	0,37
A7	9,17	n.d	46,96	35,63	4,81	0,35	0,15	0,01	1,62	0,58	0,11	99,38	0,19
A8	11,09	n.d	47,59	32,34	6,12	0,28	0,16	0,01	1,37	0,52	0,09	99,57	0,25
A8	11,97	n.d	46,98	32,77	5,69	0,33	0,13	n.d	0,87	0,54	0,11	99,40	0,24
A9	8,77	0,21	45,33	37,69	4,07	0,31	0,11	0,04	1,55	0,53	0,14	98,72	0,16
A9	7,64	0,05	45,83	40,19	2,91	0,33	0,14	0,03	1,12	0,53	0,13	98,88	0,11

B

Sample number	Al_2O_3	CaO	Cr_2O_3	$FeO_{(tot)}$	MgO	MnO	NiO	SiO_2	TiO_2	V_2O_3	ZnO	Total	Mg#
B1	8,30	n.d	44,88	39,65	3,73	0,31	0,19	n.d	1,79	0,57	0,11	99,54	0,14
B1	7,58	0,01	43,06	42,72	2,71	0,34	0,17	0,01	2,10	0,53	0,13	99,36	0,10
B2	7,88	n.d	48,92	35,99	4,09	0,33	0,16	0,01	1,83	0,58	0,11	99,89	0,17
B2	7,78	n.d	47,10	38,96	2,99	0,32	0,13	0,01	1,25	0,66	0,12	99,32	0,12
B4	9,07	0,18	43,70	39,26	3,73	0,33	0,07	0,02	1,32	0,57	0,20	98,45	0,14
B4	8,11	0,02	43,99	43,80	1,55	0,39	0,10	0,01	0,76	0,52	0,18	99,44	0,06
B5	7,14	0,21	42,16	44,88	1,44	0,37	0,09	0,04	1,23	0,58	0,15	98,29	0,05
B5	7,86	n.d	43,54	42,03	2,87	0,34	0,15	n.d	2,33	0,64	0,16	99,92	0,11
B6	11,24	0,03	49,29	30,86	6,75	0,25	0,13	0,01	1,27	0,52	0,09	100,42	0,28
B6	9,46	0,01	50,47	32,55	5,96	0,26	0,13	n.d	0,84	0,50	0,11	100,29	0,25
B7	10,18	0,06	48,97	32,85	5,54	0,29	0,12	0,03	1,07	0,55	0,12	99,78	0,23
B7	9,70	n.d	46,52	36,19	4,64	0,31	0,13	n.d	1,61	0,54	0,10	99,74	0,19
B8	8,76	0,01	44,83	39,08	3,76	0,32	0,15	0,01	1,55	0,54	0,13	99,13	0,15
B8	8,34	0,003	42,92	40,80	3,47	0,32	0,14	0,01	1,95	0,50	0,10	98,55	0,13
B8	10,11	0,02	44,51	37,89	4,44	0,32	0,13	0,02	1,49	0,49	0,13	99,55	0,17
B9	8,88	0,01	46,01	38,24	3,51	0,32	0,15	0,003	1,61	0,62	0,14	99,50	0,14
B9	9,51	0,01	47,84	35,41	4,47	0,30	0,13	0,01	0,96	0,54	0,13	99,30	0,18
B10	9,27	0,17	45,91	35,78	4,87	0,33	0,11	0,02	1,24	0,56	0,13	98,39	0,20

Table C-2: Continued

B													
Sample number	**Al_2O_3**	**CaO**	**Cr_2O_3**	**$FeO_{(tot)}$**	**MgO**	**MnO**	**NiO**	**SiO_2**	**TiO_2**	**V_2O_3**	**ZnO**	**Total**	**Mg#**
B10	6,86	0,01	41,75	43,50	2,84	0,39	0,20	0,01	2,15	0,57	0,11	98,37	0,10
B11	8,99	n.d	46,13	36,86	4,20	0,36	0,16	0,02	1,74	0,56	0,12	99,13	0,17
B11	7,79	0,003	46,79	37,41	4,07	0,36	0,16	0,01	2,03	0,57	0,12	99,30	0,16
B12	8,42	0,01	47,03	37,20	3,76	0,32	0,16	0,01	1,38	0,57	0,14	98,98	0,15
B12	8,00	0,01	48,13	36,20	4,38	0,34	0,14	0,004	1,17	0,57	0,10	99,05	0,18
C													
Sample number	**Al_2O_3**	**CaO**	**Cr_2O_3**	**$FeO_{(tot)}$**	**MgO**	**MnO**	**NiO**	**SiO_2**	**TiO_2**	**V_2O_3**	**ZnO**	**Total**	**Mg#**
C1	9,70	0,004	47,46	35,70	4,38	0,35	0,11	0,01	1,03	0,60	0,15	99,50	0,18
C1	8,04	0,01	45,99	38,18	3,20	0,57	0,17	n.d	1,84	0,58	0,15	98,74	0,13
C2	8,30	n.d	46,82	39,04	2,76	0,38	0,09	n.d	0,85	0,58	0,17	99,00	0,11
C2	7,42	0,02	45,69	40,08	2,66	0,41	0,13	0,02	1,52	0,76	0,20	98,91	0,11
C3	9,41	n.d	46,50	36,08	4,33	0,35	0,15	0,002	1,31	0,55	0,15	98,83	0,18
C3	9,96	0,02	47,56	32,07	7,16	0,35	0,12	0,01	1,53	0,53	0,11	99,43	0,28
C4	8,50	0,12	44,51	40,41	2,21	0,39	0,14	0,02	1,11	0,67	0,13	98,21	0,09
C4	9,36	0,01	44,17	39,16	3,22	0,38	0,14	0,02	1,49	0,58	0,15	98,67	0,13
C5	12,18	0,05	47,52	32,50	5,01	0,34	0,11	0,01	0,66	0,63	0,11	99,11	0,22
C5	8,17	0,07	46,58	36,77	4,26	0,34	0,12	0,04	1,47	0,59	0,09	98,48	0,17
C6	8,70	0,28	39,20	42,74	2,48	0,34	0,14	0,04	1,45	0,61	0,12	96,09	0,09
C6	8,87	0,05	47,15	35,18	4,48	0,35	0,14	0,02	1,25	0,64	0,11	98,24	0,19
C6	7,38	n.d	44,26	40,55	2,93	0,40	0,13	0,02	1,73	0,65	0,13	98,17	0,11
C7	9,01	0,05	44,91	37,01	4,27	0,39	0,17	0,01	1,50	0,53	0,14	97,98	0,17
C7	7,16	0,02	44,27	40,29	3,18	0,41	0,17	n.d	2,00	0,59	0,15	98,23	0,12
C8	9,25	0,02	47,37	35,36	4,38	0,36	0,15	0,02	1,08	0,66	0,11	98,76	0,18
C8	6,63	0,06	44,49	42,24	1,85	0,43	0,13	0,03	1,46	0,65	0,12	98,09	0,07
D													
Sample number	**Al_2O_3**	**CaO**	**Cr_2O_3**	**$FeO_{(tot)}$**	**MgO**	**MnO**	**NiO**	**SiO_2**	**TiO_2**	**V_2O_3**	**ZnO**	**Total**	**Mg#**
D3	12,38	0,02	48,56	30,32	6,57	0,32	0,12	0,01	0,83	0,48	0,11	99,72	0,28
D3	11,59	0,01	47,80	33,04	4,94	0,35	0,12	0,02	0,71	0,53	0,10	99,21	0,21
D4	9,26	0,01	47,02	34,82	4,77	0,36	0,18	0,01	1,43	0,59	0,12	98,55	0,20
D5	7,20	0,08	43,50	42,95	1,76	0,43	0,15	0,03	1,62	0,63	0,13	98,47	0,07
D5	7,67	0,11	45,60	39,95	2,45	0,39	0,15	0,04	1,32	0,64	0,11	98,42	0,10

Appendix D – In-situ strontium isotope data

Table D-1: In-situ Sr-isotope ratios for cumulus plagioclase minerals

			A			
Sample number	**Corrected $^{87}Sr/^{86}Sr$**	**SE**	**corrected $^{87}Rb/^{86}Sr$**	**SE**	**Initial $^{87}Sr/^{86}Sr$**	**2SE**
A1	0,7067	0,0001	0,0017	$2,81\times10^{-5}$	0,7066	0,0001
A1	0,7064	0,0002	0,0021	$3,06\times10^{-5}$	0,7064	0,0002
A1	0,7066	0,0001	0,0034	$5,70\times10^{-5}$	0,7065	0,0001
A1	0,7065	0,0001	0,0018	$3,36\times10^{-5}$	0,7064	0,0001
A1	0,7064	0,0002	0,0021	$3,58\times10^{-5}$	0,7064	0,0002
A1	0,7065	0,0002	0,0024	$3,65\times10^{-5}$	0,7064	0,0002
A2	0,7062	0,0003	0,0042	$1,33\times10^{-4}$	0,7061	0,0004
A2	0,7064	0,0001	0,0124	$3,43\times10^{-4}$	0,7061	0,0005
A2	0,7070	0,0001	0,0168	$2,26\times10^{-4}$	0,7065	0,0004
A2	0,7062	0,0001	0,0030	$2,96\times10^{-5}$	0,7061	0,0001
A2	0,7063	0,0001	0,0022	$3,75\times10^{-5}$	0,7062	0,0001
A3	0,7060	0,0001	0,0008	$3,26\times10^{-5}$	0,7059	0,0001
A3	0,7064	0,0001	0,0007	$2,45\times10^{-5}$	0,7064	0,0001
A3	0,7076	0,0001	0,0444	$3,13\times10^{-4}$	0,7063	0,0001
A3	0,7061	0,0001	0,0057	$1,07\times10^{-4}$	0,7059	0,0001
A3	0,7060	0,0001	0,0053	$1,28\times10^{-4}$	0,7059	0,0001
A3	0,7064	0,0001	0,0018	$4,19\times10^{-5}$	0,7063	0,0001
A4	0,7069	0,0003	0,0134	$9,43\times10^{-4}$	0,7065	0,0003
A4	0,7062	0,0001	0,0151	$1,21\times10^{-4}$	0,7058	0,0001
A4	0,7067	0,0001	0,0166	$5,27\times10^{-4}$	0,7062	0,0001
A4	0,7065	0,0001	0,0034	$1,01\times10^{-4}$	0,7064	0,0001
A4	0,7062	0,0001	0,0058	$3,11\times10^{-4}$	0,7060	0,0001
A5	0,7064	0,0001	0,0112	$2,33\times10^{-4}$	0,7060	0,0001
A5	0,7065	0,0001	0,0238	$4,49\times10^{-4}$	0,7058	0,0001
A5	0,7057	0,0001	0,0051	$1,06\times10^{-4}$	0,7056	0,0001
A5	0,7067	0,0001	0,0009	$2,64\times10^{-5}$	0,7066	0,0001
A6	0,7059	0,0001	0,0012	$3,20\times10^{-5}$	0,7059	0,0001
A6	0,7061	0,0002	0,0037	$5,96\times10^{-5}$	0,7060	0,0002
A6	0,7075	0,0002	0,1785	$4,47\times10^{-3}$	0,7022	0,0003
A6	0,7062	0,0001	0,0004	$4,16\times10^{-5}$	0,7062	0,0001
A6	0,7065	0,0001	0,0025	$6,46\times10^{-5}$	0,7064	0,0001
A6	0,7061	0,0001	0,0022	$6,46\times10^{-5}$	0,7061	0,0001
A6	0,7065	0,0001	0,0035	$6,30\times10^{-5}$	0,7063	0,0001
A7	0,7063	0,0002	0,0013	$3,54\times10^{-5}$	0,7062	0,0002
A7	0,7067	0,0001	0,0011	$3,34\times10^{-5}$	0,7067	0,0001
A7	0,7065	0,0002	0,0027	$9,08\times10^{-5}$	0,7064	0,0002
A7	0,7069	0,0003	0,0015	$1,13\times10^{-4}$	0,7068	0,0003
A8	0,7062	0,0001	0,0010	$3,42\times10^{-5}$	0,7062	0,0001
A8	0,7075	0,0006	0,0036	$3,55\times10^{-4}$	0,7073	0,0006

Table D-1: Continued

A						
Sample number	**Corrected $^{87}Sr/^{86}Sr$**	**SE**	**corrected $^{87}Rb/^{86}Sr$**	**SE**	**Initial $^{87}Sr/^{86}Sr$**	**2SE**
A9	0,7065	0,0002	0,0018	$4{,}26\times10^{-5}$	0,7064	0,0002
A9	0,7065	0,0001	0,0018	$4{,}13\times10^{-5}$	0,7065	0,0001
A9	0,7061	0,0002	0,0018	$7{,}20\times10^{-5}$	0,7061	0,0002
A9	0,7061	0,0002	0,0035	$8{,}43\times10^{-5}$	0,7060	0,0002
A9	0,7067	0,0001	0,0006	$3{,}55\times10^{-5}$	0,7067	0,0001
A9	0,7066	0,0002	0,0004	$3{,}57\times10^{-5}$	0,7066	0,0002
B						
Sample number	**Corrected $^{87}Sr/^{86}Sr$**	**SE**	**corrected $^{87}Rb/^{86}Sr$**	**SE**	**Initial $^{87}Sr/^{86}Sr$**	**2SE**
B1	0,7067	0,0001	0,0013	$4{,}25\times10^{-5}$	0,7066	0,0001
B1	0,7066	0,0001	0,0009	$3{,}08\times10^{-5}$	0,7066	0,0001
B1	0,7067	0,0001	0,0031	$1{,}55\times10^{-4}$	0,7066	0,0001
B1	0,7065	0,0001	0,0019	$5{,}84\times10^{-5}$	0,7064	0,0001
B1	0,7064	0,0001	0,0021	$7{,}06\times10^{-5}$	0,7064	0,0001
B1	0,7063	0,0001	0,0014	$3{,}11\times10^{5}$	0,7063	0,0001
B2	0,7064	0,0001	0,0028	$5{,}69\times10^{-5}$	0,7063	0,0001
B2	0,7067	0,0001	0,0039	$6{,}93\times10^{-5}$	0,7066	0,0001
B2	0,7061	0,0001	0,0039	$4{,}13\times10^{-5}$	0,7060	0,0001
B2	0,7065	0,0002	0,0024	$3{,}93\times10^{-5}$	0,7064	0,0002
B2	0,7063	0,0002	0,0143	$4{,}23\times10^{-4}$	0,7059	0,0002
B4	0,7062	0,0002	0,0039	$8{,}44\times10^{-5}$	0,7061	0,0002
B4	0,7060	0,0002	0,0029	$5{,}80\times10^{-5}$	0,7059	0,0002
B4	0,7062	0,0002	0,0042	$7{,}51\times10^{-5}$	0,7061	0,0002
B4	0,7065	0,0002	0,0009	$5{,}10\times10^{-5}$	0,7065	0,0002
B4	0,7062	0,0002	0,0042	$7{,}69\times10^{-5}$	0,7061	0,0002
B5	0,7068	0,0001	0,0022	$3{,}61\times10^{-5}$	0,7067	0,0001
B5	0,7064	0,0002	0,0011	$3{,}78\times10^{-5}$	0,7063	0,0002
B5	0,7060	0,0001	0,0013	$4{,}07\times10^{-5}$	0,7059	0,0001
B5	0,7063	0,0002	0,0044	$1{,}76\times10^{-4}$	0,7062	0,0002
B5	0,7068	0,0001	0,0281	$3{,}30\times10^{-4}$	0,7059	0,0001
B5	0,7068	0,0001	0,0096	$2{,}50\times10^{-4}$	0,7065	0,0001
B5	0,7067	0,0001	0,0049	$8{,}21\times10^{-5}$	0,7066	0,0001
B6	0,7064	0,0002	0,0017	$4{,}64\times10^{-5}$	0,7063	0,0002
B6	0,7062	0,0002	0,0011	$5{,}19\times10^{-5}$	0,7062	0,0002
B6	0,7065	0,0002	0,0171	$9{,}22\times10^{-4}$	0,7060	0,0002
B6	0,7064	0,0002	0,0005	$4{,}27\times10^{-5}$	0,7064	0,0002
B6	0,7065	0,0002	0,0005	$4{,}10\times10^{-5}$	0,7065	0,0002
B6	0,7063	0,0002	0,0022	$5{,}76\times10^{-5}$	0,7062	0,0002
B6	0,7061	0,0002	0,0012	$4{,}66\times10^{-5}$	0,7060	0,0002
B6	0,7060	0,0001	0,0011	$3{,}80\times10^{-5}$	0,7060	0,0001
B7	0,7069	0,0002	0,0011	$4{,}37\times10^{-5}$	0,7069	0,0002
B7	0,7061	0,0002	0,0050	$9{,}98\times10^{-5}$	0,7060	0,0002

Table D-1 continued

			B			
Sample number	**Corrected $^{87}Sr/^{86}Sr$**	**SE**	**corrected $^{87}Rb/^{86}Sr$**	**SE**	**Initial $^{87}Sr/^{86}Sr$**	**2SE**
B7	0,7062	0,0002	0,0012	$5{,}17\times10^{-5}$	0,7061	0,0002
B7	0,7068	0,0002	0,0006	$4{,}74\times10^{-5}$	0,7068	0,0002
B7	0,7061	0,0002	0,0009	$4{,}37\times10^{-5}$	0,7061	0,0002
B7	0,7061	0,0002	0,0010	$4{,}22\times10^{-5}$	0,7061	0,0002
B7	0,7064	0,0002	0,0027	$9{,}39\times10^{-5}$	0,7063	0,0002
B7	0,7061	0,0002	0,0011	$4{,}10\times10^{-5}$	0,7060	0,0002
B8	0,7062	0,0002	0,0035	$1{,}71\times10^{-4}$	0,7061	0,0002
B8	0,7063	0,0003	0,0044	$3{,}09\times10^{-4}$	0,7062	0,0003
B8	0,7066	0,0003	0,0024	$6{,}70\times10^{-5}$	0,7065	0,0003
B8	0,7064	0,0002	0,0016	$4{,}61\times10^{-5}$	0,7063	0,0002
B8	0,7061	0,0002	0,0012	$4{,}10\times10^{-5}$	0,7061	0,0002
B8	0,7062	0,0001	0,0016	$4{,}25\times10^{-5}$	0,7061	0,0001
B8	0,7064	0,0002	0,0011	$4{,}14\times10^{-5}$	0,7064	0,0002
B8	0,7064	0,0002	0,0009	$3{,}69\times10^{-5}$	0,7063	0,0002
B8	0,7068	0,0002	0,0027	$4{,}93\times10^{-5}$	0,7067	0,0002
B9	0,7069	0,0002	0,0057	$1{,}50\times10^{-4}$	0,7068	0,0002
B9	0,7059	0,0002	0,0020	$6{,}23\times10^{-5}$	0,7058	0,0002
B9	0,7059	0,0002	0,0007	$4{,}04\times10^{-5}$	0,7059	0,0002
B9	0,7064	0,0001	0,0014	$4{,}28\times10^{-5}$	0,7064	0,0001
B9	0,7068	0,0002	0,0006	$3{,}30\times10^{-5}$	0,7068	0,0002
B9	0,7063	0,0002	0,0009	$4{,}11\times10^{-5}$	0,7063	0,0002
B9	0,7071	0,0001	0,0007	$4{,}29\times10^{-5}$	0,7071	0,0001
B9	0,7063	0,0001	0,0073	$1{,}85\times10^{-4}$	0,7061	0,0001
B10	0,7077	0,0025	0,0053	$5{,}75\times10^{-4}$	0,7075	0,0025
B10	0,7055	0,0004	0,0016	$1{,}25\times10^{-4}$	0,7054	0,0004
B10	0,7063	0,0002	0,0013	$4{,}83\times10^{-5}$	0,7062	0,0002
B10	0,7061	0,0002	0,0027	$1{,}12\times10^{-4}$	0,7060	0,0002
B10	0,7059	0,0002	0,0016	$3{,}90\times10^{-5}$	0,7059	0,0002
B10	0,7065	0,0002	0,0014	$4{,}47\times10^{-5}$	0,7065	0,0002
B10	0,7064	0,0002	0,0022	$4{,}73\times10^{-5}$	0,7064	0,0002
B10	0,7061	0,0002	0,0031	$9{,}87\times10^{-5}$	0,7060	0,0002
B10	0,7063	0,0002	0,0013	$4{,}66\times10^{-5}$	0,7063	0,0002
B10	0,7067	0,0002	0,0225	$3{,}76\times10^{-4}$	0,7061	0,0002
B10	0,7059	0,0002	0,0012	$4{,}13\times10^{-5}$	0,7059	0,0002
B11	0,7064	0,0002	0,0020	$4{,}68\times10^{-5}$	0,7064	0,0002
B11	0,7066	0,0002	0,0025	$4{,}51\times10^{-5}$	0,7066	0,0002
B11	0,7060	0,0002	0,0012	$4{,}35\times10^{-5}$	0,7060	0,0002
B11	0,7067	0,0002	0,0021	$4{,}90\times10^{-5}$	0,7066	0,0002
B11	0,7062	0,0002	0,0017	$4{,}61\times10^{-5}$	0,7061	0,0002
B11	0,7063	0,0002	0,0025	$4{,}55\times10^{-5}$	0,7062	0,0002
B11	0,7066	0,0002	0,0007	$4{,}13\times10^{-5}$	0,7066	0,0002
B11	0,7066	0,0002	0,0044	$1{,}14\times10^{-4}$	0,7065	0,0002

Table D-1 continued

B						
Sample number	**Corrected $^{87}Sr/^{86}Sr$**	**SE**	**corrected $^{87}Rb/^{86}Sr$**	**SE**	**Initial $^{87}Sr/^{86}Sr$**	**2SE**
B11	0,7070	0,0002	0,0284	$3,20\times10^{-4}$	0,7062	0,0002
B11	0,7058	0,0002	0,0007	$4,70\times10^{-5}$	0,7058	0,0002
B12	0,7064	0,0002	0,0012	$5,25\times10^{-5}$	0,7064	0,0002
B12	0,7065	0,0002	0,0034	$1,69\times10^{-4}$	0,7064	0,0002
B12	0,7061	0,0002	0,0011	$4,63\times10^{-5}$	0,7060	0,0002
B12	0,7064	0,0002	0,0019	$6,87\times10^{-5}$	0,7063	0,0002
B12	0,7065	0,0002	0,0012	$4,36\times10^{-5}$	0,7065	0,0002
B12	0,7067	0,0002	0,0009	$4,54\times10^{-5}$	0,7067	0,0002
B12	0,7061	0,0002	0,0010	$4,89\times10^{-5}$	0,7061	0,0002
B12	0,7063	0,0002	0,0010	$3,94\times10^{-5}$	0,7062	0,0002
C						
Sample number	**Corrected $^{87}Sr/^{86}Sr$**	**SE**	**corrected $^{87}Rb/^{86}Sr$**	**SE**	**Initial $^{87}Sr/^{86}Sr$**	**2SE**
C1	0,7062	0,0002	0,0010	$5,07\times10^{-5}$	0,7062	0,0002
C1	0,7060	0,0002	0,0004	$4,93\times10^{-5}$	0,7060	0,0002
C1	0,7061	0,0002	0,0027	$6,37\times10^{-5}$	0,7060	0,0002
C1	0,7065	0,0002	0,0011	$5,05\times10^{-5}$	0,7064	0,0002
C1	0,7063	0,0002	0,0012	$4,91\times10^{-5}$	0,7063	0,0000
C1	0,7066	0,0002	0,0062	$8,71\times10^{-5}$	0,7064	0,0002
C1	0,7062	0,0002	0,0009	$5,28\times10^{-5}$	0,7062	0,0002
C1	0,7061	0,0002	0,0008	$5,03\times10^{-5}$	0,7061	0,0002
C1	0,7064	0,0002	0,0005	$4,65\times10^{-5}$	0,7064	0,0002
C1	0,7058	0,0002	0,0005	$4,10\times10^{-5}$	0,7058	0,0002
C1	0,7065	0,0002	0,0011	$5,75\times10^{-5}$	0,7064	0,0002
C1	0,7057	0,0002	0,0079	$1,22\times10^{-4}$	0,7054	0,0002
C1	0,7059	0,0002	0,0008	$5,89\times10^{-5}$	0,7059	0,0002
C1	0,7063	0,0002	0,0023	$6,18\times10^{-5}$	0,7062	0,0002
C2	0,7065	0,0002	0,0005	$5,74\times10^{-5}$	0,7065	0,0002
C2	0,7067	0,0002	0,0098	$1,68\times10^{-4}$	0,7065	0,0002
C2	0,7066	0,0002	0,0015	$6,65\times10^{-5}$	0,7066	0,0002
C2	0,7061	0,0002	0,0013	$5,03\times10^{-5}$	0,7060	0,0002
C2	0,7061	0,0002	0,0019	$6,16\times10^{-5}$	0,7061	0,0002
C2	0,7059	0,0002	0,0017	$4,39\times10^{-5}$	0,7059	0,0002
C2	0,7064	0,0002	0,0016	$4,42\times10^{-5}$	0,7063	0,0002
C3	0,7062	0,0002	0,0011	$5,66\times10^{-5}$	0,7062	0,0002
C3	0,7062	0,0002	0,0008	$4,67\times10^{-5}$	0,7062	0,0002
C3	0,7063	0,0002	0,0005	$3,96\times10^{-5}$	0,7063	0,0002
C3	0,7062	0,0002	0,0007	$4,21\times10^{-5}$	0,7062	0,0002
C3	0,7067	0,0002	0,0007	$4,07\times10^{-5}$	0,7067	0,0002
C3	0,7061	0,0002	0,0007	$3,89\times10^{-5}$	0,7060	0,0002
C3	0,7052	0,0003	0,0476	$9,87\times10^{-5}$	0,7038	0,0003
C3	0,7064	0,0002	0,0125	$9,84\times10^{-5}$	0,7061	0,0002

Table D-1 continued

B						
Sample number	**Corrected $^{87}Sr/^{86}Sr$**	**SE**	**corrected $^{87}Rb/^{86}Sr$**	**SE**	**Initial $^{87}Sr/^{86}Sr$**	**2SE**
C4	0,7061	0,0002	0,0009	$4{,}80\times10^{-5}$	0,7061	0,0002
C5	0,7065	0,0002	0,0015	$4{,}71\times10^{-5}$	0,7064	0,0002
C5	0,7065	0,0002	0,0041	$7{,}88\times10^{-5}$	0,7063	0,0002
C5	0,7065	0,0002	0,0012	$4{,}29\times10^{-5}$	0,7065	0,0002
C6	0,7063	0,0002	0,0007	$4{,}99\times10^{-5}$	0,7063	0,0002
C6	0,7064	0,0002	0,0010	$5{,}03\times10^{-5}$	0,7064	0,0002
C6	0,7066	0,0002	0,0013	$4{,}62\times10^{-5}$	0,7065	0,0002
C6	0,7062	0,0002	0,0015	$3{,}84\times10^{-5}$	0,7062	0,0002
C6	0,7060	0,0002	0,0013	$3{,}72\times10^{-5}$	0,7060	0,0002
C7	0,7059	0,0006	0,0010	$1{,}66\times10^{-4}$	0,7059	0,0006
C7	0,7062	0,0002	0,0006	$3{,}86\times10^{-5}$	0,7062	0,0002
C7	0,7063	0,0002	0,0006	$3{,}94\times10^{-5}$	0,7063	0,0002
C7	0,7064	0,0001	0,0008	$3{,}35\times10^{-5}$	0,7064	0,0001
C7	0,7061	0,0002	0,0121	$5{,}94\times10^{-4}$	0,7057	0,0002
C7	0,7060	0,0002	0,0020	$4{,}61\times10^{-5}$	0,7060	0,0002
C7	0,7066	0,0002	0,0024	$5{,}31\times10^{-5}$	0,7065	0,0002
C8	0,7061	0,0001	0,0029	$6{,}20\times10^{-5}$	0,7061	0,0001
C8	0,7064	0,0001	0,0052	$1{,}87\times10^{-4}$	0,7063	0,0001
C8	0,7061	0,0002	0,0015	$3{,}80\times10^{-5}$	0,7061	0,0002
C8	0,7071	0,0002	0,0023	$3{,}86\times10^{-5}$	0,7070	0,0002
C8	0,7061	0,0002	0,0113	$1{,}45\times10^{-4}$	0,7058	0,0002
C8	0,7065	0,0002	0,0031	$6{,}52\times10^{-5}$	0,7064	0,0002
D						
Sample number	**Corrected $^{87}Sr/^{86}Sr$**	**SE**	**corrected $^{87}Rb/^{86}Sr$**	**SE**	**Initial $^{87}Sr/^{86}Sr$**	**2SE**
D3	0,7063	0,0002	0,0035	$7{,}27\times10^{-5}$	0,7062	0,0002
D3	0,7061	0,0002	0,0016	$4{,}53\times10^{-5}$	0,7060	0,0002
D3	0,7061	0,0001	0,0003	$3{,}16\times10^{-5}$	0,7061	0,0001
D3	0,7065	0,0001	0,0014	$6{,}74\times10^{-5}$	0,7065	0,0001
D3	0,7062	0,0001	0,0010	$3{,}60\times10^{-5}$	0,7062	0,0001
D3	0,7064	0,0001	0,0008	$3{,}16\times10^{-5}$	0,7064	0,0001
D4	0,7065	0,0001	0,0006	$3{,}78\times10^{-5}$	0,7065	0,0001
D4	0,7065	0,0001	0,0007	$3{,}74\times10^{-5}$	0,7065	0,0001
D4	0,7050	0,0005	0,0006	$1{,}04\times10^{-4}$	0,7050	0,0005
D4	0,7067	0,0002	0,0019	$7{,}44\times10^{-5}$	0,7066	0,0002
D4	0,7066	0,0001	0,0011	$3{,}00\times10^{-5}$	0,7066	0,0001
D4	0,7062	0,0001	0,0011	$2{,}95\times10^{-5}$	0,7062	0,0001
D4	0,7066	0,0001	0,0014	$6{,}12\times10^{-5}$	0,7066	0,0001
D4	0,7056	0,0002	0,0581	$5{,}38\times10^{-4}$	0,7039	0,0002
D5	0,7065	0,0002	0,0014	$5{,}89\times10^{-5}$	0,7065	0,0002
D5	0,7062	0,0002	0,0020	$4{,}44\times10^{-5}$	0,7062	0,0002
D5	0,7064	0,0001	0,0015	$3{,}97\times10^{-5}$	0,7064	0,0001

Table D-1 continued

			D			
Sample number	**Corrected $^{87}Sr/^{86}Sr$**	**SE**	**corrected $^{87}Rb/^{86}Sr$**	**SE**	**Initial $^{87}Sr/^{86}Sr$**	**2SE**
D5	0,7061	0,0002	0,0011	$3{,}90\times10^{-5}$	0,7061	0,0002
D5	0,7066	0,0002	0,0009	$3{,}37\times10^{-5}$	0,7066	0,0002
D5	0,7063	0,0001	0,0039	$6{,}66\times10^{-5}$	0,7062	0,0001

Table D-2: In-situ Sr isotope data for intercumulus plagioclase minerals

A						
Sample number	**Corrected $^{87}Sr/^{86}Sr$**	**SE**	**Corrected $^{87}Rb/^{86}Sr'$**	**SE**	**Initial $^{87}Sr/^{86}Sr$**	**2SE**
A1	0,7085	0,0002	0,0162	$5{,}96\times10^{-4}$	0,7080	0,0002
A1	0,7081	0,0001	0,0186	$7{,}32\times10^{-4}$	0,7075	0,0001
A1	0,7068	0,0001	0,0029	$6{,}59\times10^{-5}$	0,7067	0,0001
A1	0,7065	0,0002	0,0151	$4{,}02\times10^{-4}$	0,7061	0,0002
A1	0,7072	0,0002	0,0105	$1{,}09\times10^{-4}$	0,7069	0,0002
A1	0,7070	0,0002	0,0103	$1{,}04\times10^{-4}$	0,7067	0,0002
A1	0,7071	0,0001	0,0153	$3{,}58\times10^{-4}$	0,7067	0,0001
A1	0,7118	0,0045	0,0742	$4{,}98\times10^{-3}$	0,7096	0,0045
A1	0,7089	0,0001	0,0081	$1{,}82\times10^{-4}$	0,7087	0,0001
A2	0,7096	0,0006	0,0278	$5{,}72\times10^{-4}$	0,7088	0,0006
A2	0,7086	0,0005	0,0080	$3{,}21\times10^{-4}$	0,7083	0,0005
A2	0,7094	0,0006	0,0151	$3{,}61\times10^{-4}$	0,7090	0,0006
A2	0,7099	0,0003	0,0060	$1{,}75\times10^{-4}$	0,7097	0,0003
A3	0,7085	0,0002	0,0016	$4{,}62\times10^{-5}$	0,7085	0,0002
A3	0,7080	0,0001	0,0024	$2{,}96\times10^{-5}$	0,7080	0,0001
A3	0,7084	0,0001	0,0031	$5{,}03\times10^{-5}$	0,7083	0,0001
A3	0,7085	0,0001	0,0041	$6{,}05\times10^{-5}$	0,7084	0,0001
A5	0,7070	0,0001	0,0196	$7{,}76\times10^{-4}$	0,7064	0,0001
A5	0,7078	0,0001	0,0444	$3{,}87\times10^{-4}$	0,7065	0,0001
A5	0,7072	0,0002	0,0203	$5{,}51\times10^{-4}$	0,7066	0,0002
A6	0,7055	0,0007	0,0016	$1{,}60\times10^{-4}$	0,7055	0,0007
A6	0,7060	0,0002	0,0006	$4{,}05\times10^{-5}$	0,7060	0,0002
A7	0,7059	0,0003	0,0059	$2{,}89\times10^{-4}$	0,7057	0,0003
A7	0,7068	0,0004	0,0100	$2{,}18\times10^{-4}$	0,7065	0,0004
A7	0,7079	0,0002	0,0187	$6{,}23\times10^{-4}$	0,7073	0,0002
A7	0,7065	0,0002	0,0027	$9{,}08\times10^{-5}$	0,7064	0,0002
A8	0,7065	0,0005	0,0074	$2{,}42\times10^{-4}$	0,7063	0,0005
A8	0,7066	0,0002	0,0152	$2{,}39\times10^{-4}$	0,7061	0,0002
A8	0,7076	0,0003	0,0221	$6{,}49\times10^{-4}$	0,7069	0,0003
A9	0,7071	0,0003	0,0074	$1{,}32\times10^{-4}$	0,7069	0,0003
A9	0,7065	0,0001	0,0201	$1{,}27\times10^{-3}$	0,7059	0,0001
A9	0,7081	0,0006	0,0039	$3{,}21\times10^{-4}$	0,7080	0,0006
A9	0,7069	0,0002	0,0025	$8{,}40\times10^{-5}$	0,7069	0,0002
B						
Sample number	**Corrected $^{87}Sr/^{86}Sr$**	**SE**	**Corrected $^{87}Rb/^{86}Sr'$**	**SE**	**Initial $^{87}Sr/^{86}Sr$**	**2SE**
B1	0,7091	0,0010	0,0272	$2{,}91\times10^{-3}$	0,7082	0,0010
B1	0,7062	0,0001	0,0060	$7{,}98\times10^{-5}$	0,7061	0,0001
B2	0,7081	0,0002	0,0182	$5{,}71\times10^{-4}$	0,7075	0,0002
B2	0,7079	0,0002	0,0268	$3{,}34\times10^{-4}$	0,7071	0,0002
B2	0,7076	0,0002	0,0104	$2{,}38\times10^{-4}$	0,7073	0,0002
B3	0,7077	0,0001	0,0372	$7{,}91\times10^{-4}$	0,7066	0,0001

Table D-2: continued

B						
Sample number	**Corrected $^{87}Sr/^{86}Sr$**	**SE**	**Corrected $^{87}Rb/^{86}Sr'$**	**SE**	**Initial $^{87}Sr/^{86}Sr$**	**2SE**
B3	0,7060	0,0001	0,0058	$6,46\times10^{-5}$	0,7059	0,0001
B3	0,7075	0,0001	0,0112	$3,72\times10^{-4}$	0,7072	0,0001
B3	0,7064	0,0002	0,0005	$4,33\times10^{-5}$	0,7064	0,0002
B4	0,7081	0,0001	0,0207	$2,80\times10^{-4}$	0,7075	0,0001
B4	0,7080	0,0001	0,0069	$8,77\times10^{-5}$	0,7078	0,0001
B4	0,7079	0,0001	0,0180	$2,24\times10^{-4}$	0,7074	0,0001
B4	0,7080	0,0001	0,0134	$1,95\times10^{-4}$	0,7076	0,0001
B5	0,7073	0,0002	0,0195	$4,35\times10^{-4}$	0,7067	0,0002
B5	0,7077	0,0002	0,0190	$3,07\times10^{-4}$	0,7072	0,0002
B5	0,7078	0,0001	0,0590	$8,40\times10^{-4}$	0,7061	0,0001
B6	0,7062	0,0001	0,0014	$5,65\times10^{-5}$	0,7061	0,0001
B6	0,7068	0,0002	0,0153	$2,24\times10^{-4}$	0,7064	0,0002
B7	0,7069	0,0002	0,0153	$2,03\times10^{-4}$	0,7064	0,0002
B7	0,7062	0,0002	0,0164	$7,19\times10^{-4}$	0,7057	0,0002
B7	0,7064	0,0002	0,0127	$4,73\times10^{-4}$	0,7060	0,0002
B7	0,7064	0,0002	0,0040	$6,86\times10^{-5}$	0,7063	0,0002
B7	0,7069	0,0002	0,0266	$4,20\times10^{-4}$	0,7061	0,0002
B7	0,7042	0,0002	0,1217	$2,04\times10^{-4}$	0,7006	0,0002
B7	0,7070	0,0002	0,0014	$9,99\times10^{-5}$	0,7070	0,0002
B9	0,7121	0,0003	0,1681	$3,61\times10^{-3}$	0,7071	0,0003
B9	0,7066	0,0001	0,0048	$8,07\times10^{-5}$	0,7065	0,0001
B10	0,7065	0,0002	0,0070	$9,60\times10^{-5}$	0,7063	0,0085
B10	0,7064	0,0002	0,0069	$7,69\times10^{-5}$	0,7062	0,0090
B10	0,7064	0,0002	0,0024	$1,18\times10^{-4}$	0,7064	0,0069
B10	0,7061	0,0002	0,0058	$8,03\times10^{-5}$	0,7059	0,0084
B10	0,7065	0,0002	0,0013	$6,98\times10^{-5}$	0,7064	0,0092
B10	0,7072	0,0002	0,0065	$2,34\times10^{-4}$	0,7070	0,0167
B10	0,7073	0,0003	0,0070	$9,88\times10^{-5}$	0,7071	0,0129
B10	0,7056	0,0007	0,0015	$1,68\times10^{-4}$	0,7055	0,0292
B11	0,7074	0,0002	0,0203	$2,57\times10^{-4}$	0,7068	0,0002
B11	0,7078	0,0002	0,0115	$1,61\times10^{-4}$	0,7074	0,0002
B11	0,7081	0,0002	0,0491	$6,71\times10^{-4}$	0,7066	0,0002
B11	0,7080	0,0002	0,0028	$6,50\times10^{-5}$	0,7079	0,0002
B12	0,7060	0,0003	0,0121	$2,05\times10^{-4}$	0,7057	0,0003
B12	0,7056	0,0002	0,0139	$1,74\times10^{-4}$	0,7052	0,0002
B12	0,7072	0,0001	0,0207	$1,84\times10^{-4}$	0,7066	0,0001
B12	0,7065	0,0003	0,0367	$3,88\times10^{-4}$	0,7054	0,0003
B12	0,7065	0,0002	0,0020	$5,12\times10^{-5}$	0,7064	0,0002
B12	0,7071	0,0002	0,0172	$2,84\times10^{-4}$	0,7066	0,0002
B12	0,7084	0,0001	0,0071	$9,61\times10^{-5}$	0,7082	0,0001
B12	0,7059	0,0002	0,0072	$4,53\times10^{-4}$	0,7057	0,0002
B12	0,7068	0,0002	0,0002	$5,04\times10^{-5}$	0,7068	0,0002

Table D-2: Continued

B						
Sample number	**Corrected $^{87}Sr/^{86}Sr$**	**SE**	**Corrected $^{87}Rb/^{86}Sr'$**	**SE**	**Initial $^{87}Sr/^{86}Sr$**	**2SE**
C1	0,7063	0,0002	0,0001	$4{,}00\times10^{-5}$	0,7063	0,0002
C1	0,7069	0,0001	0,0264	$6{,}67\times10^{-4}$	0,7061	0,0001
C1	0,7060	0,0003	0,0017	$7{,}84\times10^{-5}$	0,7060	0,0003
C1	0,7062	0,0003	0,0037	$1{,}55\times10^{-4}$	0,7061	0,0003
C1	0,7067	0,0002	0,0027	$6{,}45\times10^{-5}$	0,7066	0,0002
C1	0,7063	0,0003	0,0008	$6{,}67\times10^{-5}$	0,7063	0,0003
C2	0,7065	0,0002	0,0043	$1{,}85\times10^{-4}$	0,7063	0,0002
C2	0,7077	0,0004	0,0778	$7{,}24\times10^{-4}$	0,7054	0,0004
C2	0,7074	0,0002	0,0071	$1{,}93\times10^{-4}$	0,7072	0,0002
C2	0,7061	0,0003	0,0005	$8{,}30\times10^{-5}$	0,7061	0,0003
C2	0,7069	0,0004	0,0011	$9{,}90\times10^{-5}$	0,7069	0,0004
C3	0,7068	0,0002	0,0054	$2{,}01\times10^{-4}$	0,7066	0,0002
C3	0,7060	0,0002	0,0005	$4{,}19\times10^{-5}$	0,7059	0,0002
C3	0,7065	0,0002	0,0012	$4{,}57\times10^{-5}$	0,7064	0,0002
C3	0,7066	0,0002	0,0019	$5{,}06\times10^{-5}$	0,7065	0,0002
C3	0,7062	0,0002	0,0007	$4{,}66\times10^{-5}$	0,7062	0,0002
C4	0,7067	0,0002	0,0082	$1{,}06\times10^{-4}$	0,7064	0,0112
C4	0,7063	0,0001	0,0062	$7{,}52\times10^{-5}$	0,7061	0,0079
C4	0,7073	0,0002	0,0021	$8{,}84\times10^{-5}$	0,7072	0,0118
C5	0,7062	0,0002	0,0062	$2{,}86\times10^{-4}$	0,7060	0,0116
C5	0,7070	0,0000	0,0024	$5{,}44\times10^{-5}$	0,7069	0,0027
C5	0,7070	0,0000	0,0000	$1{,}06\times10^{-5}$	0,7069	0,0026
C5	0,7064	0,0003	0,0025	$9{,}37\times10^{-5}$	0,7063	0,0003
C6	0,7073	0,0003	0,0134	$2{,}20\times10^{-4}$	0,7069	0,0003
C6	0,7058	0,0002	0,0009	$4{,}70\times10^{-5}$	0,7058	0,0002
C7	0,7066	0,0002	0,0104	$4{,}97\times10^{-4}$	0,7063	0,0002
C7	0,7066	0,0002	0,0065	$1{,}82\times10^{-4}$	0,7064	0,0002
C7	0,7064	0,0001	0,0126	$3{,}46\times10^{-4}$	0,7060	0,0001
C7	0,7064	0,0002	0,0032	$2{,}00\times10^{-4}$	0,7063	0,0002
C8	0,7062	0,0001	0,0057	$9{,}91\times10^{-5}$	0,7060	0,0001
C8	0,7082	0,0001	0,0020	$7{,}29\times10^{-5}$	0,7081	0,0001
C8	0,7064	0,0001	0,0054	$1{,}56\times10^{-4}$	0,7062	0,0001
C8	0,7088	0,0000	0,0012	$1{,}87\times10^{-5}$	0,7088	0,0000
D						
Sample number	**Corrected $^{87}Sr/^{86}Sr$**	**SE**	**Corrected $^{87}Rb/^{86}Sr'$**	**SE**	**Initial $^{87}Sr/^{86}Sr$**	**2SE**
D1	0,7065	0,0001	0,0078	$1{,}35\times10^{-4}$	0,7063	0,0001
D1	0,7065	0,0001	0,0006	$3{,}58\times10^{-5}$	0,7064	0,0001
D1	0,7065	0,0002	0,0013	$4{,}96\times10^{-5}$	0,7065	0,0002
D1	0,7066	0,0001	0,0010	$3{,}58\times10^{-5}$	0,7066	0,0001
D1	0,7066	0,0001	0,0000	$2{,}78\times10^{-5}$	0,7066	0,0001
D1	0,7064	0,0001	0,0001	$2{,}74\times10^{-5}$	0,7064	0,0001

Table D-2: Continued

D						
Sample number	**Corrected $^{87}Sr/^{86}Sr$**	**SE**	**Corrected $^{87}Rb/^{86}Sr'$**	**SE**	**Initial $^{87}Sr/^{86}Sr$**	**2SE**
D1	0,7062	0,0001	0,0001	$2,65\times10^{-5}$	0,7062	0,0001
D2	0,7065	0,0001	0,0014	$5,79\times10^{-5}$	0,7064	0,0001
D2	0,7063	0,0001	0,0016	$4,22\times10^{-5}$	0,7062	0,0001
D2	0,7064	0,0001	0,0001	$2,71\times10^{-5}$	0,7064	0,0001
D2	0,7058	0,0001	0,0001	$2,61\times10^{-5}$	0,7058	0,0001
D2	0,7066	0,0001	0,0016	$3,89\times10^{-5}$	0,7066	0,0001
D2	0,7062	0,0001	0,0003	$2,76\times10^{-5}$	0,7062	0,0001
D3	0,7065	0,0001	0,0021	$4,78\times10^{-5}$	0,7065	0,0001
D3	0,7062	0,0001	0,0001	$2,79\times10^{-5}$	0,7062	0,0001
D3	0,7066	0,0002	0,0001	$2,90\times10^{-5}$	0,7066	0,0002
D4	0,7063	0,0002	0,0051	$7,18\times10^{-5}$	0,7061	0,0002
D4	0,7064	0,0001	0,0014	$4,13\times10^{-5}$	0,7063	0,0001
D4	0,7062	0,0001	0,0022	$4,54\times10^{-5}$	0,7061	0,0001
D4	0,7062	0,0001	0,0146	$1,39\times10^{-4}$	0,7058	0,0001
D4	0,7062	0,0001	0,0013	$3,74\times10^{-5}$	0,7062	0,0001
D4	0,7063	0,0001	0,0008	$4,77\times10^{-5}$	0,7063	0,0001
D4	0,7059	0,0001	0,0014	$5,62\times10^{-5}$	0,7059	0,0001
D4	0,7061	0,0001	0,0026	$6,48\times10^{-5}$	0,7060	0,0001
D5	0,7061	0,0001	0,0005	$3,42\times10^{-5}$	0,7061	0,0001
D5	0,7068	0,0001	0,0007	$3,15\times10^{-5}$	0,7068	0,0001
D5	0,7062	0,0001	0,0011	$3,92\times10^{-5}$	0,7061	0,0001
D5	0,7070	0,0002	0,0012	$5,61\times10^{-5}$	0,7069	0,0002
D5	0,7061	0,0001	0,0038	$9,17\times10^{-5}$	0,7059	0,0001

Table D-3: Standard measurements taken before and during the analysis of the samples.

Comment	Corrected 87Sr/86Sr	SE	corrected 87Rb/86Sr'	SE
InhousePlag-1	0,7071	$3{,}50\times10^{-5}$	0,0002	$8{,}21\times10^{-6}$
BHVO2G-1	0,7036	$7{,}44\times10^{-5}$	0,0667	$5{,}66\times10^{-5}$
BHVO2G-2	0,7035	$7{,}37\times10^{-5}$	0,0665	$6{,}55\times10^{-5}$
InhousePlag-2	0,7072	$4{,}55\times10^{-5}$	0,0001	$9{,}62\times10^{-6}$
BHBO2G-3	0,7033	$8{,}81\times10^{-5}$	0,0665	$6{,}58\times10^{-5}$
InhousePlag-3	0,7071	$3{,}70\times10^{-5}$	0,0001	$7{,}56\times10^{-6}$
BHVO2G-4	0,7034	$7{,}43\times10^{-5}$	0,0686	$6{,}80\times10^{-5}$
Inhouseplag-4	0,7071	$3{,}90\times10^{-5}$	0,0001	$8{,}01\times10^{-6}$
BHV02G^{-5}	0,7035	$8{,}20\times10^{-5}$	0,0684	$5{,}82\times10^{-5}$
BHVO2G-6	0,7036	$7{,}77\times10^{-5}$	0,0679	$7{,}09\times10^{-5}$
InhousePlag^{-5}	0,7072	$3{,}89\times10^{-5}$	0,0002	$8{,}23\times10^{-6}$
BHVO2G-7	0,7034	$8{,}00\times10^{-5}$	0,0679	$6{,}14\times10^{-5}$
BHVO2G-8	0,7034	$7{,}76\times10^{-5}$	0,0676	$8{,}38\times10^{-5}$
BHVO2G-9	0,7040	$9{,}23\times10^{-5}$	0,0672	$7{,}21\times10^{-5}$
InhousePlag-1	0,7071	$4{,}20\times10^{-5}$	0,0001	$7{,}65\times10^{-6}$
BHVO2G-1	0,7036	$8{,}84\times10^{-5}$	0,0668	$6{,}42\times10^{-5}$
BHVO2G-2	0,7034	$8{,}88\times10^{-5}$	0,0678	$5{,}72\times10^{-5}$
BHVO2G-3	0,7035	$9{,}99\times10^{-5}$	0,0679	$6{,}64\times10^{-5}$
InhousePlag-2	0,7073	$4{,}84\times10^{-5}$	0,0002	$9{,}02\times10^{-6}$
InhousePlag-3	0,7072	$4{,}49\times10^{-5}$	0,0001	$9{,}08\times10^{-6}$
BHVO2G-4	0,7034	$8{,}87\times10^{-5}$	0,0696	$7{,}51\times10^{-5}$
InhousePlag-1	0,7071	$4{,}49\times10^{-5}$	0,0001	$9{,}29\times10^{-6}$
InhousePlag-2	0,7070	$4{,}81\times10^{-5}$	0,0002	$9{,}76\times10^{-6}$
BHVO2G-1	0,7034	$8{,}96\times10^{-5}$	0,0667	$6{,}42\times10^{-5}$
BHVO2G-2	0,7035	$1{,}04\times10^{-4}$	0,0671	$7{,}26\times10^{-5}$
BHHVO2G-3	0,7035	$1{,}07\times10^{-4}$	0,0665	$5{,}90\times10^{-5}$
BHVO2G-4	0,7036	$1{,}05\times10^{-4}$	0,0700	$8{,}49\times10^{-5}$
Inhouseplag - 3	0,7071	$4{,}70\times10^{-5}$	0,0002	$1{,}15\times10^{-5}$
InhousePlag-1	0,7070	$4{,}37\times10^{-5}$	0,0002	$1{,}07\times10^{-5}$
BHVO2G-1	0,7033	$9{,}82\times10^{-5}$	0,0677	$4{,}66\times10^{-5}$
BHVO2G-2	0,7038	$1{,}29\times10^{-4}$	0,0660	$5{,}07\times10^{-5}$
InhousePlag-1	0,7072	$5{,}06\times10^{-5}$	0,0002	$1{,}15\times10^{-5}$
BHVO2G-1	0,7035	$1{,}12\times10^{-4}$	0,0678	$4{,}95\times10^{-5}$
InhousePlag-2	0,7071	$5{,}41\times10^{-5}$	0,0002	$1{,}11\times10^{-5}$
BHVO2G-2	0,7035	$1{,}08\times10^{-4}$	0,0673	$7{,}27\times10^{-5}$
BHVO2G-3	0,7033	$1{,}18\times10^{-4}$	0,0681	$5{,}39\times10^{-5}$
BHVO2G-4	0,7037	$1{,}14\times10^{-4}$	0,0677	$4{,}94\times10^{-5}$
InhousePlag-1	0,7072	$6{,}22\times10^{-5}$	0,0002	$1{,}31\times10^{-5}$
BHVO2G-1	0,7038	$1{,}08\times10^{-4}$	0,0673	$6{,}38\times10^{-5}$
BHVO2G-2	0,7034	$1{,}15\times10^{-4}$	0,0672	$4{,}98\times10^{-5}$
BHVO2G-3	0,7031	$1{,}23\times10^{-4}$	0,0685	$6{,}86\times10^{-5}$
BHVO2G - 4	0,7033	$1{,}34\times10^{-4}$	0,0665	$7{,}45\times10^{-5}$
BHVO2G^{-5}	0,7033	$1{,}28\times10^{-4}$	0,0713	$6{,}61\times10^{-5}$
InhousePlag-1	0,7069	$6{,}77\times10^{-5}$	0,0001	$1{,}61\times10^{-5}$

Table D-3: Continued

Comment	Corrected 87Sr/86Sr	SE	corrected 87Rb/86Sr'	SE
BHVO2G-1	0,7033	$1,26\times10^{-4}$	0,0678	$5,76\times10^{-5}$
InhousePlag-2	0,7071	$5,01\times10^{-5}$	0,0001	$1,05\times10^{-5}$
BHVO2G-2	0,7036	$8,99\times10^{-5}$	0,0673	$6,58\times10^{-5}$
InhousePlag-1	0,7073	$4,85\times10^{-5}$	0,0001	$8,87\times10^{-6}$
BHVO2G-1	0,7034	$9,06\times10^{-5}$	0,0672	$7,24\times10^{-5}$
BHVO2G - 2	0,7033	$8,86\times10^{-5}$	0,0663	$7,39\times10^{-5}$
InhousePlag-1	0,7071	$4,87\times10^{-5}$	0,0000	$9,20\times10^{-6}$
BHVO2G-1	0,7033	$8,97\times10^{-5}$	0,0671	$5,77\times10^{-5}$
BHVO2G - 2	0,7033	$9,12\times10^{-5}$	0,0663	$3,36\times10^{-5}$
InhousePlag-1	0,7071	$5,57\times10^{-5}$	0,0001	$1,04\times10^{-5}$
BHVO2G-1	0,7035	$8,88\times10^{-5}$	0,0681	$3,92\times10^{-5}$
BHVO2G-2	0,7032	$1,01\times10^{-4}$	0,0679	$5,47\times10^{-5}$

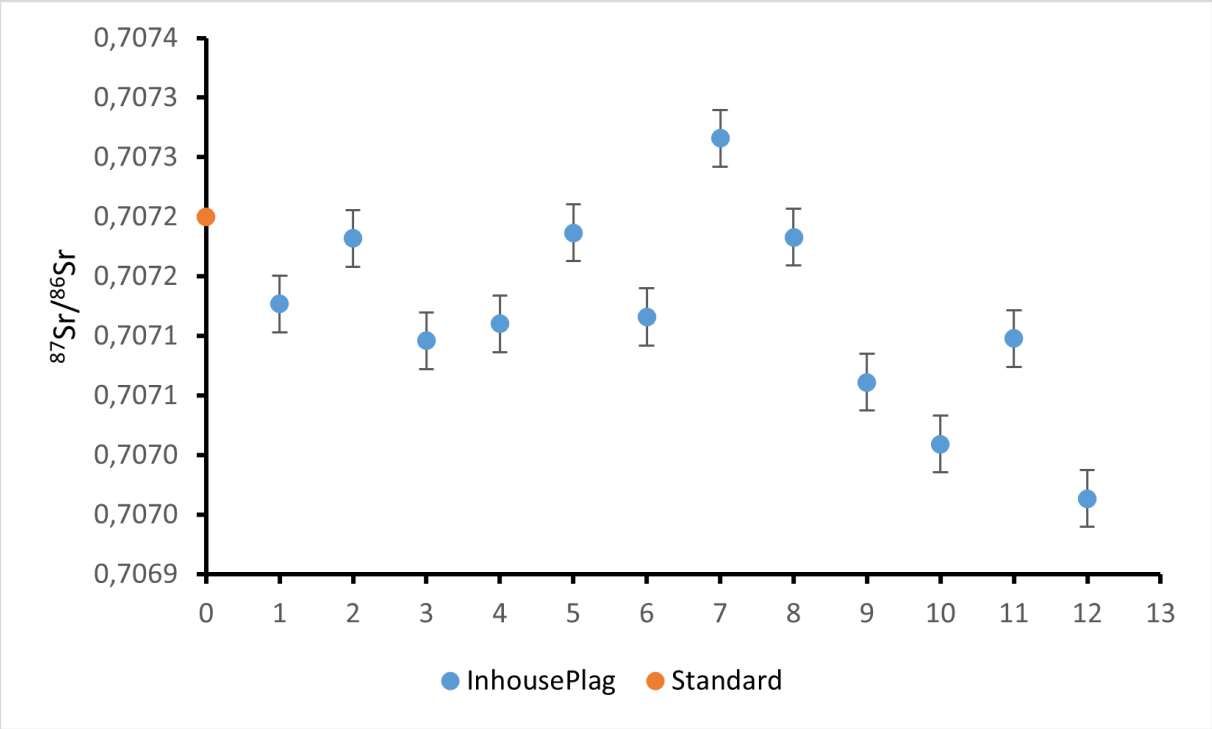

Figure D1: $^{87}Sr/^{86}Sr$ values obtained from the ablation of the inhouse plagioclase standard during sample analysis compared to the average excepted value for this standard.

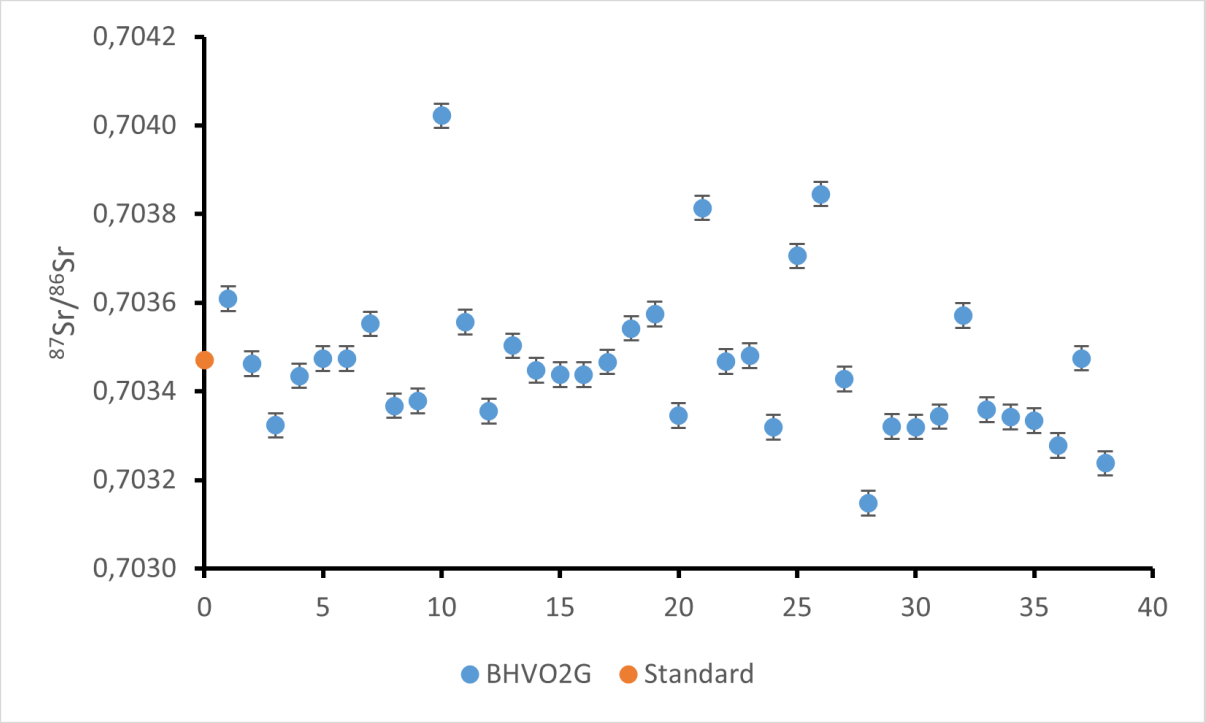

Figure D2: $^{87}Sr/^{86}Sr$ values obtained from the ablation of the BHVO2G standard during sample analysis compared to the average excepted value for this standard.